STABILITY OF DEEP-WATER PIPELINES UNDER COMBINED LOADING

By Spyros A. Karamanos and John L. Tassoulas

OFFSHORE
TECHNOLOGY
RESEARCH
CENTER

A National Science Foundation Engineering Research Center

6/91-B-18-100

For more information contact:

Offshore Technology Research Center
Texas A&M University
1200 Mariner Drive
College Station, TX 77845-3400
(409) 845-6000

or,

Center for Offshore Technology
The University of Texas at Austin
WRW 217
Austin, TX 77812-1085
(512) 471-3753

STABILITY OF DEEP-WATER PIPELINES UNDER COMBINED LOADING

by

Spyros A. Karamanos and John L. Tassoulas

Report on Research
Sponsored by
the
Offshore Technology Research Center

CENTER FOR OFFSHORE TECHNOLOGY
THE UNIVERSITY OF TEXAS AT AUSTIN
1991

Acknowledgments

This study was sponsored by the Offshore Technology Research Center, a National Science Foundation Engineering Research Center. Computing Resources for this work were provided by The University of Texas System Center for High Performance Computing.

STABILITY OF DEEP-WATER PIPELINES UNDER COMBINED LOADING

by

Spyros A. Karamanos and John L. Tassoulas

ABSTRACT

This work investigates the response of relatively thick inelastic tubes under combined external pressure, bending and tension. A nonlinear finite element analysis technique is adopted. Results are presented in the form of pressure-bending, pressure-tension and tension-bending diagrams and are of direct significance in the design of deep-water pipelines.

Table of Contents

Chapter 1

Introduction

1.1 Motivation

During the last decade, the increasing demand for oil and the limited inland oil resources urged oil companies to extend their activities in exploring deep offshore areas. Nowadays, offshore oil and gas production represents approximately twenty percent of the total oil and gas production and is expected to increase within the next few years. Meanwhile, offshore projects are currently into the construction stage in depths of 2500 - 5000 ft.

The feasibility of deep-water exploration and production strongly depends on the available technological capabilities and, therefore, there has been a tremendous need for research in this field. An important area that had to be investigated is the response of pipelines in deep-water. Major deep offshore projects involving pipeline operations in depths of 3000 ft are already in the design stage. In addition, oil companies are already investigating the possibility of pipeline installation in depths of up to 10000 ft. It should be noted that pipeline collapse in such depths is intolerable, not only due to the environmental destruction but also because of the difficulty of repair. Therefore, a complete understanding of pipeline behavior is mandatory.

One of the most critical operations is the installation of pipelines in deep-water. Figure 1.1 shows two typical pipelaying methods: the "$S-lay$"

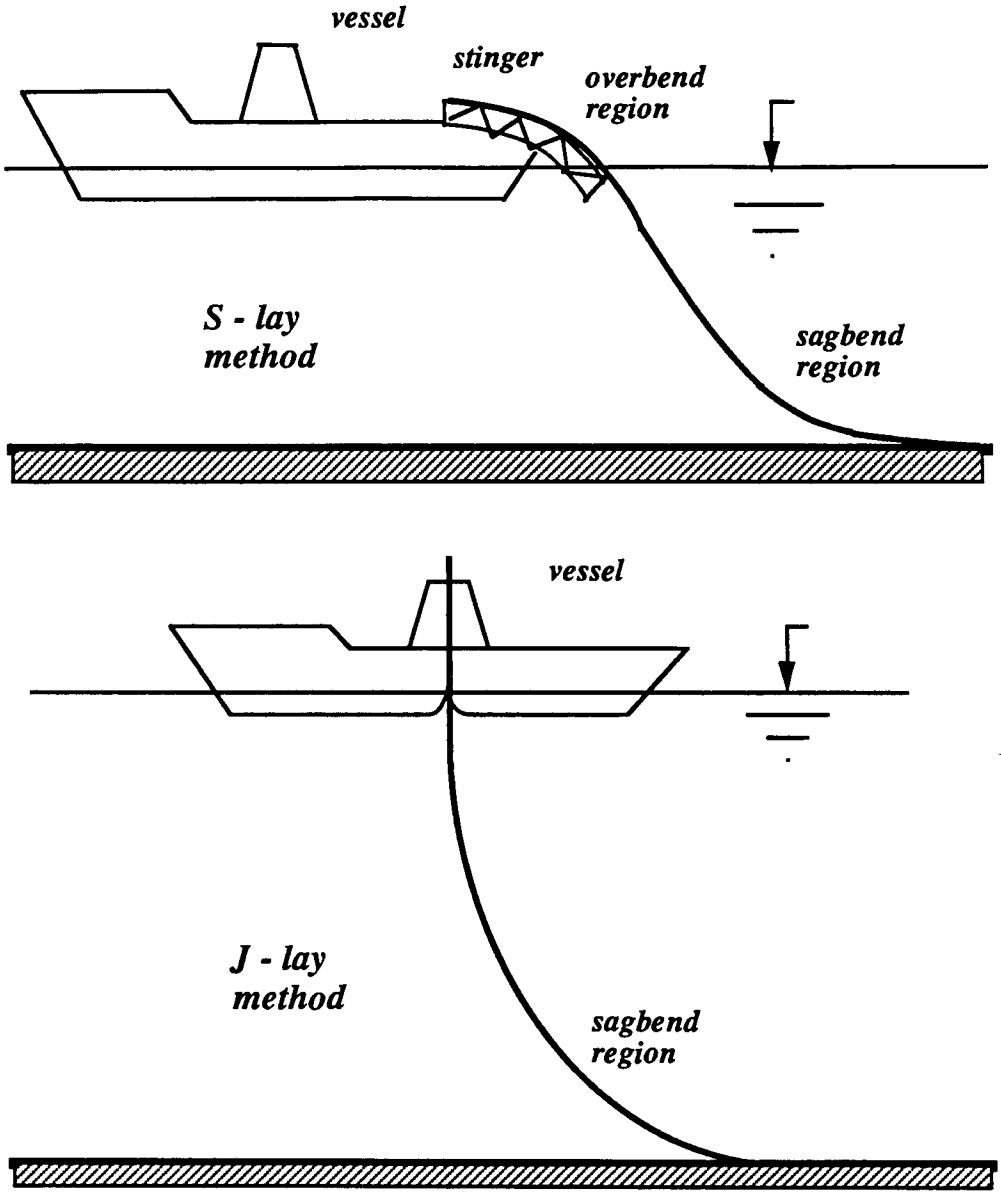

Figure 1.1: Typical pipelaying configurations.

method and the "$J - lay$" method. Of these, the "$S - lay$" method is a conventional procedure that has been very effective for relatively shallow-water applications. However, in depths of more than 3000 ft, the method becomes significantly impractical due to the problems caused by the overbend of the pipe at the stinger. More specifically, an extensive overbend may provoke buckling of the pipe span near the stinger tip. Furthermore, bending strains beyond the yield point will prevent the pipe from laying flat on the seafloor.

On the other hand, the "$J - lay$" method is widely used in deep-water applications because of its simplicity and low cost. Its main advantages over the "$S - lay$" method are the reduced stinger requirements and the resulting singly-curved shape of the pipe.

In both methods, the pipe is subjected to a combination of external pressure, bending and tension. It is important to note that tension is applied in order to control the shape (i.e., the curvature) of the pipeline during installation. This combined loading situation is very likely to cause pipeline buckling.

The stability of tubes under combined loading is a challenging topic in structural mechanics and has been previously treated by several researchers. During the last two decades, a series of experimental and analytical studies have been published leading an improved understanding of the phenomenon.

1.2 Problem Statement - Litterature Review

There are two types of tube instability under combined loading of pressure, tension and bending (Stephens et al [41]):

- bifurcation instability in the form of wrinkling collapse due to the compressive bending stresses
- limit condition due to extensive cross-section ovalization

For thin tubes, having a diameter-to-thickness ratio (D/t) greater than 40, bifurcation controls the collapse. However, for thicker pipes, a limit condition due to extensive ovalization is reached before the bifurcation load (Sherman [38]). In deep-water applications, relatively thick tubes are used. Therefore, attention is focused on the second type of instability.

The first analytical work is due to Brazier [6] who treated the phenomenon of limit moment due to ovalization under pure bending (external pressure equal to zero). Brazier extended St. Venant's solution using an approximate treatment of second-order effects, and derived a moment-curvature relationship assuming elastic behavior and thin pipes.

Ades [2] worked on the ovalization of inelastic tubes subjected to pure bending. He employed the deformation theory of plasticity and assumed an elliptical ovalization shape for the cross section. Reissner [35] investigated the case of elastic pure bending, and presented an analytical formulation using an approximate solution in the form of a series expansion. An improved solution procedure was proposed by Reissner and Weinitschke [36]. Reissner [34] was also the first to analyze elastic tubes under bending and pressure, using the same formulation as in his aforementioned papers.

The need for safe deep-water pipeline installation motivated Shell Development Company and Battelle Columbus Laboratories to perform an analytical and experimental investigation of the phenomenon. Results gave

rise to the well-known "Shell" and "Battelle" formulas, widely used in offshore-pipeline design:

- ("Shell") $\frac{p}{p_c} + \frac{k}{k_c} = 1$
- ("Battelle") $(\frac{p}{p_c})^{2/3} + (\frac{k}{k_c})^{2/3} = 1$

where p is the applied external pressure, k is the bending curvature and p_c, k_c and p_c', k_c' are constants defined in Murphey and Langner [29] and Johns and McConnell [17] for "Shell" and "Battelle" formulas respectively.

Stephens et al. [41] conducted analytical work on the subject using the finite-difference technique. Both types of instability were considered, but results were limited to the case of thin elastic tubes. Important experimental contributions were made by Sherman [38] and Reddy [33] who treated tubes having a variety of D/t values. The important result of these studies is that for pipes with D/t ratio less than 40, limit moment instability, rather than bifurcation instability, controls the behavior. Gellin [12] and Kyriakides and Shaw [20] examined the ovalization instability using similar Galerkin formulations with trigonometric functions for the in-plane section deformation. They further assumed constant curvature along the pipe and that plane sections remain plane throughout the deformation history. Inelastic effects were considered through a J_2-deformation theory of plasticity. In addition, Kyriakides and Shaw presented experimental results for aluminum tubes having a D/t ratio of 34.71. Experimental data were found to be in good agreement with the analytical predictions. Notable analytical contributions to the problem were made by Fabian, who treated elastic buckling of relatively thick pipes [9], and

later, included inelastic effects using small-strain J_2-flow theory with isotropic hardening [10]. In both of these papers, the limit-moment analysis assumed that curvature is constant along the pipe and plane sections remain plane. Moreover, the effect of initial imperfections was examined. The solution of the nonlinear equations is performed through a finite-element technique with trigonometric functions. Using a two-dimensional finite element formulation, Row et al. [37] focused their attention on thick-walled deep-water pipelines. Large displacements, nonlinear shell theory and the Mroz material model with nested yield surfaces were adopted. It was also assumed that deformed sections remain plane and ovalization and curvature are constant along the pipe. Only the instability due to ovalization was considered. Results were limited to the case of bending under constant pressure. A simplified method of treating the problem of ovalization stability under combined loading was presented by de Winter et al. [46]. Curvature and ovalization were assumed to be constant along the pipe. The main contribution of this paper was the observation that the buckling load is sensitive to the loading history.

Extensive experimental as well as analytical results were reported by Corona and Kyriakides [7], [8]. The experiments were small-scale tests on three thick stainless-steel tubes having D/t ratios of 34.7, 24.5 and 18.2. The analytical work used the same basic formulation of Kyriakides and Shaw [20] but examined three different types of material behavior. Analytical results and experimental data were found to be in good agreement. These papers clearly showed that collapse under combined pressure and bending is sensitive to the loading path. Two loading paths were considered:

- $k \rightarrow p$ path, in which bending curvature is imposed up to some level and then is kept constant while pressure is applied.
- $p \rightarrow k$ path, where the pressure is first raised to a certain value and then is kept constant while the curvature is increased.

However, few results were presented for the important case of radial loading in which increments of curvature and pressure are applied in some proportion. The observation regarding path dependence of collapse was verified in the recent work of Fowler [11], who performed large-scale tests on pipes which are candidates for deep-water applications.

1.3 Scope of Present Work

This study is aimed at the development of a rigorous finite-element technique for the analysis of tubular structures. Another objective is the investigation of pipeline behavior under an arbitrary loading sequence, since very limited results exist for paths other than the $k \rightarrow p$, $p \rightarrow k$ paths. Results are obtained for the case of the so-called radial path in which pressure and curvature are increased simultaneously and in some proportion, until buckling occurs. A simple collapse criterion, appropriate for all paths, is proposed and the radial, $k \rightarrow p$, $p \rightarrow k$ paths are examined. In order to simulate the typical experimental procedure, a technique has been developed and is described below for three-dimensional analysis of tubular structures. A simpler version for two-dimensional analysis which assumes constant curvature along the tube is also presented. Its main advantage over the three-dimensional formulation is the low computational cost. Finally, an investigation of the effects of tension

loading on the response of pipelines under external pressure and bending is presented. In all cases, results are reported in the form of interaction diagrams and are of particular significance for safe pipeline design.

Chapter 2

Pipeline Design

In this chapter, a typical pipeline design procedure is outlined. It is important to note that each company has its own method for pipeline design. Therefore, a large number of procedures and empirical formulas exist, derived from the experience of each company. The procedure presented below is used by Shell Development Company [24], [25], [26]. Some alternative design formulas and design procedures are summarized.

2.1 Design Procedure

The first stage is the determination of the pipeline shape during installation. The problem can be stated as follows:

Given:

- pipe diameter (D)
- pipe thickness (t)
- pipe weight per unit length (W)
- material yield stress (σ_y)
- installation height (H)
- boundary conditions at the vessel (which will primarily depend on the installation method)

find the pipelaying configuration.

In this analysis, the pipe is considered to be a nonlinear materially-elastic beam, and the solution of the governing equation is performed by the finite-difference technique. The following computed variables are of particular importance (Figure 2.1):

- horizontal tension (T_o)
- static top tension (T_1)
- minimum sagbend radius (ρ)
- maximum sagbend strain (ϵ_o)
- maximum overbend strain (ϵ_1)

On the other hand, the basic design formulas are the following [24]:

- for pressure and tension:
  - * elastic buckling pressure:

$$p_e = \frac{2E}{1-\nu^2}(\frac{t}{D})^3 \tag{2.1}$$

where E and ν are Young's modulus and Poisson's ratio respectively.

  - * yield pressure:

$$p_y = 2\sigma_y \frac{t}{D} \tag{2.2}$$

  - * yield pressure under tension loads:

$$p_y^{'} = p_y[1-(\frac{T}{T_y})^2] \tag{2.3}$$

where T and T_y are the applied and the yield tension respectively.

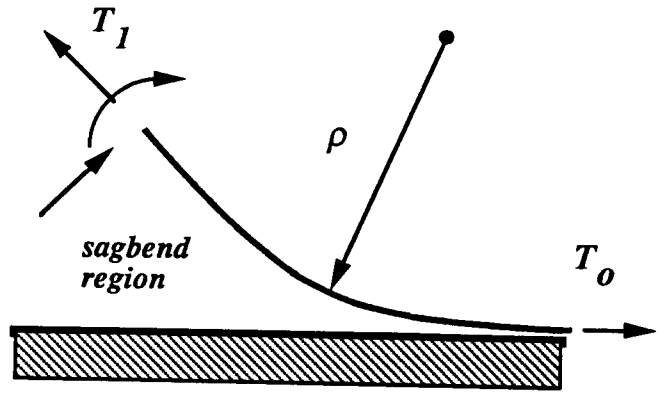

Figure 2.1: Pipe span variables.

* Shell collapse pressure:

$$p_c = \frac{p_e p_y}{\sqrt{{p_e}^2 + {p_y}^2}} \tag{2.4}$$

based on experimental data.

* propagation pressure:

$$p_p = 24\sigma_y(\frac{t}{D})^{2.4} + 48000\sigma_y(\frac{t}{D})^6 \tag{2.5}$$

- for pressure, tension and bending, use the interaction formula:

$$\frac{p}{p_c} + \frac{k}{k_c} = g \tag{2.6}$$

where $k_c = t/D^2$ and g is a function of the inital imperfections and the residual stresses ($g = 1$ for perfect pipe free of residual stresses); more

specifically,

$$g = (1 + a_1\delta + a_2\eta + a_3 r)^{-1} \tag{2.7}$$

where $a_i\,(i = 1, 2, 3)$ are constants and

* $\delta = (D_{max} - D_{min})/(D_{max} + D_{min})$
* $\eta = (t_{max} - t_{min})/(t_{max} + t_{min})$
* $r = wtE/(\pi\sigma_y D^2)$, $w =$ gap width

The design criteria are the following:

- Pressure
  * $p \leq 0.72\,p_c$, if buckling arrestors are used
  * $p \leq 0.72\,p_p$, if buckling arrestors are not used

- Tension
  * (minimum tension) $T_o \geq 200\,WD$
  * (maximum tension) $T_1 \leq 0.72\,T_y$

  where the minimum tension is required in order to control the pipeline shape and the maximum tension in order to avoid yielding.

- Bending
  * $\epsilon_o \leq \epsilon_y$
  * $\epsilon_1 \leq \epsilon_y$

It is notable that, instead of the Shell pipeline formula, a simple yield criterion is used to account for bending capacity. This seems to be very conservative. However, the sagbend region is characterized by high pressure and low curvature that is close to the yield point. For this case, the yield criterion and the Shell formula are in fairly good agreement for design purposes. In addition, this yield criterion justifies the use of a materially-elastic beam theory for the determination of pipeline shape. Another important observation is that a safety factor of $1/0.72 = 1.39$ is adopted which is low. This can be explained by the conservativeness of the analysis. Finally, the use of buckle arrestors has a significant effect on the design. If no buckle arrestors are used, the pipeline must be designed considering the propagation pressure as the ultimate pressure. This is very uneconomical, since the propagation pressure is about seven to ten times lower than the collapse pressure.

2.2 Alternative Design Formulas

- Timoshenko's first-yield pressure equation [44]:

$$p_c'^2 - [p_y + (1 + 1.5e_o\frac{D}{t})p_e]\,p_c' + p_y p_e = 0 \tag{2.8}$$

  where $e_o = (D_{max} - D_{min})/D_{max}$ is a measure of the initial ovality.

- Tension and pressure formula [11]:

$$p_y' = p_y\,\{\sqrt{[1 - 0.75(\frac{T}{T_y})^2]} - 0.5(\frac{T}{T_y})\} \tag{2.9}$$

  and p_y' will replace p_y in Eq. 2.4.

- API Bulletin [4] equation for tension and pressure:

$$p_c = p_{ci}\,\{\sqrt{[1 - 0.75(\frac{T}{T_y})^2]} - 0.5(\frac{T}{T_y})\} \tag{2.10}$$

where p_{ci} is the collapse pressure for zero tension, calculated from one of the following formulas (the choice depending on the grade of steel and the D/t ratio):

* yield collapse

$$p_{ci} = 2\sigma_y \left[\frac{(D/t)-1}{(D/t)^2}\right]$$

* plastic collapse

$$p_{ci} = \sigma_y[A/(D/t) - B] - C$$

* transition collapse

$$p_{ci} = \sigma_y[F/(D/t) - G]$$

* elastic collapse

$$p_{ci} = \frac{46.95 \cdot 10^6}{(D/t)[(D/t) - 1]}$$

where coefficients A, B, C, F, G depend on the D/t ratio and p_{ci} is in psi.

- Battelle [17] bending-pressure formula:

$$\left(\frac{p}{p'_c}\right)^{2/3} + \left(\frac{k}{k'_c}\right)^{2/3} = 1 \tag{2.11}$$

where p'_c is calculated from Timoshenko's formula and $k'_c = 32t^2/D^3$.

- Interaction formulas for combined loading have been derived by de Winter et al. [46] using a simple two-dimensional model:

  * Pressure and tension:

$$0.75\left(\frac{p}{p_y}\right)^2 + \left(\frac{p}{p_y}\right)\left(\frac{1.17p_e}{1.17p_e - p}\right)\left(\frac{D}{t}\right)\beta_o\sqrt{3} + \left(\frac{T}{T_y}\right)^2 - 1 = 0 \tag{2.12}$$

  where $\beta_o = (D_{max} - D_{min})/(D_{max} + D_{min})$

* Pressure and bending:

$$k = \frac{0.5t\sqrt{3}[1 - 0.75(\frac{p}{p_y})^2]^{1.5}}{R^2[1 + (\frac{p}{p_y})(\frac{R}{t})\sqrt{3} - 0.75(\frac{p}{p_y})^2]} \tag{2.13}$$

where $R = D/2$.

- Bending-pressure formula of Jensen [16]:

$$\frac{p}{p_c'} + (\frac{k}{k_o})^a = 1 \tag{2.14}$$

where p_c' follows from Timoshenko's formula, k_o depends on strain hardening and $a = 0.5 + 0.005(D/t)$.

- Formulas for propagation pressure:

  * Palmer [32]:

$$p_p = 3.14(\frac{t}{D})^2 \sigma_y \tag{2.15}$$

  * Mesloh et al. [28]:

$$p_p = 33.9(\frac{t}{D})^{2.5} \sigma_y \tag{2.16}$$

  * Kyriakides and Babcock [22]:

$$p_p = [10.7 + 0.54(\frac{E_T}{\sigma_y})](\frac{t}{D})^{2.25} \sigma_y \tag{2.17}$$

where E_T is the post-yield tangent modulus.

  * Kyriakides and Babcock [22]:

$$p_p = 14.5(\frac{t}{D})^{2.25} \sigma_y \tag{2.18}$$

  * Steel and Spence [40]:

$$p_p = [3.14 + 8.29(\frac{t}{D})^{0.35} (\frac{E_T}{\sigma_y})^{0.12}](\frac{t}{D})^2 \sigma_y \tag{2.19}$$

* de Winter et al. [46]:

$$p_p = 2.94(\frac{t}{D})^2 \sigma_y \tag{2.20}$$

2.3 Alternative Design Procedures

For the sake of completeness, a summary of the available literature on the determination of pipelaying configuration is presented.

A materially-elastic beam theory with nonlinear kinematics was adopted by Wilkins [45] in order to determine pipelaying stresses. The solution was performed using the finite-difference technique. A similar formulation was reported by Palmer et al. [31], whereas a finite-element solution of the problem was published by Aanhold [1].

Switaiski [42] presented a complete procedure for pipeline design during the installation process. The first step in this procedure consists of the determination of the pipeline shape. This is accomplished using an elastic nonlinear beam equation, which is solved by an iterative numerical procedure. The solution for the catenary is used as the initial guess. Once the configuration is found, the longitudinal axial stresses are computed. In addition, the hoop stresses due to hydrostatic pressure are calculated, assuming a cross-sectional bending in the form of the first buckling mode. Then, the von Mises effective stress is compared with the yield stress. The same paper describes a process that estimates the dynamic effects of wave-pipe and wave-vessel interaction on the pipeline response. The effective stress computed from dynamic analysis is added to the static effective stress and their sum is compared with the yield stress.

Chapter 3

Continuum Mechanics Background

This chapter reviews the basics of continuum mechanics, necessary for the development of the numerical model described in the next section. The reader is assumed to have a background in vector calculus and linear algebra. An in-depth treatment of the topic can be found in the books of Gurtin [13] and Malvern [27].

3.1 Basics of Tensor Algebra and Analysis

A tensor is a linear function that maps the vector space $\mathcal{V}$ into itself, i.e. if $\boldsymbol{A}$ is a tensor, then $\boldsymbol{A} : \mathcal{V} \ni \boldsymbol{u} \longrightarrow \boldsymbol{v} \in \mathcal{V}$ and we write $\boldsymbol{v} = \boldsymbol{A}\boldsymbol{u}$. The tensor space is denoted by $\mathcal{L}$. Define addition and scalar magnification as follows:

$$\begin{array}{llcll} \forall \boldsymbol{A}, \boldsymbol{B} \in \mathcal{L}, & (\boldsymbol{A}+\boldsymbol{B})\boldsymbol{u} & = & \boldsymbol{A}\boldsymbol{u}+\boldsymbol{B}\boldsymbol{u}, & \forall \boldsymbol{u} \in \mathcal{V} \\ \forall \lambda \in \mathcal{R}, \boldsymbol{A} \in \mathcal{L}, & (\lambda \boldsymbol{A})\boldsymbol{u} & = & \lambda(\boldsymbol{A}\boldsymbol{u}), & \forall \boldsymbol{u} \in \mathcal{V} \end{array} \tag{3.1}$$

where $\mathcal{R}$ is the space of real numbers. The unit tensor $\boldsymbol{I}$ is defined such that

$$\boldsymbol{I}\boldsymbol{u} = \boldsymbol{u} \tag{3.2}$$

whereas the negative of a tensor $\boldsymbol{A} \in \mathcal{L}$ is the tensor $-\boldsymbol{A}$ such that

$$\boldsymbol{A} + (-\boldsymbol{A}) = (-\boldsymbol{A}) + \boldsymbol{A} = \boldsymbol{O} \tag{3.3}$$

where $\boldsymbol{O}$ is the zero tensor. Under these two operations $\mathcal{L}$ is a linear space. Define as the outer product of two vectors $\boldsymbol{u}, \boldsymbol{v} \in \mathcal{L}$ the tensor $\boldsymbol{u} \otimes \boldsymbol{v} \in \mathcal{L}$ such that

$$(\boldsymbol{u} \otimes \boldsymbol{v})\boldsymbol{w} = (\boldsymbol{v} \cdot \boldsymbol{w})\boldsymbol{u}, \forall \boldsymbol{w} \in \mathcal{V} \tag{3.4}$$

If $\{\boldsymbol{b}_k\}_{k=1,2,3}$ and $\{\boldsymbol{d}_m\}_{m=1,2,3}$ are bases of $\mathcal{V}$ then $\{\boldsymbol{b}_k \otimes \boldsymbol{d}_m\}$ is a basis of $\mathcal{L}$ in the sense that every tensor $\boldsymbol{A}$ can be written as a linear combination of these tensors. We write

$$\boldsymbol{A} = A^{km}(\boldsymbol{b}_k \otimes \boldsymbol{d}_m) \tag{3.5}$$

where A^{km} are called components of $\boldsymbol{A}$ with respect to the considered basis. Define the transpose of a tensor $\boldsymbol{A}$ the tensor $\boldsymbol{A}^T$ such that

$$(\boldsymbol{A}^T\boldsymbol{u})\boldsymbol{v} = (\boldsymbol{A}\boldsymbol{v})\boldsymbol{u}, \forall \boldsymbol{u}, \boldsymbol{v} \in \mathcal{V} \tag{3.6}$$

Define the composition of two tensors $\boldsymbol{A}, \boldsymbol{B}$ the tensor $\boldsymbol{AB}$ such that:

$$(\boldsymbol{AB})\boldsymbol{u} = \boldsymbol{A}(\boldsymbol{B}\boldsymbol{u}), \forall \boldsymbol{u} \in \mathcal{V} \tag{3.7}$$

Define the trace of a tensor $\boldsymbol{A} = A^{km}(\boldsymbol{b}_k \otimes \boldsymbol{d}_m)$ as the real number

$$tr(\boldsymbol{A}) = A^{km}(\boldsymbol{b}_k \cdot \boldsymbol{d}_m) \in \mathcal{R} \tag{3.8}$$

It can be shown that the value of the trace is independent of the basis chosen. Define the inner (scalar) product of tensors $\boldsymbol{A}$ and $\boldsymbol{B}$ as follows:

$$\boldsymbol{A} \cdot \boldsymbol{B} = tr(\boldsymbol{A}^T\boldsymbol{B}) = tr(\boldsymbol{B}^T\boldsymbol{A}) = \boldsymbol{B} \cdot \boldsymbol{A} \in \mathcal{R} \tag{3.9}$$

The components of tensor $\boldsymbol{A}$ with respect to the basis $\boldsymbol{b}_k \otimes \boldsymbol{d}_m$ are expressed as:

$$A^{km} = \boldsymbol{A} \cdot (\boldsymbol{b}^k \otimes \boldsymbol{d}^m) = (\boldsymbol{A}\boldsymbol{d}^m) \cdot \boldsymbol{b}^k \tag{3.10}$$

Define as the inverse of a tensor $\boldsymbol{A}$ the tensor $\boldsymbol{A}^{-1}$ which has the property:

$$\boldsymbol{A}^{-1}\boldsymbol{A} = \boldsymbol{A}\boldsymbol{A}^{-1} = \boldsymbol{I} \tag{3.11}$$

The determinant of a tensor $\boldsymbol{A}$ is the real number $det(\boldsymbol{A})$ defined as follows:

$$det(\boldsymbol{A}) = det[A^{km}]\, b\, d \tag{3.12}$$

where $b = \boldsymbol{b}_1 \cdot (\boldsymbol{b}_2 \times \boldsymbol{b}_3)$, $d = \boldsymbol{d}_1 \cdot (\boldsymbol{d}_2 \times \boldsymbol{d}_3)$ and $det[A^{km}]$ is the determinant of the matrix of the tensor components.

We make use of a Cartesian coordinate system x^1, x^2, x^3. Then the position vector of a point is

$$\boldsymbol{x} = \boldsymbol{x}(x^1, x^2, x^3) = x^k \boldsymbol{e}_k \tag{3.13}$$

where $\boldsymbol{e}_k$ is the orthonormal basis of the Cartesian system. Consider now the curvilinear system of coordinates ξ^1, ξ^2, ξ^3 defined by the functions

$$z^m = f^m(\xi^1, \xi^2, \xi^3),\ m = 1,2,3 \tag{3.14}$$

where

$$det[\frac{\partial f^m}{\partial \xi^k}] \neq 0 \tag{3.15}$$

Define covariant basis of the coordinate system ξ^1, ξ^2, ξ^3 the vectors

$$\boldsymbol{g}_k = \frac{\partial \boldsymbol{x}}{\partial \xi^k} = \frac{\partial f^m}{\partial \xi^k} \boldsymbol{e}_m \tag{3.16}$$

These vectors are tangent to the coordinate lines. Define the reciprocal basis vectors $\boldsymbol{g}^m$ such that

$$\boldsymbol{g}^m \cdot \boldsymbol{g}_k = \delta^m{}_k \tag{3.17}$$

where, $\delta^m{}_k$ is Kronecker's delta. If $d\boldsymbol{x}$ is the differential of the position vector, then

$$d\boldsymbol{x} = d\xi^k \boldsymbol{g}_k \tag{3.18}$$

Every tensor $\boldsymbol{A}$ can be written as

$$\boldsymbol{A} = A^{km}\boldsymbol{g}_k \otimes \boldsymbol{g}_m = A_{km}\boldsymbol{g}^k \otimes \boldsymbol{g}^m = A^k{}_m \boldsymbol{g}_k \otimes \boldsymbol{g}^m = A_k{}^m \boldsymbol{g}^k \otimes \boldsymbol{g}_m \tag{3.19}$$

In particular, the identity tensor $\boldsymbol{I}$ is written as

$$\boldsymbol{I} = g^{km}\boldsymbol{g}_k \otimes \boldsymbol{g}_m = g_{km}\boldsymbol{g}^k \otimes \boldsymbol{g}^m = \boldsymbol{g}_k \otimes \boldsymbol{g}^k = \boldsymbol{g}^m \otimes \boldsymbol{g}_m \tag{3.20}$$

where $g^{km} = \boldsymbol{g}^k \cdot \boldsymbol{g}^m$ and $g_{km} = \boldsymbol{g}_k \cdot \boldsymbol{g}_m$ are called contravariant and covariant metric coefficients respectively.

The gradient of a scalar point function $\phi(\boldsymbol{x})$ is defined as the vector function $\nabla_x \phi$ such that

$$d\phi = \nabla_x \phi \cdot d\boldsymbol{x} \tag{3.21}$$

With respect to a certain coordinate system,

$$\nabla_x \phi = \phi_{,k}\boldsymbol{g}^k \in \mathcal{V} \tag{3.22}$$

The gradient $\nabla_x \boldsymbol{u}$ of a vector point function $\boldsymbol{u}$ is a tensor defined as

$$d\boldsymbol{u} = [\nabla_x \boldsymbol{u}]d\boldsymbol{x} \tag{3.23}$$

With respect to a particular coordinate system,

$$\nabla_x \boldsymbol{u} = \boldsymbol{u}_{,k} \otimes \boldsymbol{g}^k \in \mathcal{L} \tag{3.24}$$

If $\boldsymbol{u}, \boldsymbol{T}$ are vector and tensor functions respectively, then their divergence is defined as

$$div\, \boldsymbol{u} = \boldsymbol{u}_{,k} \cdot \boldsymbol{g}^k = tr(\nabla_x \boldsymbol{u}) \in \mathcal{R} \tag{3.25}$$

and

$$div\, \boldsymbol{T} = \boldsymbol{T}_{,k}\, \boldsymbol{g}^k \in \mathcal{V} \tag{3.26}$$

Note that the divergence is independent of coordinate system.

3.2 Elements of Deformation and Stress Theory

Configuration $K(B)$ of a body B is a one-to-one mapping between the material points of the body and the points of the Eucledian space $\mathcal{E}$. A particular configuration $K_o(B)$, arbitrary but constant throughout deformation is chosen to be the "reference configuration". Deformation is defined as the one-to-one mapping of $K_o(B)$ onto $K(B)$. In our analysis, in order to describe the shell geometry, a "convected" curvilinear coordinate system ξ^1, ξ^2, ξ^3 is used, which is embedded in the continuum and deforms with it. Every point has three labels ξ^1, ξ^2, ξ^3 which remain constant throughout deformation. If $\boldsymbol{x}$ denotes the position vector, the covariant vector basis at the current configutation is

$$\boldsymbol{g}_k = \frac{\partial \boldsymbol{x}}{\partial \xi^k} \tag{3.27}$$

In particular, the position vector in the reference configuration is denoted by $\boldsymbol{X}$ and the covariant basis by $\boldsymbol{G}_k$. Clearly,

$$d\boldsymbol{X} = d\xi^k \boldsymbol{G}_k \tag{3.28}$$

The deformation gradient is defined as the tensor $\boldsymbol{F}$ such that:

$$d\boldsymbol{x} = \boldsymbol{F}\, d\boldsymbol{X} \tag{3.29}$$

The components of $\boldsymbol{F}$ with respect to the basis $\boldsymbol{G}^k \otimes \boldsymbol{G}^m$ are easily computed to be

$$F_{km} = \boldsymbol{g}_m \cdot \boldsymbol{G}_k \tag{3.30}$$

Note also that

$$\boldsymbol{g}_k = \boldsymbol{F}\boldsymbol{G}_k \tag{3.31}$$

Consider a volume element dV in the current configuration, represented as

$$dV = d\boldsymbol{x}_{(1)} \cdot (d\boldsymbol{x}_{(2)} \times d\boldsymbol{x}_{(3)}) \tag{3.32}$$

The same volume element is represented in the reference configuration as

$$dV_o = d\boldsymbol{X}_{(1)} \cdot (d\boldsymbol{X}_{(2)} \times d\boldsymbol{X}_{(3)}) \tag{3.33}$$

It can be easily shown that

$$dV = det(\boldsymbol{F}) dV_o \tag{3.34}$$

Consider now a surface element which is represented in the reference configuration as

$$\boldsymbol{n} dA = d\boldsymbol{x}_{(1)} \times d\boldsymbol{x}_{(2)} \tag{3.35}$$

and in the reference configuration as

$$\boldsymbol{n}_o dA_o = d\boldsymbol{X}_{(1)} \times d\boldsymbol{X}_{(2)} \tag{3.36}$$

It can be proved that

$$\boldsymbol{n} dA = det(\boldsymbol{F}) \boldsymbol{F}^{-T} \boldsymbol{n}_o dA_o \tag{3.37}$$

Consider the line element $d\boldsymbol{x}$ in the deformed configuration. Its length is given by the formula:

$$ds^2 = d\boldsymbol{x} \cdot d\boldsymbol{x} = (\boldsymbol{F} d\boldsymbol{X}) \cdot (\boldsymbol{F} d\boldsymbol{X}) = (\boldsymbol{F}^T \boldsymbol{F} d\boldsymbol{X}) \cdot d\boldsymbol{X} = (\boldsymbol{F}^T \boldsymbol{F}) \cdot (d\boldsymbol{X} \otimes d\boldsymbol{X}) \tag{3.38}$$

In the reference configuration, we have

$$ds_o{}^2 = d\boldsymbol{X}\cdot d\boldsymbol{X} = \boldsymbol{I}\cdot(d\boldsymbol{X}\otimes d\boldsymbol{X}) \tag{3.39}$$

Therefore,

$$ds^2 - ds_o{}^2 = (\boldsymbol{F}^T\boldsymbol{F} - \boldsymbol{I})\cdot(d\boldsymbol{X}\otimes d\boldsymbol{X}) = 2\boldsymbol{E}\cdot(d\boldsymbol{X}\otimes d\boldsymbol{X}) \tag{3.40}$$

where

$$\boldsymbol{E} = \frac{1}{2}(\boldsymbol{F}^T\boldsymbol{F} - \boldsymbol{I}) \tag{3.41}$$

is defined as the Cauchy strain tensor. The components of $\boldsymbol{E}$ with respect to the $\boldsymbol{G}^k \otimes \boldsymbol{G}^m$ basis are

$$E_{km} = \frac{1}{2}(g_{km} - G_{km}) \tag{3.42}$$

Define the material derivative of a scalar, vector or tensor function $\mathcal{F}$, as the change of the value of this function with respect to time (t) at a specific material point, i.e.

$$d\mathcal{F}|_{\boldsymbol{\xi}} = \dot{\mathcal{F}}\,dt \tag{3.43}$$

The velocity of a certain material point is defined as the material derivative of the position vector, i.e.

$$\boldsymbol{v} = \frac{\partial}{\partial t}[\boldsymbol{x}(\xi^1,\xi^2,\xi^3,t)] = \dot{\boldsymbol{x}} \tag{3.44}$$

The velocity gradient tensor $\boldsymbol{L}$ is defined as the gradient of the velocity field with respect to the spatial (current) position, i.e.

$$d\boldsymbol{v}|_t = \boldsymbol{L}d\boldsymbol{x} \tag{3.45}$$

Decompose $\boldsymbol{L}$ in a symmetric part $\boldsymbol{d}$ and a skew part $\boldsymbol{\omega}$, where

$$\boldsymbol{d} = \frac{1}{2}(\boldsymbol{L} + \boldsymbol{L}^T) \tag{3.46}$$

and

$$\boldsymbol{\omega} = \frac{1}{2}(\boldsymbol{L} - \boldsymbol{L}^T) \tag{3.47}$$

The components of $\boldsymbol{L}$ with respect to the $\boldsymbol{g}^k \otimes \boldsymbol{g}^m$ basis are

$$L_{km} = \frac{\partial \boldsymbol{v}}{\partial \xi^m} \cdot \boldsymbol{g}_k = v_{k|m} \tag{3.48}$$

Consequently, the components of $\boldsymbol{d}$ with respect to the same basis are

$$d_{km} = \frac{1}{2}(v_{k|m} + v_{m|k}) \tag{3.49}$$

Consider a point in the continuum and a surface passing through the point. Let $\boldsymbol{n}$ and $\boldsymbol{t}$ be respectively the unit normal to the surface and the traction at this specific point. Then, the Cauchy (true) stress tensor is defined as a tensor $\boldsymbol{\sigma}$ having the following property:

$$\boldsymbol{t} = \boldsymbol{\sigma}\boldsymbol{n} \tag{3.50}$$

Define $\hat{\boldsymbol{\sigma}}$ as the referential (nominal) stress tensor, such that

$$\boldsymbol{t}\, dA = \hat{\boldsymbol{\sigma}}\boldsymbol{n}_o dA_o \tag{3.51}$$

where subscript (o) refers to the reference configuration. It is easily proved that

$$\hat{\boldsymbol{\sigma}} = det(\boldsymbol{F})\boldsymbol{\sigma}\boldsymbol{F}^{-T} \tag{3.52}$$

Define also the Kirchhoff stress tensor

$$\boldsymbol{\tau} = \frac{dV}{dV_o}\boldsymbol{\sigma} = det(\boldsymbol{F})\boldsymbol{\sigma} \tag{3.53}$$

Finally, define the convected and the Jaumann rates of Kirchhoff stress as

$$\begin{aligned} \overset{\circ}{\boldsymbol{\tau}} &= \dot{\boldsymbol{\tau}} - \boldsymbol{\omega}\boldsymbol{\tau} + \boldsymbol{\tau}\boldsymbol{\omega} \\ \overset{\Delta}{\boldsymbol{\tau}} &= \dot{\boldsymbol{\tau}} - \boldsymbol{L}\boldsymbol{\tau} - \boldsymbol{\tau}\boldsymbol{L}^T \end{aligned} \tag{3.54}$$

The principle of virtual displacements is of particular importance in our analysis:

$$\int_V \nabla_x(\delta \boldsymbol{u})\cdot\boldsymbol{\sigma}\, dV = \int_B \delta \boldsymbol{u}\cdot\boldsymbol{t}\, dB \tag{3.55}$$

where V is the volume of the body, B is the boundary of the body, and $\delta \boldsymbol{u}$ is the virtual displacement field. As a result of the chain rule of differentiation,

$$\nabla_x(\delta \boldsymbol{u}) = \nabla_X(\delta \boldsymbol{u})\boldsymbol{F}^{-1} \tag{3.56}$$

Using the above equation and the fact that

$$\boldsymbol{\tau}\, dV_o = \boldsymbol{\sigma}\, dV \tag{3.57}$$

we can write the "referential" form of the principle of virtual displacements:

$$\int_{V_o} [\nabla_X(\delta \boldsymbol{u})\boldsymbol{F}^{-1}]\cdot\boldsymbol{\tau}\, dV_o = \int_B \delta \boldsymbol{u}\cdot\boldsymbol{t}\, dB \tag{3.58}$$

or

$$\int_{V_o} \delta U_{k|j}(\boldsymbol{G}^k\cdot\boldsymbol{g}_i)\tau^{ij} dV_o = \int_B \delta \boldsymbol{u}\cdot\boldsymbol{t}\, dB \tag{3.59}$$

where,

$$\delta U_{k|j} = \frac{\partial(\delta \boldsymbol{u})}{\partial \xi^j}\cdot\boldsymbol{G}_k \tag{3.60}$$

and τ^{ij} are the components of the Kirchhoff stress tensor with respect to the $\boldsymbol{G}_i \otimes \boldsymbol{G}_j$ basis.

3.3 Material Behavior

For the modeling of the material behavior, the J_2-incremental theory of plasticity is adopted. To describe the post-yielding behavior, isotropic hardening is employed. It is worth mentioning that in the recent work of

Corona and Kyriakides[7], this simple hardening model performed remarkably well.

The constitutive equations relate the Jaumann rate of Kirchoff stress to the rate of deformation. The deviatoric Kirchoff stress tensor is defined as

$$\boldsymbol{s} = \boldsymbol{\tau} - \frac{1}{3}(\boldsymbol{\tau} \cdot \boldsymbol{I})\boldsymbol{I} \tag{3.61}$$

Its components with respect to the current basis

$$s^{ij} = \tau^{ij} - \frac{1}{3} g^{ij} g_{km} \tau^{km} \tag{3.62}$$

We define the von Mises (effective) stress as

$$Y = \sqrt{\frac{3}{2}\, \boldsymbol{s} \cdot \boldsymbol{s}} = \sqrt{\frac{3}{2} g_{ik} g_{jm} s^{ij} s^{km}} \tag{3.63}$$

The loading criterion is

$$Y = Y_{max} \quad \text{and} \quad \dot{Y} > 0 \tag{3.64}$$

where Y_{max} is equal to the maximum value of Y throughout the deformation history but not less than $Y_{max,o}$ which is the initial yielding value for the the case of uniaxial tension. It is assumed that the material obeys the normality rule imposed by the Drucker's postulate of stability. Then, if $\boldsymbol{d}^p$ is the plastic part of the rate-of-deformation tensor,

$$\boldsymbol{d}^p = \frac{3}{2}\frac{\dot{d}_p}{Y}\boldsymbol{s} \tag{3.65}$$

where it can be easily shown that

$$d_p = \int_o^t \sqrt{\frac{2}{3}\boldsymbol{d}^p \cdot \boldsymbol{d}^p}\, dt \tag{3.66}$$

The above equation indicates that d_p is a measure of the total plastic deformation. Based on this observation, we assume that Y_{max} is a monotonically increasing function of d_p. The function is found from the uniaxial stress-strain curve and this procedure is outlined at the end of the section. During elasto-plastic loading, $Y = Y_{max}$. Therefore

$$\dot{Y} = \dot{Y}_{max} \text{ and } \dot{Y} = \frac{dY_{max}}{dd_p}\dot{d}_p \tag{3.67}$$

It can be shown that the differentiation of Eq.3.63 gives

$$\dot{Y} = \frac{3}{2Y}\boldsymbol{s}\cdot\overset{\Delta}{\boldsymbol{\tau}} \tag{3.68}$$

Furthermore,

$$\overset{\Delta}{\boldsymbol{\tau}} = \boldsymbol{\mathcal{E}}(\boldsymbol{d} - \boldsymbol{d}^p) \tag{3.69}$$

where $\boldsymbol{\mathcal{E}}$ is the fourth-order, elastic rigidity tensor whose components in the current basis are given by

$$\mathcal{E}^{ijkl} = \frac{E}{2(1+\nu)}\left[(g^{ik}g^{jl} + g^{il}g^{jk}) + \frac{2\nu}{1-2\nu}g^{ij}g^{kl}\right] \tag{3.70}$$

Using Eqs. 3.69, 3.68, 3.67, 3.65 and after some manipulations we get

$$\overset{\Delta}{\boldsymbol{\tau}} = \boldsymbol{\mathcal{D}}\boldsymbol{d} \tag{3.71}$$

where $\boldsymbol{\mathcal{D}}$ is a fourth-order tensor whose contravariant components with respect to the current basis are

$$\mathcal{D}^{ijkm} = \mathcal{E}^{ijkm} - \frac{3G}{Y^2}\frac{1}{1+\frac{H}{3G}}s^{ij}s^{km} \tag{3.72}$$

and $H = \frac{dY_{max}}{dd_p}$. Concequently, the convected rate of Kirchoff stress is found to be

$$\overset{\circ}{\boldsymbol{\tau}} = \boldsymbol{\mathcal{R}}\boldsymbol{d} = (\boldsymbol{\mathcal{D}} - \boldsymbol{\mathcal{L}})\boldsymbol{d} = \tag{3.73}$$

where the contravariant components of tensor $\mathcal{L}$ are computed to be

$$\mathcal{L}^{ijkm} = \frac{1}{2}(g^{ik}\tau^{jm} + g^{jk}\tau^{im} + g^{im}\tau^{jk} + g^{jm}\tau^{ik}) \tag{3.74}$$

It is notable that the components of tensor $\mathcal{R}$ exhibit the symmetries $R^{ijkm} = R^{jikm}$, $R^{ijkm} = R^{ijmk}$ (due to the symmetry of $\overset{\circ}{\boldsymbol{\tau}}$ and $\boldsymbol{d}$) and $R^{ijkm} = R^{kmij}$.

To complete the development of the constitutive equations, the function $Y_{max}(d_p)$ must be defined. In our work, this function is extracted from the uniaxial tension stress-strain curve. Assume that the uniaxial curve $\hat{\sigma}$ versus $\hat{\epsilon}$ is known, where $\hat{\sigma}$ is the nominal stress, $\hat{\epsilon}$ is the nominal strain. If P is the applied load, L_o, L are the initial and current bar lengths respectively, $\Delta L = L - L_o$ and A_o, A are the initial and current cross-sectional areas respectively, we have:

- axial nominal stress

$$\hat{\sigma} = \frac{P}{A_o}$$

- axial nominal strain

$$\hat{\epsilon} = \frac{\Delta L}{L_o}$$

- axial Cauchy stress

$$\sigma = \frac{P}{A} = \hat{\sigma}\frac{A_o}{A}$$

- axial Kirchhoff stress

$$\tau = \frac{V}{V_o}\sigma = \frac{L}{L_o}\hat{\sigma} = (1 + \hat{\epsilon})\hat{\sigma}$$

- deviatoric Kirchhoff stress components

$$\begin{aligned} s_{11} &= \tfrac{2}{3}\tau \\ s_{22} &= s_{33} = -\tfrac{1}{3}\tau \\ s_{ij} &= 0 \quad , \quad i \neq j \end{aligned}$$

- von Mises stress

$$Y = \tau = (1 + \hat{\epsilon})\hat{\sigma} \tag{3.75}$$

- plastic rate-of-deformation stress components

$$\begin{aligned} d^p_{11} &= d^p_{11} \\ d^p_{22} &= d^p_{33} = -\tfrac{1}{2}d^p_{11} \\ d^p_{ij} &= 0 \quad , \quad i \neq j \end{aligned}$$

- total rate-of-deformation in the axial direction

$$d_{11} = \frac{dL/L}{dt}$$

- elastic rate-of-deformation in the axial direction

$$d^e_{11} = \frac{\dot{\tau}}{E}$$

- plastic deformation parameter

$$\dot{d}_p = d^p_{11}$$

of course,

$$d^p_{11} = d_{11} - d^e_{11}$$

and, therefore,

$$\dot{d}_p = \frac{dL}{dt}\frac{1}{L} - \frac{\dot{\tau}}{E}$$

Integration of this quantity gives

$$d_p = ln(1 + \hat{\epsilon}) - (1 + \hat{\epsilon})\frac{\hat{\sigma}}{E} \tag{3.76}$$

Eqs. 3.75 and 3.76 give Y_{max} and d_p in terms of $\hat{\sigma}$ and $\hat{\epsilon}$.

Chapter 4

Finite Element Technique

In this chapter, the implementation of the finite element used in the present study is described. The formulation employs the finite element method through a nine-node isoparametric shell element (*degenerated shell element*) introduced by Ahmad et al. [3] for the linear analysis of moderately thick and thin shells. A multilayered version of this element is employed and permits the simulation of pipes of arbitrary thickness. The analysis is based on the principle of virtual work in the form of equation 3.59 and the elastoplastic constitutive equation 3.73 relating the convected rate of Kirchhoff stress to the rate-of-deformation tensor. A "pressure node" is used, as in the work of Katsounas and Tassoulas [18] and Song and Tassoulas [39],in order to facilitate the tracing of equilibrium paths involving pressure limit points. Finally, the boundary conditions of the problem are imposed through kinematic constraints, which are implemented using auxiliary elements.

4.1 Nine-Node Isoparametric Shell Element

The finite element employed in our analysis is depicted in Figure 4.1. The nodes of the element have been located on the interior surface of the shell. Let $\boldsymbol{x}^{(k)}$ denote the position vector of node (k) of a typical quadrilateral shell element in the current configuration. Associated with each node is a

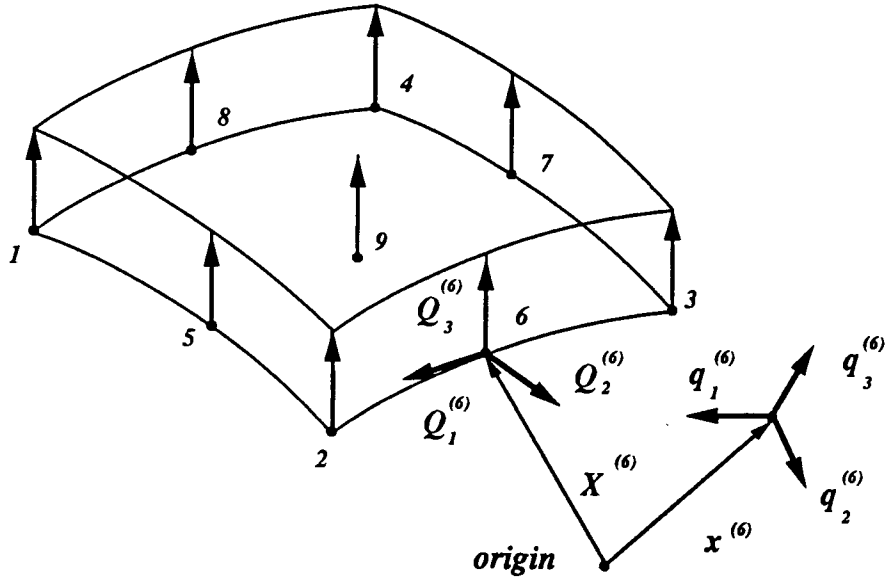

Figure 4.1: Nine-node isoparametric shell element.

vector, identified by $\boldsymbol{q}_3^{(k)}$ in Figure 4.1, extending, through the thickness, to the exterior surface of the element. The magnitude of this vector is taken equal to the thickness of the shell, possibly varying from node to node, but constant during deformation, i.e., the vectors undergo only rigid-body motion. The material (convected) coordinates (ξ^1, ξ^2, ξ^3) are chosen so that the element is mapped onto the parallelepiped $-1 \leq \xi^1 \leq 1$, $-1 \leq \xi^2 \leq 1$, and $0 \leq \xi^3 \leq 1$ (see Figure 4.2). Using Lagrangian quadratic interpolation with respect to ξ^1 and ξ^2, and linear interpolation with respect to ξ^3, the geometry of the element can be expressed as

$$\boldsymbol{x}(\xi^1, \xi^2, \xi^3) = \sum_{k=1}^{9} [(\boldsymbol{x}^{(k)} + \xi^3 \boldsymbol{q}_3^{(k)}) N^{(k)}(\xi^1, \xi^2)] \tag{4.1}$$

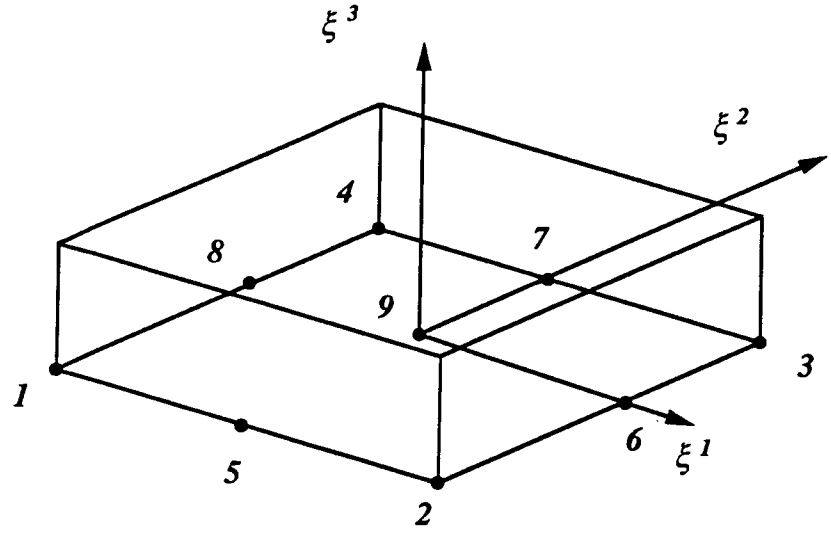

Figure 4.2: Material (convected) coordinate system.

where $N^{(k)}$, $k = 1, \cdots, 9$, are the nodal Lagrangian shape functions (see the book by Zienkiewicz [47]). For ξ^3 fixed, the surface defined by Eq. 4.1 is referred to as *lamina*; for ξ^1, ξ^2 fixed, the line defined by Eq. 4.1 is a *fiber*. Note that $\xi^3 = 0$ is the surface on which the nodes of the element are located and $\xi^3 = 1$ is the exterior pipe surface.

The velocity can be written as

$$\boldsymbol{v}(\xi^1, \xi^2, \xi^3) = \sum_{k=1}^{9} [(\boldsymbol{v}^{(k)} + \xi^3 \dot{\boldsymbol{q}}_3^{(k)}) N^{(k)}(\xi^1, \xi^2)] \tag{4.2}$$

where $\boldsymbol{v}^{(k)}$ denotes the velocity of node k and $\dot{\boldsymbol{q}}_3^{(k)}$ is the rate of change of $\boldsymbol{q}_3^{(k)}$.

In order to monitor the motion of $\boldsymbol{q}_3^{(k)}$, two mutually orthogonal vectors $\boldsymbol{q}_1^{(k)}$, $\boldsymbol{q}_2^{(k)}$ of the same magnitude as $\boldsymbol{q}_3^{(k)}$ and orthogonal to $\boldsymbol{q}_3^{(k)}$ are selected. If we denote by $\hat{\boldsymbol{q}}_m^{(k)}$, $(m = 1, 2, 3)$ the unit vector in the direction of

$\boldsymbol{q}_m^{(k)}$ and by $\omega_1^{(k)}$ and $\omega_2^{(k)}$ the angular velocities with respect to the axes in the direction of $\hat{\boldsymbol{q}}_1^{(k)}$ and $\hat{\boldsymbol{q}}_2^{(k)}$, then

$$\dot{\boldsymbol{q}}_3^{(k)} = \omega_1^{(k)}\hat{\boldsymbol{q}}_1^{(k)} \times \boldsymbol{q}_3^{(k)} + \omega_2^{(k)}\hat{\boldsymbol{q}}_2^{(k)} \times \boldsymbol{q}_3^{(k)} \tag{4.3}$$

Vectors $\hat{\boldsymbol{q}}_m^{(k)}$ obey the right-hand rule, i.e.,

$$\hat{\boldsymbol{q}}_1^{(k)} \times \hat{\boldsymbol{q}}_2^{(k)} = \hat{\boldsymbol{q}}_3^{(k)} \tag{4.4}$$

Therefore, Eq. 4.3 can be rewritten as

$$\dot{\boldsymbol{q}}_3^{(k)} = -\omega_1^{(k)}\boldsymbol{q}_2^{(k)} + \omega_2^{(k)}\boldsymbol{q}_1^{(k)} \tag{4.5}$$

and Eq. 4.2 becomes

$$\boldsymbol{v}(\xi^1,\xi^2,\xi^3) = \sum_{k=1}^{9}[(\boldsymbol{v}^{(k)} - \omega_1^{(k)}\xi^3\boldsymbol{q}_2^{(k)} + \omega_2^{(k)}\xi^3\boldsymbol{q}_1^{(k)})N^{(k)}(\xi^1,\xi^2)] \tag{4.6}$$

The same interpolation is used for the incremental displacements, i.e., $\Delta\boldsymbol{u}$ is taken as

$$\Delta\boldsymbol{u}(\xi^1,\xi^2,\xi^3) = \sum_{k=1}^{9}[(\Delta\boldsymbol{u}^{(k)} - \Delta\theta_1^{(k)}\xi^3\boldsymbol{q}_2^{(k)} + \Delta\theta_2^{(k)}\xi^3\boldsymbol{q}_1^{(k)})N^{(k)}(\xi^1,\xi^2)] \tag{4.7}$$

where $\Delta\boldsymbol{u}^{(k)}$ (three components), $\Delta\theta_1^{(k)}$, $\Delta\theta_2^{(k)}, k = 1,\ldots,9$, are the nodal displacements and rotations.

In order to simulate tubes of arbitrary thickness, a multilayered version of the shell element is employed (Figure 4.3). The same interpolation for the geometry and the displacements is used. However, there are two degrees of freedom associated with each node of the additional layer, namely, the angular velocities $\omega_1^{(k)}$ and $\omega_2^{(k)}$, which monitor the motion of vector $\boldsymbol{q}_3^{(k)}$, $k = 10,\ldots,18$.

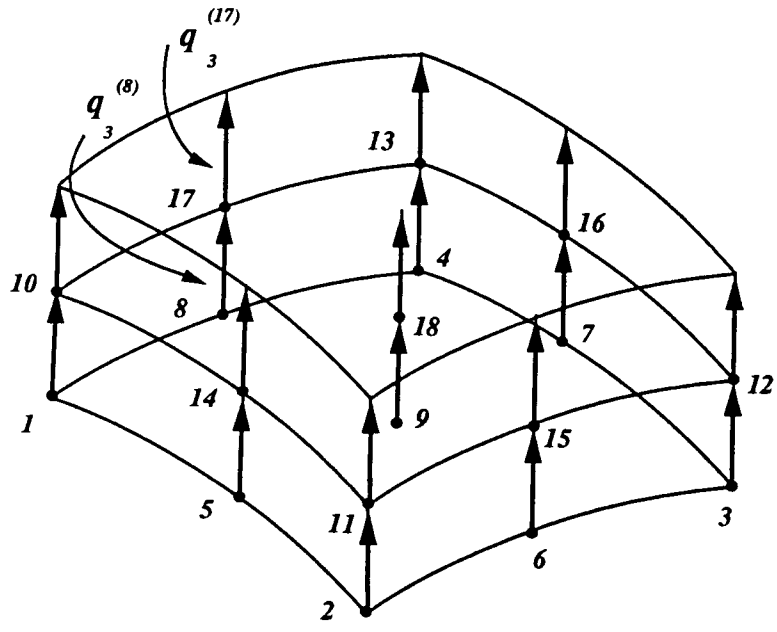

Figure 4.3: Multilayered shell element.

For the purpose of applying equilibrium, the principle of virtual displacements is considered in a nearby configuration $\boldsymbol{x}'$

$$\int_{V_o} \delta U'_{k|j} (\boldsymbol{G}^k \cdot \boldsymbol{g}'_i) \tau'^{ij} dV_o = \int_{B'} \delta \boldsymbol{u}' \cdot \boldsymbol{t}' \, dB' \tag{4.8}$$

It can be shown [18] and [39] that this equation using the constitutive equation 3.73 and keeping the linear terms reduces to

$$\begin{aligned} & \int_{V_o} \delta U_{n|j} (\boldsymbol{G}^n \cdot \boldsymbol{g}_i) R^{ijkl} (\boldsymbol{G}^m \cdot \boldsymbol{g}_k) \Delta U_{m|l} dV_o \\ + & \int_{V_o} \delta U_{n|j} \tau^{ij} G^{nl} \Delta U_{l|i} dV_o \\ = & \int_B \delta \boldsymbol{u} \cdot \boldsymbol{t}' dB - \int_{V_o} \delta U_{i|j} \hat{\sigma}^{ji} \, dV_o \end{aligned} \tag{4.9}$$

where R^{ijkl} are the components of the fourth-order tensor $\boldsymbol{R}$ in the current basis, whereas $\Delta U_{i|j}$ and $\delta U_{i|j}$ are the components of the incremental and

virtual displacement vectors respectively on the reference basis. If we define

$$S^{ijkl} = (\boldsymbol{G}^i \cdot \boldsymbol{g}_n) R^{njml} (\boldsymbol{G}^k \cdot \boldsymbol{g}_m) + \tau^{jl} G^{ik} \tag{4.10}$$

then Eq. 4.9 becomes

$$\begin{aligned} &\int_{V_o} \delta U_{i|j} S^{ijkl} \Delta U_{k|l} \, dV_o \\ &= \int_B \delta \boldsymbol{u} \cdot \boldsymbol{t}' \, dB - \int_{V_o} \delta U_{i|j} \hat{\sigma}^{ji} \, dV_o \end{aligned} \tag{4.11}$$

where $\Delta \boldsymbol{u}^{(k)}$ (three components), $\Delta\theta_1^{(k)}$, $\Delta\theta_2^{(k)}, k = 1, \ldots, 9$, are the nodal displacements and rotations.

From the computational point of view, a matrix representation of Eq. 4.11 is preferable for the solution process in a compact and elegant manner. For every element, the 45-component column vector of nodal displacements and rotations is defined as

$$\mathbf{\Delta U} = \begin{bmatrix} \vdots \\ \Delta u_1^{(k)} \\ \Delta u_2^{(k)} \\ \Delta u_3^{(k)} \\ \Delta\theta_1^{(k)} \\ \Delta\theta_2^{(k)} \\ \vdots \end{bmatrix} \tag{4.12}$$

where the subscripts in parentheses indicate components with respect to a (global) rectangular Cartesian system. The 45-component column vector of virtual nodal displacements and rotations is defined similarly and denoted by $\delta\mathbf{U}$. The column vector containing the components of the gradient of the

incremental displacements in the reference basis is arranged as

$$grad\left(\boldsymbol{\Delta u}\right) = \begin{bmatrix} \Delta U_{1|1} \\ \Delta U_{2|1} \\ \Delta U_{3|1} \\ \Delta U_{1|2} \\ \Delta U_{2|2} \\ \Delta U_{3|2} \\ \Delta U_{1|3} \\ \Delta U_{2|3} \\ \Delta U_{3|3} \end{bmatrix} \tag{4.13}$$

The column vector containing the components of the gradient of $\boldsymbol{\delta u}$ is arranged similarly and will be denoted by $grad(\boldsymbol{\delta u})$. Using Eq. 4.7, the increment of displacement at any material point can be expressed as

$$\boldsymbol{\Delta u} = \mathbf{N}\boldsymbol{\Delta U} \tag{4.14}$$

in which $\mathbf{N}$ is a 3×45 matrix. Differentiating Eq. 4.14 and taking components on the reference base vectors, one finds

$$grad(\boldsymbol{\Delta u}) = \mathbf{B}\boldsymbol{\Delta U} \tag{4.15}$$

where $\mathbf{B}$ is a 9×45 matrix. Likewise,

$$\boldsymbol{\delta u} = \mathbf{N}\boldsymbol{\delta U} \tag{4.16}$$

and

$$grad(\boldsymbol{\delta u}) = \mathbf{B}\boldsymbol{\delta U} \tag{4.17}$$

Recall the mixed components of the deformation gradient on the reference base vectors:

$$F^i_{\cdot j} = \boldsymbol{F}\cdot(\boldsymbol{G}^i \otimes \boldsymbol{G}_j) = (\boldsymbol{F}\boldsymbol{G}_j)\cdot\boldsymbol{G}^i = \boldsymbol{G}^i\cdot\boldsymbol{g}_j \tag{4.18}$$

An auxiliary 5×9 matrix $\mathbf{W}$ containing these components is defined as

$$\mathbf{W} = \begin{bmatrix} F^1_{.1} & F^2_{.1} & F^3_{.1} & 0 & 0 & 0 & 0 & 0 & 0 \\ 0 & 0 & 0 & F^1_{.2} & F^2_{.2} & F^3_{.2} & 0 & 0 & 0 \\ F^1_{.2} & F^2_{.2} & F^3_{.2} & F^1_{.1} & F^2_{.1} & F^3_{.1} & 0 & 0 & 0 \\ 0 & 0 & 0 & F^1_{.3} & F^2_{.3} & F^3_{.3} & F^1_{.2} & F^2_{.2} & F^3_{.2} \\ F^1_{.3} & F^2_{.3} & F^3_{.3} & 0 & 0 & 0 & F^1_{.1} & F^2_{.1} & F^3_{.1} \end{bmatrix} \tag{4.19}$$

On account of the symmetry of the Kirchhoff stress and $\tau^{33} = 0$, the 5-component column vector of stress components is taken as

$$\mathcal{T} = \begin{bmatrix} \tau^{11} \\ \tau^{22} \\ \tau^{12} \\ \tau^{23} \\ \tau^{31} \end{bmatrix} \tag{4.20}$$

Applying the condition that $\dot{\tau}^{33} = 0$ (since $\tau^{33} = 0$ at all times), Eq. 3.73 relating the convected rate of Kirchhoff stress to the stretching can be written in matrix form as:

$$\dot{\mathcal{T}} = \mathbf{R}\mathbf{d} \tag{4.21}$$

in which

$$\dot{\mathcal{T}} = \begin{bmatrix} \dot{\tau}^{11} \\ \dot{\tau}^{22} \\ \dot{\tau}^{12} \\ \dot{\tau}^{23} \\ \dot{\tau}^{31} \end{bmatrix} \quad , \qquad \mathbf{d} = \begin{bmatrix} d^{11} \\ d^{22} \\ d^{12} \\ d^{23} \\ d^{31} \end{bmatrix} \tag{4.22}$$

and $\mathbf{R}$ is a 5×5 matrix. On the basis of the symmetries of the components R^{ijkl} in Eq. 3.73, it can be shown that $\mathbf{R}$ is symmetric. Another auxiliary matrix $\mathbf{C}$ (9×9), is defined so that

$$C_{IJ} = \tau^{j(I)l(J)} G^{i(I)k(J)} \tag{4.23}$$

where the relationship between the indices is given by

I , J	i *or* k	j *or* l
1	1	1
2	2	1
3	3	1
4	1	2
5	2	2
6	3	2
7	1	3
8	2	3
9	3	3

(4.24)

This arrangement is consistent with that of the gradient components in Eq. 4.13. It is easily checked that $\mathbf{C}$ is symmetric from $\tau^{jl}G^{ik} = \tau^{lj}G^{ki}$. Finally, define $\mathbf{S}$ (9×9) as

$$\mathbf{S} = \mathbf{W}^T\mathbf{R}\mathbf{W} + \mathbf{C} \tag{4.25}$$

Using the matrices and column vectors given above, the contribution of the element to the left-hand side of Eq. 4.11 can be written as

$$\delta\mathbf{U}^T \left[\int_{V_o^e} \mathbf{B}^T\mathbf{S}\mathbf{B}\, dV_o^e \right] \Delta\mathbf{U} \tag{4.26}$$

while its contribution to the right-hand side is

$$-\delta\mathbf{U}^T \left[\int_{V_o^e} \mathbf{B}^T\mathbf{W}^T\boldsymbol{\tau}\, dV_o^e \right] \tag{4.27}$$

where V_o^e is the domain of the element in the reference configuration. Thus, the tangent stiffness matrix is given by

$$\mathbf{K^e} = \int_{V_o^e} \mathbf{B}^T\mathbf{S}\mathbf{B}\, dV_o^e \tag{4.28}$$

while the element internal load vector is:

$$\mathbf{P^e}_{int} = \int_{V_o^e} \mathbf{B}^T \mathbf{W}^T \tau \, dV_o^e \tag{4.29}$$

After assembling the stiffness matrices and load vectors of all elements, the system of equations for the displacement increment is solved. Upon computing the displacement increment, the corresponding increments of strain and stress are calculated, and, thus, an estimate of the nearby state of equilibrium is obtained.

Reduced integration (2 by 2 array of Gauss-Legendre points) is employed on every lamina of the element for the evaluation of the stiffness matrix and load vector. An array of 5 Gauss-Legendre points is used through the thickness (in each layer). It is well known that, in general, this under-integrated element is handicapped by spurious modes of deformation ("zero energy" modes). However, the boundary conditions of interest in the present study are such that these modes are not allowed and the element performs very well. The integration of the constitutive equations is based on the well-known radial return method, which employs the backward Euler substitution. For a detailed description of this procedure, the reader is reffered to the the work of Katsounas and Tassoulas [18].

4.2 Pressure Node

An important feature of the present formulation is the use of an auxiliary node so as to overcome points of limit pressure along equilibrium paths of tubes. The implementation of this "pressure node" is given by Katsounas and Tassoulas [18] and Song and Tassoulas [39] and is included here

for the sake of completeness. There is one degree of freedom for this node: the increment of pressure Δp. The node is appended to the usual array of nodes of each element. For the problems of concern in the present investigation, the pressure node is common to all elements. The "load" associated with the node is the volume-like increment:

$$\Delta\hat{V} = \int_B \Delta\boldsymbol{u}\cdot\boldsymbol{n}\,dB = \sum_e \int_{B^e} \Delta\boldsymbol{u}\cdot\boldsymbol{n}\,dB^e = \sum_e \left(\int_{B^e} \mathbf{n}^T\mathbf{N}\; dB^e \right) \boldsymbol{\Delta}\mathbf{U} \tag{4.30}$$

$\boldsymbol{n}$ being the unit vector normal to the element boundary B^e at $\boldsymbol{x}$. The assembled incremental equations can be rewritten as

$$\mathbf{K}\,\boldsymbol{\Delta}\mathbf{U} = \mathbf{P}_{ext} - \Delta p \int_B \mathbf{N}^T\mathbf{n}\,dB - \mathbf{P}_{int} \tag{4.31}$$

where the traction due to Δp is approximated by $-\Delta p\,\boldsymbol{n}$ and $\mathbf{P}_{ext}$ is the load vector corresponding to boundary tractions other than those due to the pressure. Combining Eqs. 4.30 and 4.31 one finds:

$$\begin{bmatrix} \mathbf{K} & \int_B \mathbf{N}^T\mathbf{n}\,dB \\ \int_B \mathbf{n}^T\mathbf{N}\,dB & 0 \end{bmatrix} \begin{bmatrix} \boldsymbol{\Delta}\mathbf{U} \\ \Delta p \end{bmatrix} = \begin{bmatrix} \mathbf{P}_{ext} - \mathbf{P}_{int} \\ \Delta\hat{V} \end{bmatrix} \tag{4.32}$$

It is seen that the inclusion of the pressure node has a symmetric contribution to the system matrix which can be assembled element-by-element along with the stiffness matrix. The presence of $\Delta\hat{V}$ on the right-hand side of Eq. 4.32 indicates that one can prescribe the volume-like change and determine the required increase or decrease in pressure. This is important in "driving" the solution around limit points of pressure, where Δp changes sign while $\Delta\hat{V}$ remains negative.

4.3 Three-Dimensional Analysis

In order to simulate the typical experimental procedure, a three-dimensional analysis of a nine-diameter-long pipe segment is conducted. This is in the range of lengths used in experiments [11]. The pipe cross section is assumed to be initially doubly-symmetric. A global Cartesian coordinate system (x_1,x_2,x_3) is used: x_3 is the longitudinal axis of the pipe while x_1 is the symmetry of axis of symmetry of the cross section. Only one quarter of the pipe, i.e., $0 < x_3 < L/2$ and $x_2 > 0$, is analyzed because of the symmetries with respect to the planes $x_3 = L/2$ and $x_2 = 0$. The discretization consists of an array of 9-node elements, each of length $D/4$ (in the x_3 direction) and occupying a sector of angle $\pi/6$ in the undeformed configuration of the pipe. This is a 6 by 18 mesh of elements for a quarter of the pipe. These mesh characteristics were also adopted by Katsounas and Tassoulas [18] with very good results. In some experiments, the pressurized pipes are subjected to end rotations through rigid plates which are rigidly connected to the ends of the segment (Figure 4.4). In order to simulate this condition, let (e) denote the node (a reference point) on the end plate at $x_3 = 0$. At this node, three orthonormal fixed-in-the-plate vectors $\boldsymbol{e}_1$, $\boldsymbol{e}_2$, $\boldsymbol{e}_3$ are selected, initially in the directions of the x_1, x_2 and x_3 axes. To describe the motion of the plate, the node has three degrees of freedom: $\Delta u_1^{(e)}$, $\Delta u_3^{(e)}$(translations in the x_1 and x_3 directions) and $\Delta\theta_2^{(e)}$ (rotation with respect to $\boldsymbol{e}_2$). Clearly, $\boldsymbol{e}_2$ coincides with $\boldsymbol{x}_2$ throughout deformation. Consider a shell element node (k) located on the end section (Figure 4.5). The associated vectors and degrees of freedom are $\boldsymbol{q}_1^{(k)}$, $\boldsymbol{q}_2^{(k)}$,$\boldsymbol{q}_3^{(k)}$ and $\Delta u_1^{(k)}$,$\Delta u_2^{(k)}$,$\Delta u_3^{(k)}$, $\Delta\theta_1^{(k)}$, $\Delta\theta_2^{(k)}$. In order to ensure that the plate is "welded" on the end section the following kinematic constraints must

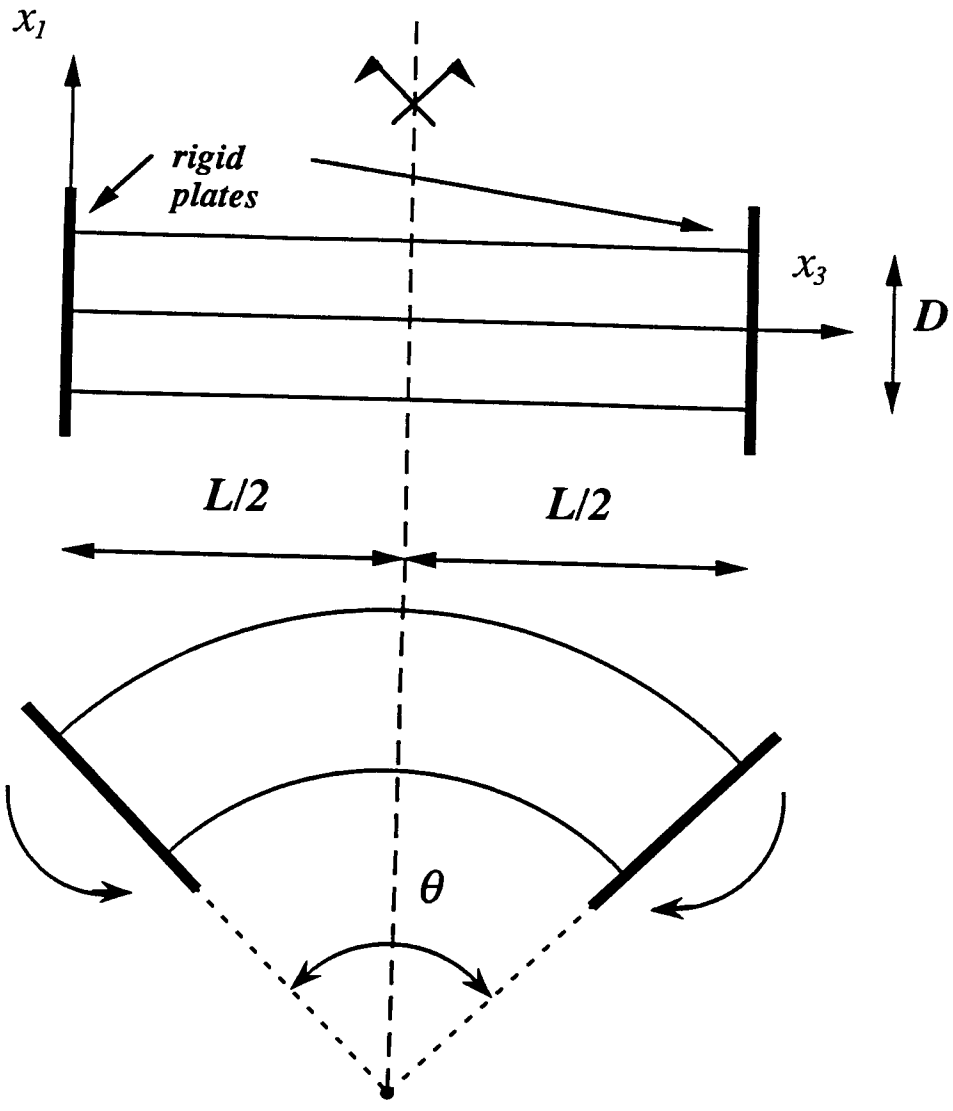

Figure 4.4: Schematic representation of experimental procedure.

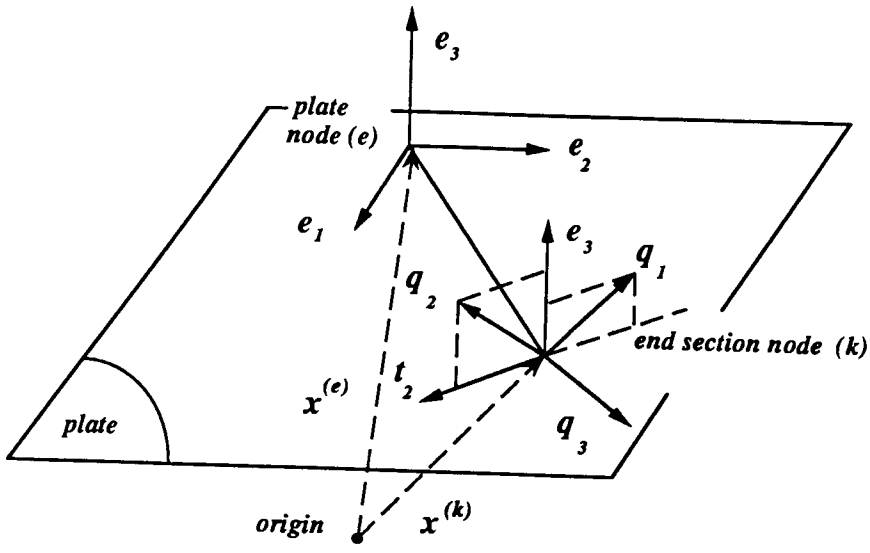

Figure 4.5: End section node and plate node vectors.

be considered:

$$\begin{aligned}
\Delta u_1^{(k)} &= \Delta u_1^{(e)} + (\boldsymbol{e}_2 \times [\boldsymbol{x}^{(k)} - \boldsymbol{x}^{(e)}])\cdot\boldsymbol{x}_1 \, \Delta\theta_2^{(e)} \\
\Delta u_2^{(k)} &= (\boldsymbol{e}_2 \times [\boldsymbol{x}^{(k)} - \boldsymbol{x}^{(e)}])\cdot\boldsymbol{x}_2 \, \Delta\theta_2^{(e)} \\
\Delta u_3^{(k)} &= \Delta u_3^{(e)} + (\boldsymbol{e}_2 \times [\boldsymbol{x}^{(k)} - \boldsymbol{x}^{(e)}])\cdot\boldsymbol{x}_3 \, \Delta\theta_2^{(e)} \\
\Delta\theta_1^{(k)} &= \boldsymbol{e}_2\cdot\hat{\boldsymbol{q}}_1^{(k)} \, \Delta\theta_2^{(e)} \\
\Delta\theta_2^{(k)} &= \boldsymbol{e}_2\cdot\hat{\boldsymbol{q}}_2^{(k)} \, \Delta\theta_2^{(e)}
\end{aligned} \tag{4.33}$$

where $\boldsymbol{x}^{(k)}$, $\boldsymbol{x}^{(e)}$ are the positions of nodes (k) and (e), while $\boldsymbol{x}_1$, $\boldsymbol{x}_2$, $\boldsymbol{x}_3$, denote unit vectors along the coordinate axes. These conditions are imposed for all shell element nodes on the end plate, and can be written in a matrix form as

$$\boldsymbol{\Delta U}^{(k)} = \mathbf{C}\boldsymbol{\Delta U}^{(e)} \tag{4.34}$$

The non-zero components of $\mathbf{C}$ (5×6) are

$$\begin{aligned} C_{11} &= C_{22} = C_{33} = 1 \\ C_{m5} &= (\boldsymbol{e}_2 \times [\boldsymbol{x}^{(k)} - \boldsymbol{x}^{(e)}]) \cdot \boldsymbol{x}_m \quad , \; m = 1,2,3 \\ C_{45} &= \boldsymbol{e}_2 \cdot \hat{\boldsymbol{q}}_1^{(k)} \\ C_{55} &= \boldsymbol{e}_2 \cdot \hat{\boldsymbol{q}}_2^{(k)} \end{aligned} \tag{4.35}$$

Denote by $\mathbf{P}^{(k)}$ and $\mathbf{P}^{(e)}$ the load vectors that correspond to nodes (k) and (e) respectively. It can be easily shown that

$$\mathbf{P}^{(e)} = \mathbf{C}^T \mathbf{P}^{(k)} \tag{4.36}$$

Consequently, the auxiliary element matrix is:

$$\begin{bmatrix} \mathbf{0} & -\mathbf{I} & \mathbf{0} \\ -\mathbf{I} & \mathbf{0} & \mathbf{C} \\ \mathbf{0} & \mathbf{C}^T & \mathbf{0} \end{bmatrix} \tag{4.37}$$

while the element vector (contributing to the right-hand side of the assembled equations) is:

$$\begin{bmatrix} \mathbf{0} & \mathbf{0} & \mathbf{P}^e \end{bmatrix}^T \tag{4.38}$$

where the first column of the stiffness matrix corresponds to the incremental displacements of node (k), the second column to the (external) forces of node (k) and the third column to the incremental displacements of node (e). It is notable that the forces of node (k) cannot be specified a priori. In addition, the degrees of freedom of node (k) must not be supported, since they are directly connected to the degrees of freedom of the plate node (e).

4.4 Two-Dimensional Analysis

In addition to the analysis described above, a procedure for two-dimensional analysis based on the cross section has been developed. In this case, ovalization and curvature are assumed to be constant along the pipe. Instead of formulating a special two-dimensional element, the same 9-node shell element is employed using appropriate boundary conditions. Six elements along the half-circumference and one element in the longitudinal direction x_3 are used. Note that the condition of constant ovalization along the pipe implies that the deformed shell generators will have a circular shape. However, the elements have parabolic shape functions and this imposes a restriction to their length l in the x_3 direction. Assuming that a parabola is an adequate representation of a circular arc of angle not greater than $\pi/8$ and denoting by k_u the maximum curvature encountered in the analysis, one finds:

$$l \leq \frac{\pi}{8} \frac{1}{k_u} \tag{4.39}$$

In the present computations, l was taken equal to $D/4$, i.e., equal to the length of each element in three-dimensional analysis. Symmetry conditions with respect to the $x_3 = l/2$ and $x_2 = 0$ axes are imposed. Two rigid plates are assumed to be connected to the end sections, so that, end section nodes (k) and the corresponding vectors $\boldsymbol{q}_3^{(k)}$ are always on the plate. However, these nodes can move on the plate. The motion of each one of the plates is monitored by a plate node (e). There are three orthonormal vectors $\boldsymbol{e}_1$, $\boldsymbol{e}_2$, $\boldsymbol{e}_3$ associated with this node, initially in the directions of the global Cartesian coordinate system. During deformation, $\boldsymbol{e}_3$ is always normal to the plate.

The assumption of constant curvature along tube generators implies that the cross sections remain plane. Furthermore, the in-plane deformation (ovalization) is the same for all cross sections. Towards enforcing the first condition, the nodes at $x_3 = l/2$ are supported so as to maintain a plane cross section without, however, restricting the in-plane deformation ("roller" supports). Also, the end sections ($x_3 = 0$ and $x_3 = l$) are forced to remain plane by attaching, not "welding", rigid plates that allow in-plane deformations. Using the notation adopted earlier for end plates, the degrees of freedom of shell node (k) are transformed to plate-specific components (see Figure 4.5):

$$\begin{array}{lcll} \Delta\hat{u}_i^{(k)} & = & \boldsymbol{e}_i{\cdot}[\Delta u_1^{(k)}\boldsymbol{x}_1 + \Delta u_2^{(k)}\boldsymbol{x}_2 + \Delta u_3^{(k)}\boldsymbol{x}_3] & (i = 1,2,3) \\ \Delta\hat{\theta}_j^{(k)} & = & \boldsymbol{t}_j^{(k)}{\cdot}[\Delta\theta_1^{(k)}\hat{\boldsymbol{q}}_1^{(k)} + \Delta\theta_2^{(k)}\hat{\boldsymbol{q}}_2^{(k)}] & (j = 1,2) \end{array} \tag{4.40}$$

where

$$\begin{array}{lcl} \boldsymbol{t}_1^{(k)} & = & \boldsymbol{e}_3 \\ \boldsymbol{t}_2^{(k)} & = & \hat{\boldsymbol{q}}_3^{(k)} \times \boldsymbol{e}_3 \end{array}$$

In terms of these components, the provisions for node (k) to move on the plate can be written as:

$$\begin{array}{lcl} \Delta\hat{u}_3^{(k)} & = & \boldsymbol{e}_3{\cdot}[\Delta u_1^{(e)}\boldsymbol{x}_1 + \Delta u_3^{(e)}\boldsymbol{x}_3] + (\boldsymbol{e}_2 \times [\boldsymbol{x}^{(k)} - \boldsymbol{x}^{(e)}]){\cdot}\boldsymbol{e}_3\,\Delta\theta_2^{(e)} \\ \Delta\hat{\theta}_2^{(k)} & = & \boldsymbol{e}_2{\cdot}\boldsymbol{t}_2^{(k)}\Delta\theta_2^{(e)} \end{array} \tag{4.41}$$

Finally, the in-plane beformation of the end sections is made identical to that of the middle section. For this purpose, a reference generator is chosen. Let (r) ans (r') be the nodes on this generator at one of the end sections and the middle section respectively. Also, let (k) and (k') be corresponding nodes on another generator. The conditions that the ovalization of the cross sections be the same are:

$$\begin{array}{lcl} \Delta\hat{u}_1^{(k)} - \Delta\hat{u}_1^{(r)} & = & \Delta u_1^{(k')} - \Delta u_1^{(r')} \\ \Delta\hat{u}_2^{(k)} & = & \Delta u_2^{(k')} \\ \Delta\hat{\theta}_1^{(k)} & = & \Delta\theta_2^{(k')} \end{array} \tag{4.42}$$

Note that, for nodes at the middle section, $\boldsymbol{q}_2 = \boldsymbol{x}_3$ throughout the deformation history.

The implementation of these constraints is desribed below. Eqs. 4.40 can be written in matrix form as follows:

$$\boldsymbol{\Delta}\mathbf{U}^{(k)} = \mathbf{A}\,\boldsymbol{\Delta}\mathbf{V}^{(k)} \tag{4.43}$$

The nonzero components of matrix $\mathbf{A}$ (5×5) are

$$\begin{aligned} &A_{ij} = e_{ij}\,, \quad i,j = 1,2,3 \\ &A_{44} = \ A_{55} = \boldsymbol{e}_3 \cdot \hat{\boldsymbol{q}}_1 \\ &A_{45} = -A_{54} = \boldsymbol{e}_3 \cdot \hat{\boldsymbol{q}}_2 \end{aligned} \tag{4.44}$$

where e_{ij} is component i of vector $\boldsymbol{e}_j$. Eqs. 4.41 can be written as

$$\boldsymbol{\Delta}\mathbf{V}^{(k)} = \mathbf{B}\,\boldsymbol{\Delta}\hat{\mathbf{V}}^{(k)} + \hat{\mathbf{B}}\,\boldsymbol{\Delta}\mathbf{U}^{(e)} \tag{4.45}$$

where the nonzero components of $\mathbf{B}$ (5×3) and $\hat{\mathbf{B}}$ (5×3) are

$$\begin{aligned} &B_{11} = B_{22} = B_{43} = 1 \\ &\hat{B}_{31} = e_{13} \\ &\hat{B}_{32} = e_{33} \\ &\hat{B}_{33} = -\boldsymbol{e}_1 \cdot [\boldsymbol{x}^{(k)} - \boldsymbol{x}^{(e)}] \\ &\hat{B}_{53} = -\boldsymbol{e}_1 \cdot \hat{\boldsymbol{q}}_3 \end{aligned} \tag{4.46}$$

and

$$\boldsymbol{\Delta}\hat{\mathbf{V}}^{(k)} = \left[\ \Delta\hat{u}_1^{(k)} \quad \Delta\hat{u}_2^{(k)} \quad \Delta\hat{\theta}_1^{(k)}\ \right]^T \tag{4.47}$$

On the other hand Eq. 4.42 can be cast in the form

$$\begin{aligned} \boldsymbol{\Delta}\hat{\mathbf{V}}^{(k)} = \ &\mathbf{D}\,\boldsymbol{\Delta}\hat{\mathbf{V}}^{(r)} + \hat{\mathbf{D}}\,\boldsymbol{\Delta}\mathbf{U}^{(k')} \\ &+ \mathbf{E}\,\boldsymbol{\Delta}\mathbf{U}^{(r')} + \hat{\mathbf{E}}\,\boldsymbol{\Delta}\mathbf{U}^{(e)} \end{aligned} \tag{4.48}$$

The nonzero components of matrices $\mathbf{D}$ (3×3), $\hat{\mathbf{D}}$ (3×5), $\mathbf{E}$ (3×5) and $\hat{\mathbf{E}}$ (3×3) are the following:

$$\begin{aligned} D_{11} &= E_{11} = -1 \\ \hat{D}_{11} &= \hat{D}_{22} = \hat{D}_{35} = 1 \\ \hat{E}_{11} &= e_{11} \\ \hat{E}_{22} &= e_{31} \end{aligned} \tag{4.49}$$

Combining Eqs. 4.43, 4.45 and 4.48, one finds:

$$\begin{aligned} \boldsymbol{\Delta U}^{(k)} = \; & \mathbf{C_1}\, \boldsymbol{\Delta} \hat{\mathbf{V}}^{(r)} + \mathbf{C_2}\, \boldsymbol{\Delta U}^{(k')} \\ & + \mathbf{C_3}\, \boldsymbol{\Delta U}^{(r')} + \mathbf{C_4}\, \boldsymbol{\Delta U}^{(e)} \end{aligned} \tag{4.50}$$

where

$$\begin{aligned} \mathbf{C_1}(5 \times 3) &= \mathbf{A\,B\,C} \\ \mathbf{C_2}(5 \times 5) &= \mathbf{A\,B}\hat{\mathbf{D}} \\ \mathbf{C_3}(5 \times 5) &= \mathbf{A\,B\,E} \\ \mathbf{C_4}(5 \times 3) &= \mathbf{A\,B}\hat{\mathbf{E}} + \mathbf{A}\hat{\mathbf{B}} \end{aligned}$$

Therefore, the auxiliary element matrix can be composed as:

$$\begin{bmatrix} \mathbf{0} & -\mathbf{I} & \mathbf{0} & \mathbf{0} & \mathbf{0} & \mathbf{0} \\ -\mathbf{I} & \mathbf{0} & \mathbf{C_1} & \mathbf{C_2} & \mathbf{C_3} & \mathbf{C_4} \\ \mathbf{0} & \mathbf{C_1}^T & \mathbf{0} & \mathbf{0} & \mathbf{0} & \mathbf{0} \\ \mathbf{0} & \mathbf{C_2}^T & \mathbf{0} & \mathbf{0} & \mathbf{0} & \mathbf{0} \\ \mathbf{0} & \mathbf{C_3}^T & \mathbf{0} & \mathbf{0} & \mathbf{0} & \mathbf{0} \\ \mathbf{0} & \mathbf{C_4}^T & \mathbf{0} & \mathbf{0} & \mathbf{0} & \mathbf{0} \end{bmatrix} \tag{4.51}$$

In the above matrix, the first column cooresponds to the incremental displacements $\mathbf{\Delta U}^{(k)}$ of node (k), the second column to the nodal forces $\mathbf{P}^{(k)}$, the third to the incremental in-plate dislpacements $\mathbf{\Delta \hat{V}}^{(r)}$ of the reference node (r), the fourth to the incremental displacements $\mathbf{\Delta U}^{(k')}$ of the conjugate node (k'), the fifth to the incremental dislpacements $\mathbf{\Delta U}^{(r')}$ of node (r') and the sixth to the incremental plate displacements $\mathbf{\Delta U}^{(e)}$. The associated right-hand side contribution is

$$\begin{bmatrix} \mathbf{0} & \mathbf{0} & \mathbf{0} & \mathbf{0} & \mathbf{0} & \mathbf{P}^e \end{bmatrix}^T \tag{4.52}$$

There is one such auxiliary element for each shell node (k) on the rigid plate, except for the reference node (r). For this particular node only conditions 4.40 and 4.41 apply. This means that the auxiliary element for this node has a matrix given by

$$\begin{bmatrix} \mathbf{0} & -\mathbf{I} & \mathbf{0} & \mathbf{0} \\ -\mathbf{I} & \mathbf{0} & \mathbf{C}'_1 & \mathbf{C}'_2 \\ \mathbf{0} & \mathbf{C}'^T_1 & \mathbf{0} & \mathbf{0} \\ \mathbf{0} & \mathbf{C}'^T_2 & \mathbf{0} & \mathbf{0} \end{bmatrix} \tag{4.53}$$

and vector:

$$\begin{bmatrix} \mathbf{0} & \mathbf{0} & \mathbf{0} & \mathbf{P}^e \end{bmatrix}^T \tag{4.54}$$

where matrices $\mathbf{C}'_1$ and $\mathbf{C}'_2$ are defined as follows:

$$\mathbf{C}'_1(5 \times 3) = \mathbf{A}\,\mathbf{B}$$
$$\mathbf{C}'_2(5 \times 3) = \mathbf{A}\,\hat{\mathbf{B}}$$

Note that the first column of the element matrix corresponds to the incremental nodal displacements $\mathbf{\Delta U}^{(r)}$, the second column to the nodal forces $\mathbf{P}^{(r)}$, the

third to the incremental in-plate displacements $\Delta\hat{\mathbf{V}}^{(r)}$ and the fourth to the incremental plate displacements $\Delta\mathbf{U}^{(e)}$.

Chapter 5

Response Under Bending and Pressure

In the present chapter, the response of relatively thick tubes to external pressure and bending is examined. First, a physical explanation of the instability of tubes due to extensive ovalization is presented. Then, the general features of pipeline response under combined loading are described. Finally, results from three-dimensional and two-dimensional analyses are reported and compared with the existing simplified formulas.

5.1 Physical Explanation of Ovalization Instability

Consider a pipe under bending (Figure 5.1). The top fibers have tensile stresses σ_t, while the bottom fibers have compressive stresses σ_c. Due to the longitudinal curvature, both stresses σ_t and σ_c, if projected on the axis $a - a$, give a component which is directed towards the interior of the pipe. These stress components are responsible for the ovalization process.

An immediate consequence of the ovalization process is the decrease of the lever-arm between the total compressive and total tensile force of the cross-section. This means that ovalization tends to decrease the moment. At low values of bending, the rate of increase of moment due to strain-hardening of the material is greater than the rate of decrease due to ovalization. At the point where the two rates become equal, a limit moment point occurs. This is

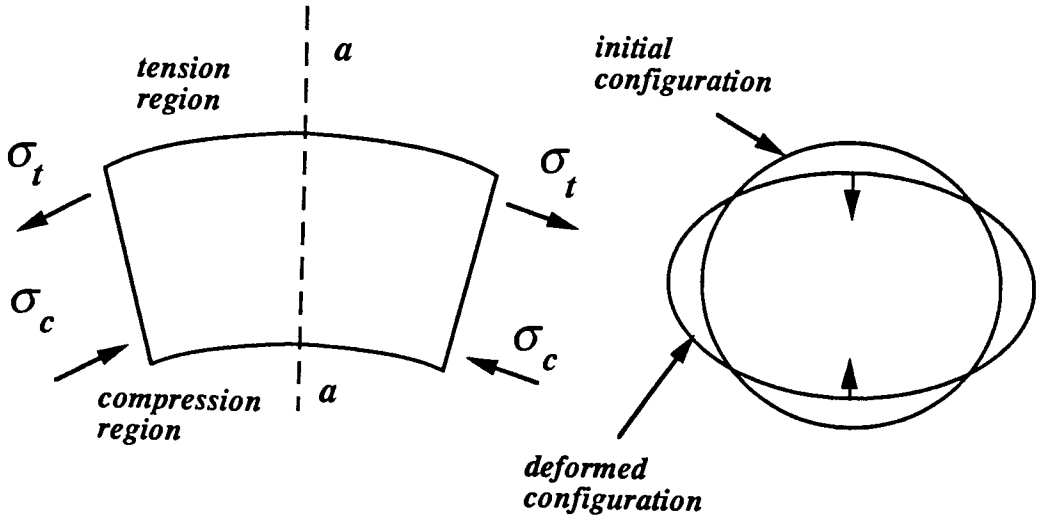

Figure 5.1: Schematic representation of ovalization phenomenon.

accentuated by the fact that the increase of longitudinal stresses is restrained by the appearence of hoop stresses in the plasticity equations. Of course, the pipe must be sufficiently thick in order to resist the high longitudinal compressive stresses. For the case of thin pipes, these stresses cause buckling in the form of wrinkles on the compressive side of the tube, before the ovalization limit point occurs.

A characteristic value of D/t ratio equal to 40 is used in order to distinguish between the two types of instability. It is noted that this value is empirical and comes from experimental observations, not from a detailed analysis of the phenomenon.

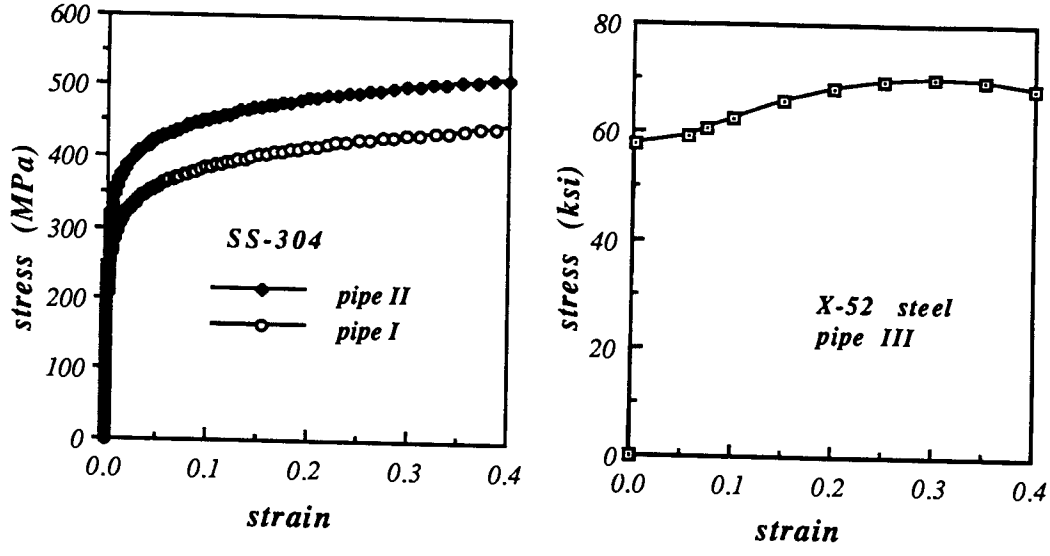

Figure 5.2: Uniaxial stress-strain curves.

5.2 Description of Pipes Analysed

Three pipes are considered in this work. Pipes I and II were tested experimentally and analyzed using a different technique by Corona and Kyriakides [8]. They are both relatively thick pipes with D/t equal to 34.7 and 18.2 respectively. Since D/t is less than 40, it is expected that collapse will be caused by extensive ovalization. Therefore, the possibility of bifurcation buckling is not considered. The material is stainless steel and its nominal stress-strain relationship is approximated by a Ramberg-Osgood curve:

$$\epsilon = \frac{\sigma}{E}\left[1 + \frac{3}{7}(\frac{\sigma}{\sigma_y})^{n-1}\right] \tag{5.1}$$

as suggested by Corona and Kyriakides [8]. The values of the material constants are E = 186 and 204 GPa, σ_y = 224 and 283 MPa and n =9.67 and

10.7 for pipes I and II respectively. There is a slight difference between the axial and circumferential yield stresses. This difference is ignored in the present analysis. The uniaxial curves for these materials are depicted in Figure 5.2(a).

Pipe III is a candidate for deep-water applications. Its dimensions are $D = 12.75\,in$ $(323.85\ mm)$, $t = 0.59\,in$ $(14.986\ mm)$. The material is $X-52$ steel with a nominal strees-strain curve (provided by Langner [26]) as shown in Figure 5.2(b).

Pipe III is considered to be initially perfect. Pipes I and II are also assumed to be perfect, expect for the case of pure pressure loading where a very slight initial ovalization is considered. This initial imperfection is defined as a perturbation of the radial coordinate, i.e., if a nodal point in the perfect ring has polar coordinates (R,θ), in the imperfect ring its polar coordinates will be $(R+w,\theta)$, where:

$$w = w_o \cos 2\theta \tag{5.2}$$

The ratio w_o/R was taken equal to $6 \cdot 10^{-4}$ for pipes I and II.

5.3 General Features of Pipeline Response

Results are presented in the form of pressure-curvature and pressure-moment interaction diagrams. The reported curvature is calculated by dividing the relative end-rotation (θ) by the initial length of pipe generators (i.e., L in $3D$ analysis, or l in $2D$ analysis). Pressure, curvature and moment are normalized by $p_y = 2\sigma_y t/D$, $k_I = t/D^2$ and $M_y = \sigma_y t D^2$ respectively.

Three loading paths are considered : $k \rightarrow p$, $p \rightarrow k$, and radial path (Figure 5.3). Their main characteristics are the following:

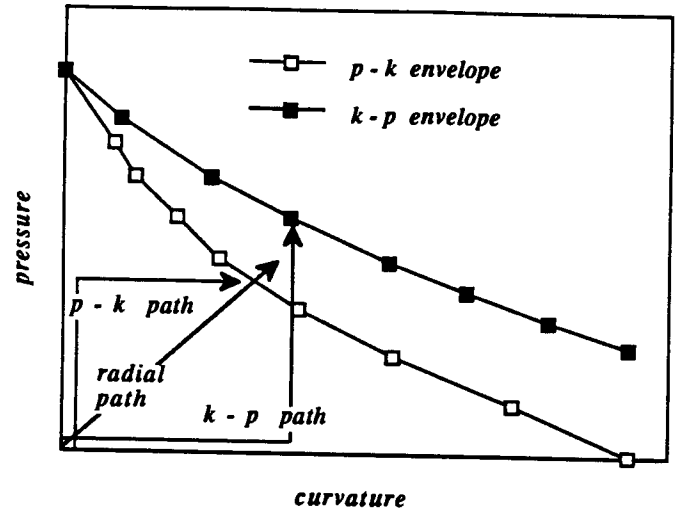

Figure 5.3: Definition of three loading sequences.

$k \rightarrow p$ *path* : Pure bending is first imposed on the pipe up to a certain curvature by increasing end rotation. Then, keeping the end rotation constant, pressure is applied by means of negative volume-like changes (pressure node), until a limit pressure is reached. The locus of these points defines the collapse envelope for this path. It is notable that, during pressure application, the moment is substantially reduced.

$p \rightarrow k$ *path* : The pipe is subjected to pure pressure up to a certain level which is then kept constant while curvature is increased. The point where moment reaches a limit value is the collapse point and the locus of these points constitutes the collapse envelope for this path. The pressure level has a significant effect on the limit moment and the corresponding curvature, as well as on the smoothness of the moment-curvature curve around the limit point.

At high pressure levels, the pipe exhibits "brittle" behavior: the moment-curvature curve is almost linear prior to the limit point, whereas around the limit point the curve becomes very sharp and collapse is sudden.

Radial path : In this path, both loading parameters (pressure and curvature) are increased simultaneously and proportionally. For a narrow range of loading cases with very low curvature values, a point of limit pressure is encoutered first. This is explained by the fact that, for very low curvatures, the behavior is similar to that under pure pressure. On the other hand, for the majority of radial loading cases, a point of limit moment is reached first, at a level which can be much below the $p \rightarrow k$ envelope. This phenomenon was also reported by Corona and Kyriakides [7]. However, it is expected, from a physical point of view, that instability for the radial path occurs somewhere between the envelopes for the two previous paths. The interaction between the two loading parameters must be considered. This is achieved by adopting a stability criterion based on the second-order work

$$W = \Delta p \, \Delta V + \Delta M \Delta \theta \tag{5.3}$$

where Δp , ΔV , ΔM and $\Delta \theta$ denote the increments of pressure, volume enclosed by the pipe segment, moment and relative end rotation (these are the increments computed during a step of the analysis). While W is positive, the pipe is stable. Loss of stability occurs when W changes sign. Note that this criterion can be applied to any loading path. In the cases of $k \rightarrow p$ and $p \rightarrow k$ paths, it is consistent with the collapse definitions given previously. In the $k \rightarrow p$ case, $\Delta \theta$ is zero and ΔV is positive. Therefore, when p changes sign, Δp becomes negative and W changes sign. Similarly, along the $p \rightarrow k$

path, Δp is zero and $\Delta\theta$ is positive. Thus, when limit moment occurs (i.e., ΔM becomes negative) W changes sign.

5.4 Results from Three-Dimensional Analysis

For pipe I envelopes for $k \rightarrow p$ and $p \rightarrow k$ loading sequences are shown in Figure 5.4(a). Their comparison with the experimental data shows reasonably good agreement. Several collapse points were obtained for pipe II, that are also close to the experimental data [Figure 5.4(b)]. Only the pure bending case was analyzed for pipe III (see Figure 5.11).

The actual curvature along the pipe was calculated in seven cases and results are presented in Figures 5.5, 5.6 and 5.7. It is seen that the curvature is not constant along the deformed pipe and this is due to the boundary conditions imposed by the end plates which are "welded" on the pipe and, therefore, do not allow ovalization near the ends. In all cases, maximum curvature (k_{max}) occurs in the middle section and is greater than the curvature calculated from relative end rotations (k_{3D}). Apparently, the rigid plates are responsible for some fluctuations of the curvature near the end-sections. In general, the change of curvature along the pipe is more pronounced at high levels of relative end rotation. In the special case of pure bending, the difference between (k_{max}) and (k_{3D}) is quite significant (22.5 %, 16.7 % and 8.5 % for pipes I, II and III respectively). Note that for lower values of curvature this difference is not as noticeable. However, the above observations show that curvature calculated from experimental data may be an ambiguous measure of curvature, whenever rigid plates are used [11]. In the small-scale experiments

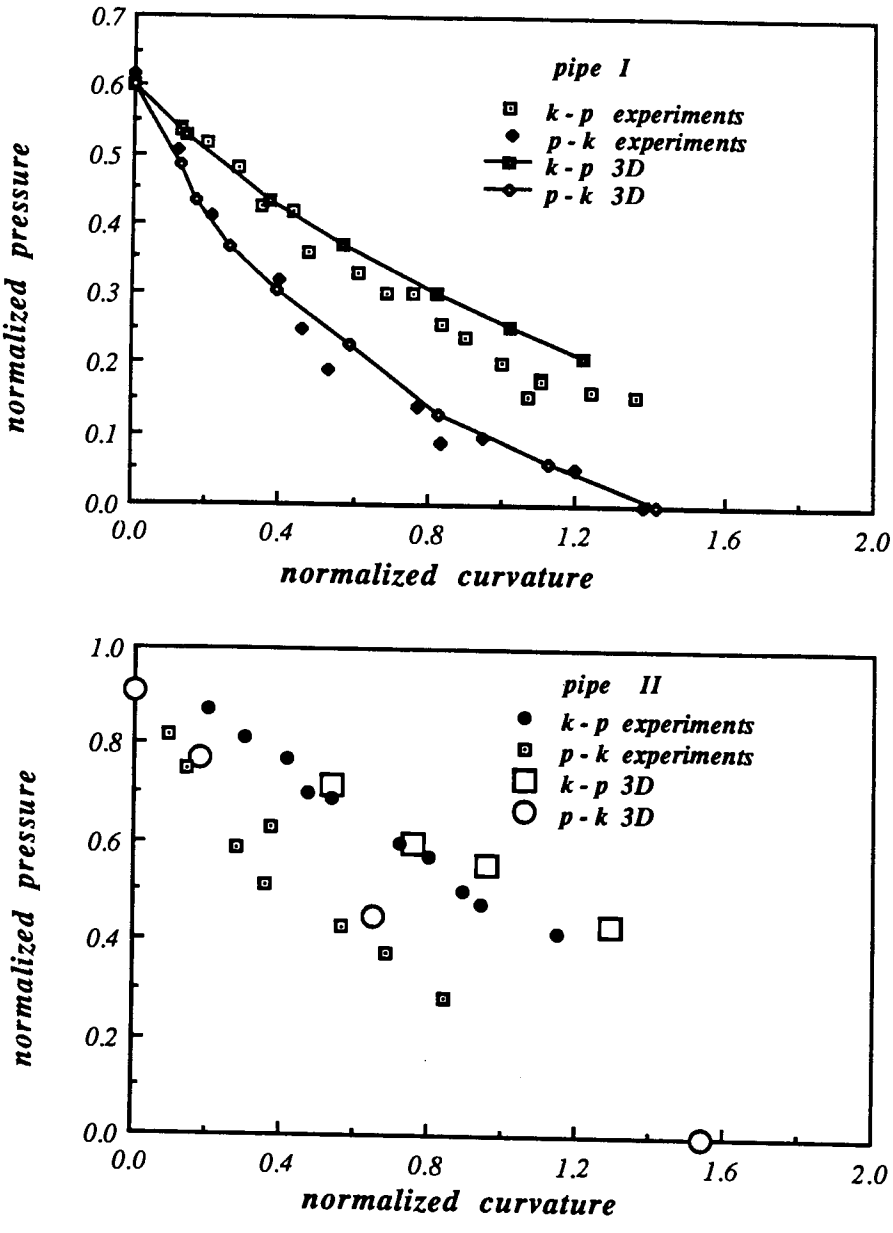

Figure 5.4: Comparison between $3D$ analysis and experimental data [8] for pipes I and II.

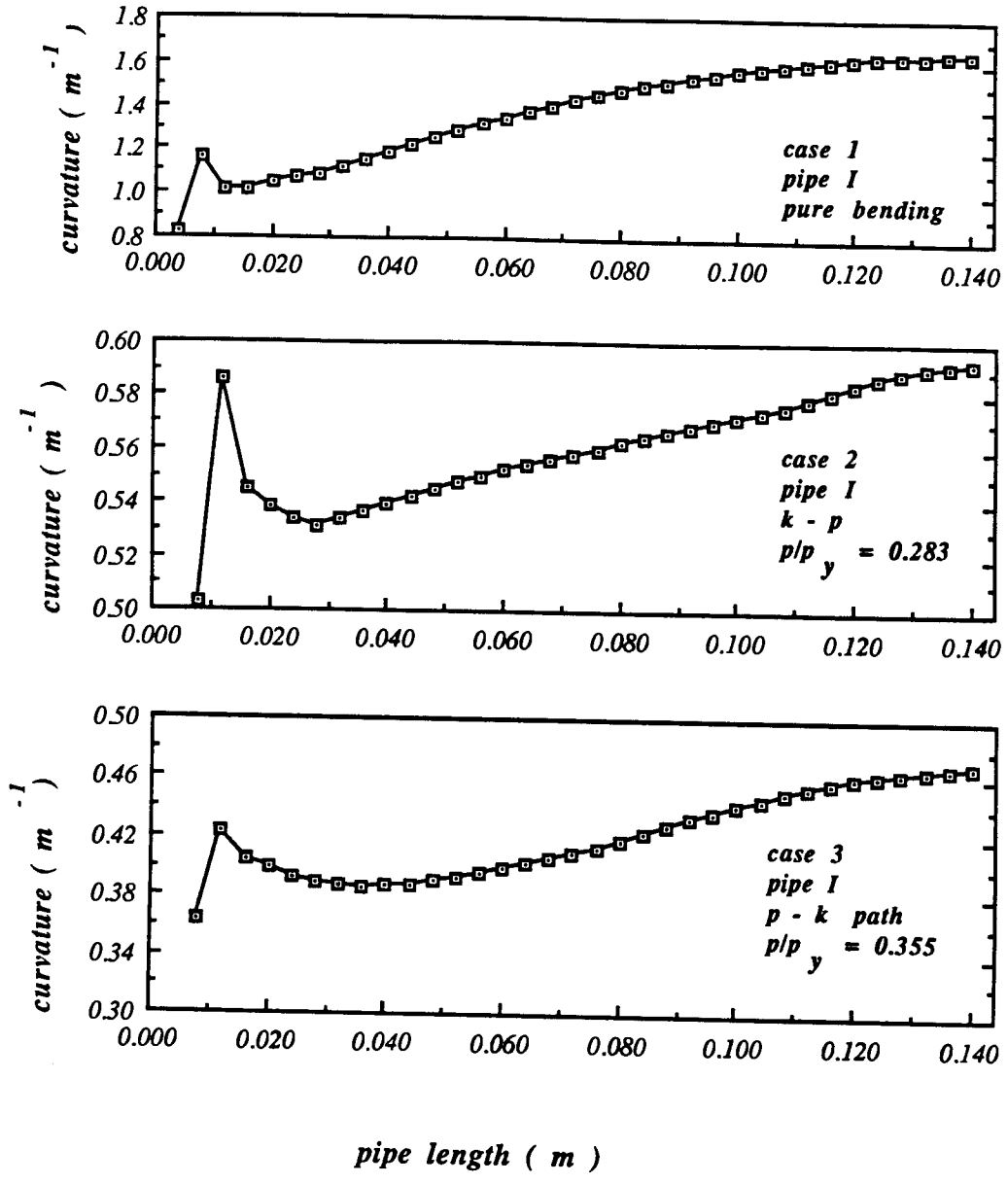

Figure 5.5: Variation of curvature along pipe I for three loading cases at collapse.

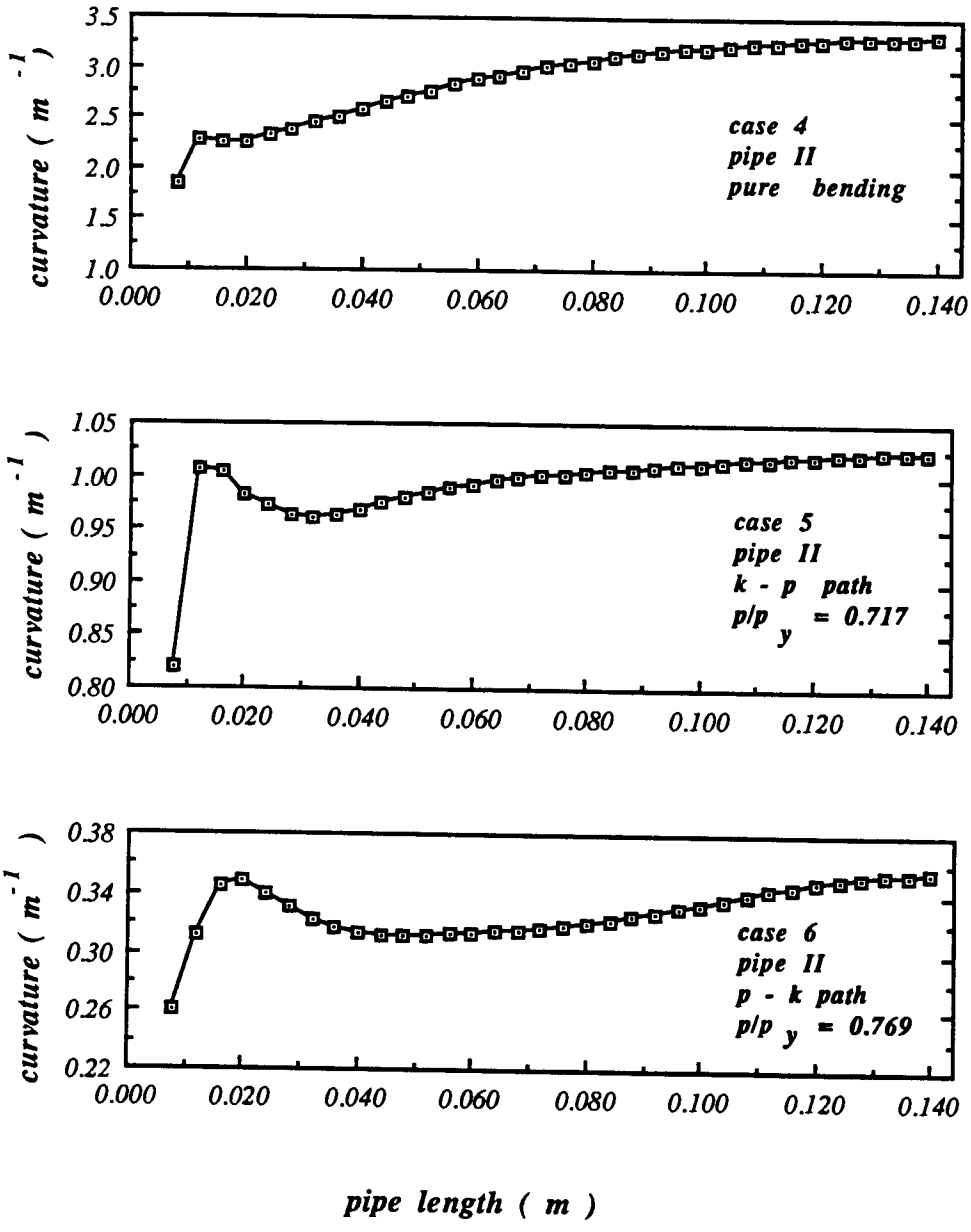

Figure 5.6: Variation of curvature along pipe II for three loading cases at collapse.

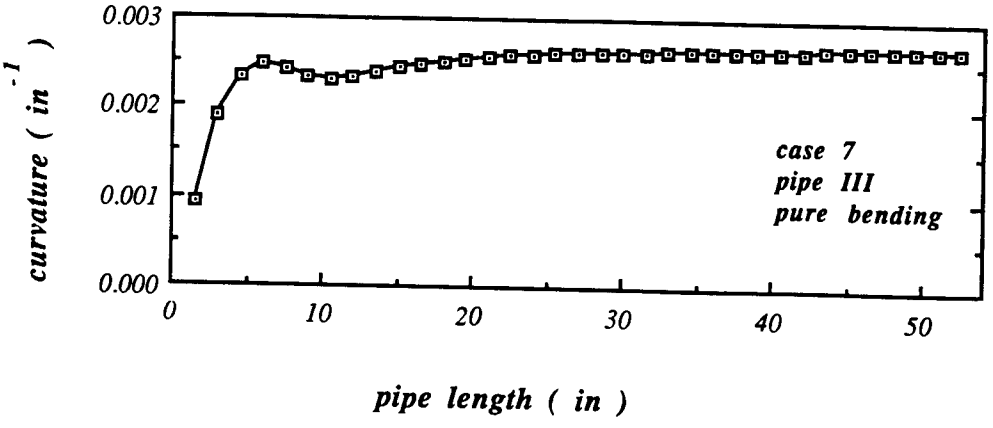

Figure 5.7: Variation of curvature along pipe III for the pure bending case.

of Corona and Kyriakides [7],[8], a more elaborate mechanism was used to impose relative end-rotations. It is believed that the curvature is more nearly constant along the pipes tested in those experiments.

For pipe I, three moment-curvature curves are shown in Figure 5.8 for different values of pressure. For the case of pure bending, the behavior is characterized by a very large "plastic plateau" where curvature increases under almost constant moment. For $p/p_y = 0.20$, the limit moment is not significantly affected, but the ultimate curvature value is reduced to half the value recorded in pure bending, and the curve around the limit point becomes sharper. For $p/p_y = 0.44$, the ultimate moment is half the limit moment under pure bending, whereas ultimate curvature is almost eight times smaller. In this case, pipe behavior becomes "brittle" with sudden collapse. In Figure 5.9 moment-curvature curves for the pure-bending, three-dimensional analysis of pipes II and III are also depicted. Note that the curves for pipes I and II show considerable strain-hardening, in contrast with the curve for pipe III which

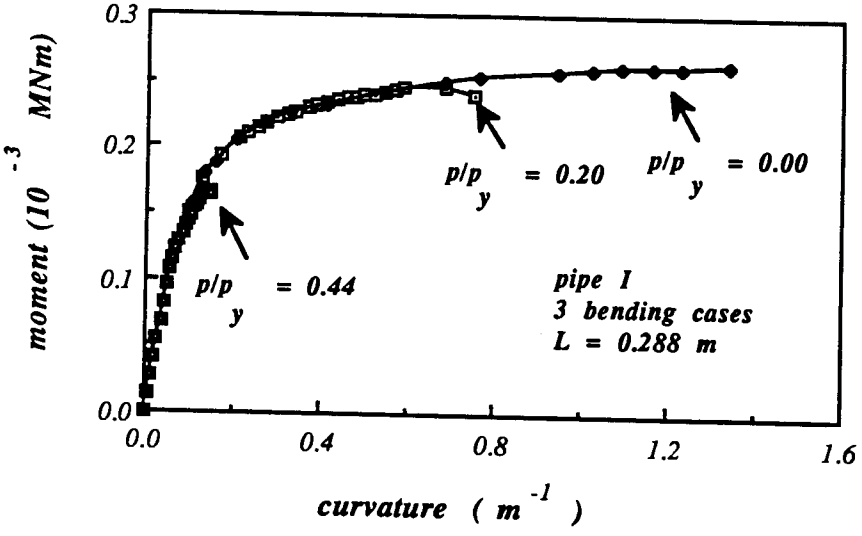

Figure 5.8: Moment-curvature curves for three different pressure levels for pipe I [3D analysis].

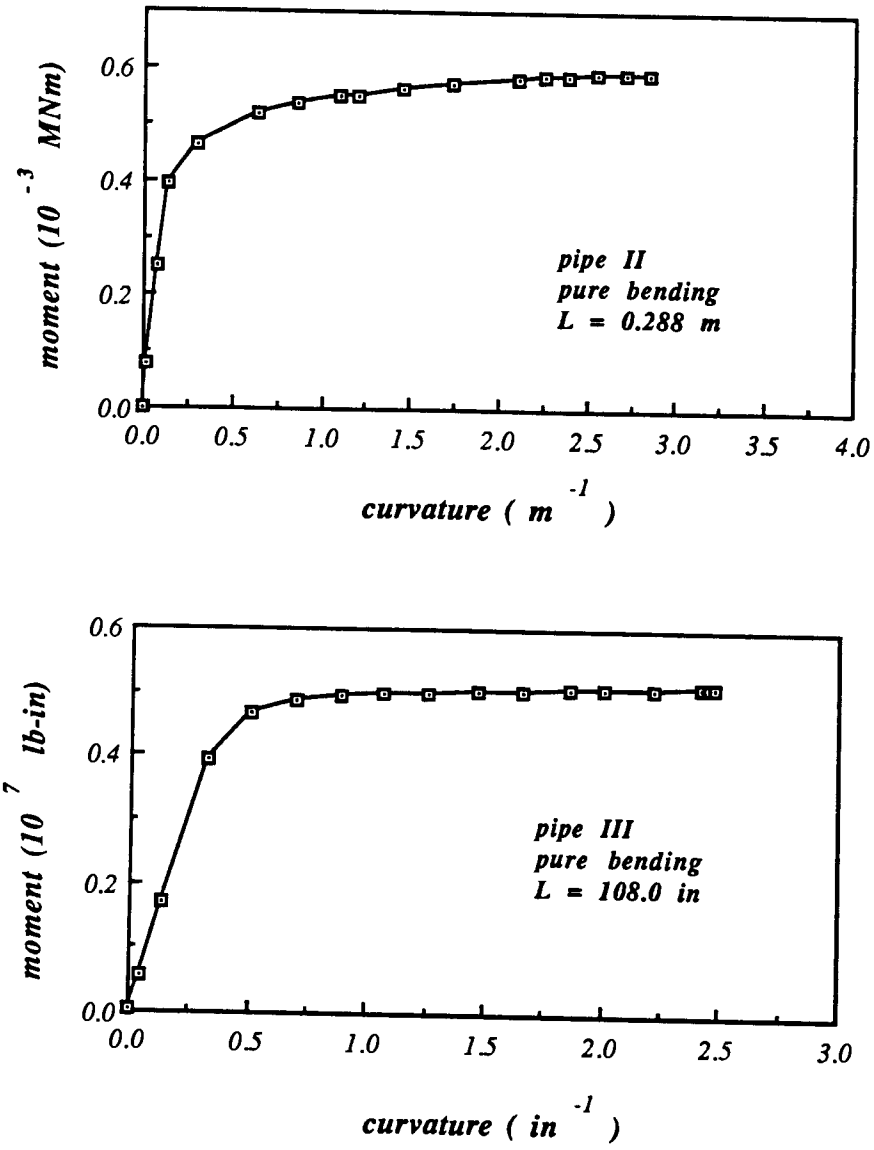

Figure 5.9: Moment-curvature curves for pure bending of pipe II and pipe III [$(3D)$ analysis].

becomes quite flat after yielding. This is explained by the notably different shapes of stress-strain curves for stainless steel and $X-52$ steel.

cases	k_{3D}	k_{max}	k_{ave}	k_{2D}
1	*1.339*	*1.640*	*1.521*	*1.511*
2	*0.546*	*0.593*	*0.575*	*0.547*
3	*0.410*	*0.467*	*0.436*	*0.421*
4	*2.826*	*3.300*	*3.150*	*3.146*
5	*0.979*	*1.020*	*1.010*	*1.024*
6	*0.322*	*0.355*	*0.323*	*0.324*
7	*0.00247*	*0.00268*	*0.00264*	*0.00267*

Table 5.1: Comparison between characteristic values of curvature from three-dimensional analysis and curvature from two-dimensional analysis.

5.5 Results from two-dimensional analysis

Collapse envelopes for the three pipes are presented in Figures 5.10 and 5.11. In addition, results for pipes I and II are compared with experimental data in Figure 5.12. There is generally good agreement. However, for cases with high curvatures (i.e., close to the pure-bending case), two-dimensional envelopes seem to overestimate pipe strength when compared with three-dimensional analysis. This is depicted for pipe I in Figure 5.13 and for pipe III in Figure 5.11 and it is a consistent result since curvature reported in three-dimensional analysis is calculated from end rotations and underestimates the actual curvature. In Table 5.1, the ultimate curvature from two-dimensional analysis (k_{2D}) is compared with curvature calculated from end rotations (k_{3D}), maximum curvature (k_{max}) and the average curvature of a five-diameter pipe length about the middle section (k_{ave}) from three-dimensional analysis (the cases are the same as those of Figures 5.5, 5.6 and 5.7). The comparison indicates that (k_{2D}) is closest to (k_{ave}).

Of particular importance is the case of radial loading. For most of the cases, limit moment occurs at a very low level of loading even below the $p \rightarrow k$ envelope. This is shown in Figure 5.14 for the radial case of pipe III. The limit moment does not identify pipe collapse, since the second-order work W is still positive due to the increase of pressure. Collapse (i.e., change of sign in W) occurs at a point between the $p \rightarrow k$ and $k \rightarrow p$ envelopes. For very few cases corresponding to very low curvatures, limit pressure occurs first just before collapse. This is quite reasonable since for these cases the behavior tends to be the same as the behavior under pure pressure.

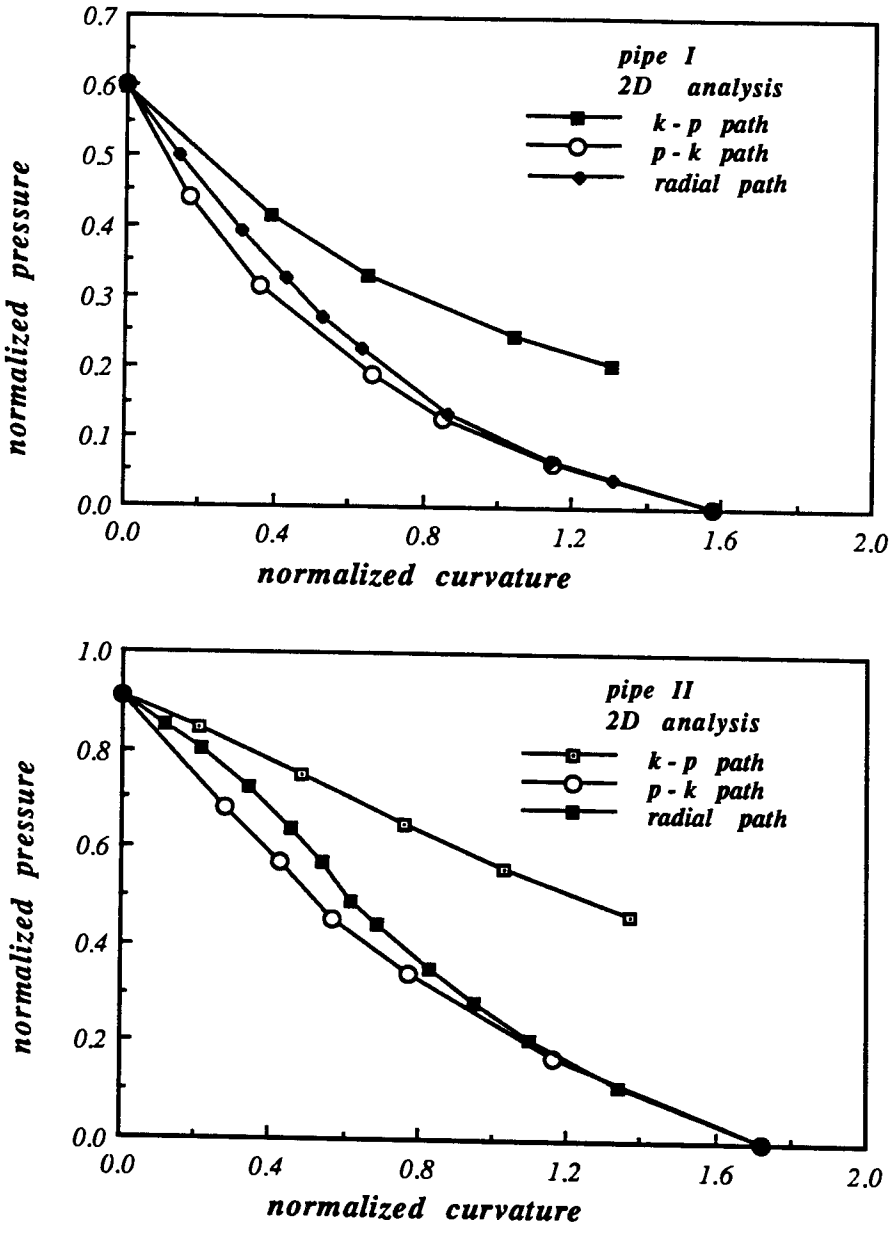

Figure 5.10: Collapse envelopes for pipes I and II from $2D$ analysis.

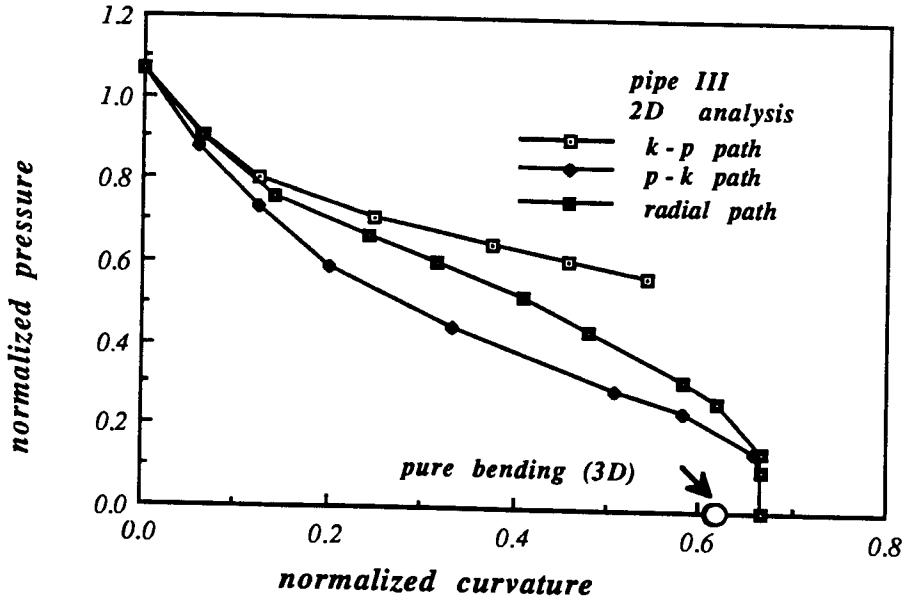

Figure 5.11: Collapse envelopes for pipe III from $2D$ analysis.

For the sake of completeness, the pressure-moment interaction curves for $p \rightarrow k$ path are depicted in Figures 5.15 and 5.16 for the three pipes. It is interesting to note the "convex" shape of these graphs, as opposed to the "concave" shape of the pressure-curvature diagrams. Indeed, for low values of pressure, the limit moment is nearly constant, whereas the corresponding curvature is significantly affected by the value of the pressure. This is in accordance with the behavior shown in Figure 5.8. On the other hand, for large values of pressure, the moment-curvature curve is almost linear elastic with sudden collapse. This implies that the curvature varies within a small range of values, whereas the change in limit moment is quite significant.

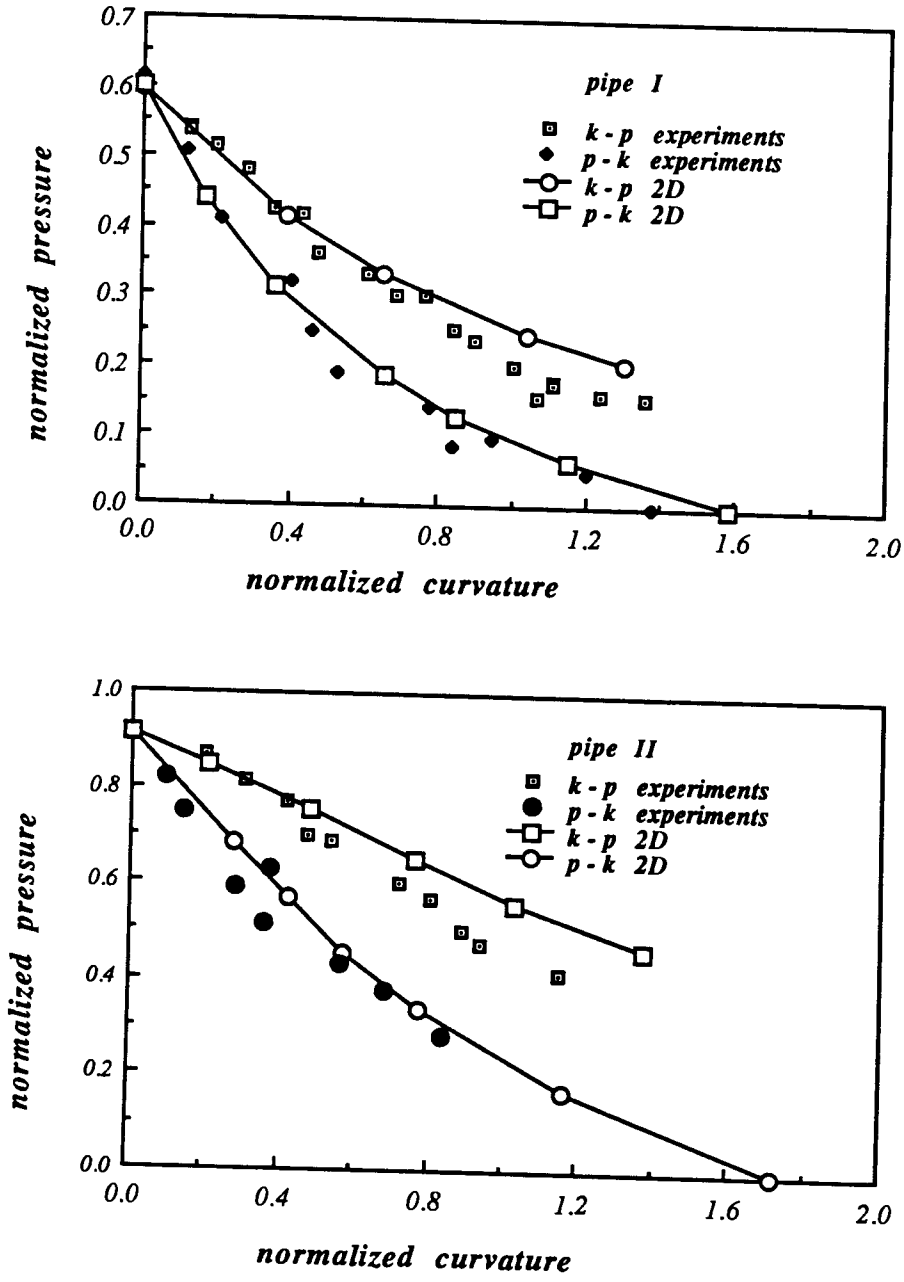

Figure 5.12: Comparison between results from $2D$ analysis of pipes I and II and experimental data [8].

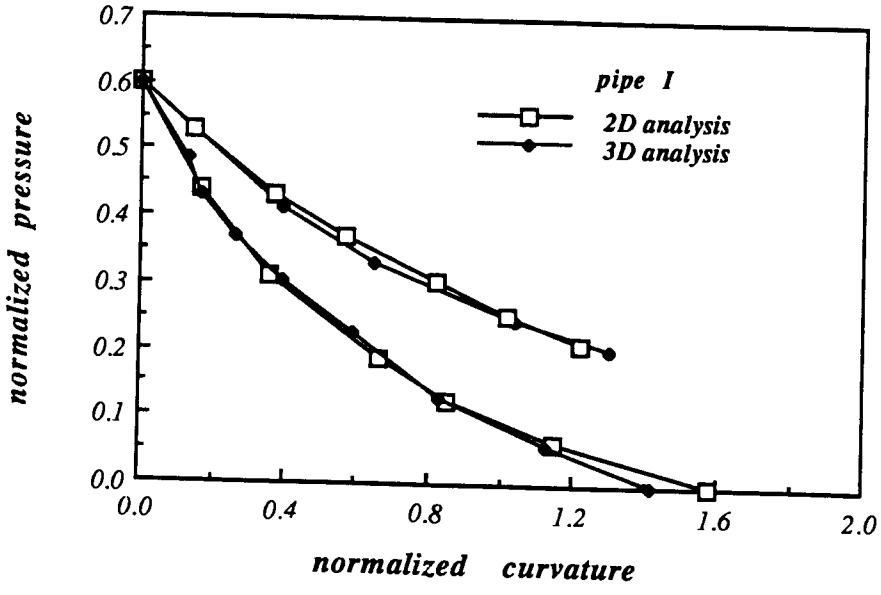

Figure 5.13: Comparison between results from $3D$ and $2D$ analyses of pipe I.

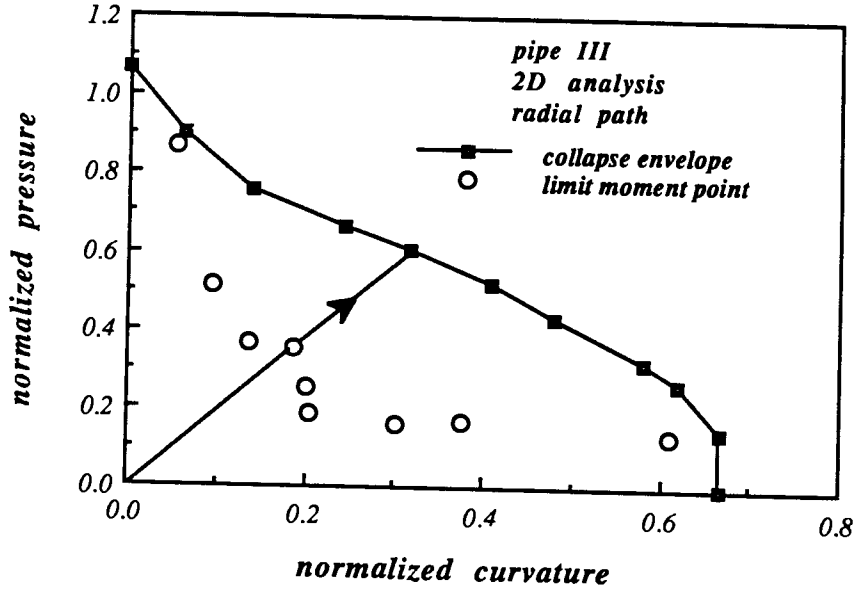

Figure 5.14: Radial path envelope and limit moment points for pipe III.

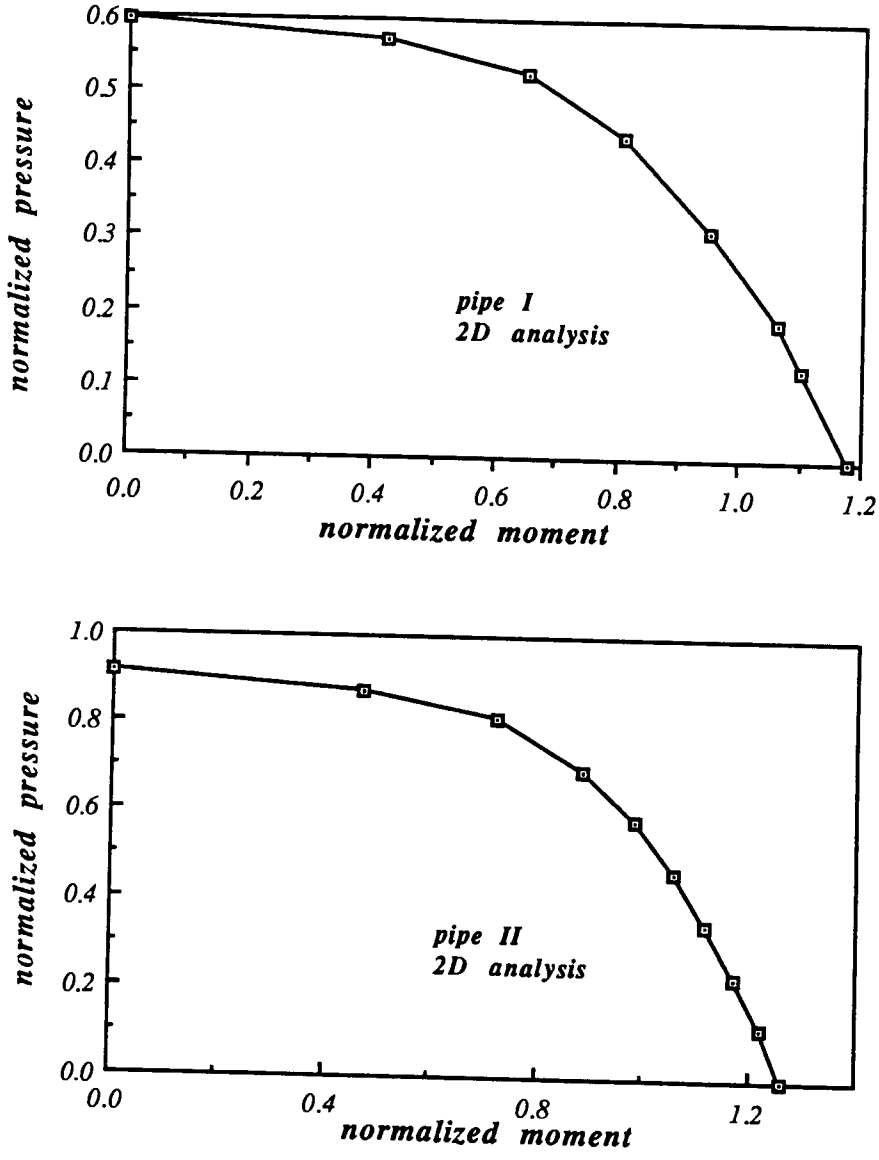

Figure 5.15: Pressure-moment envelopes of pipes I and II for $p \rightarrow k$ path.

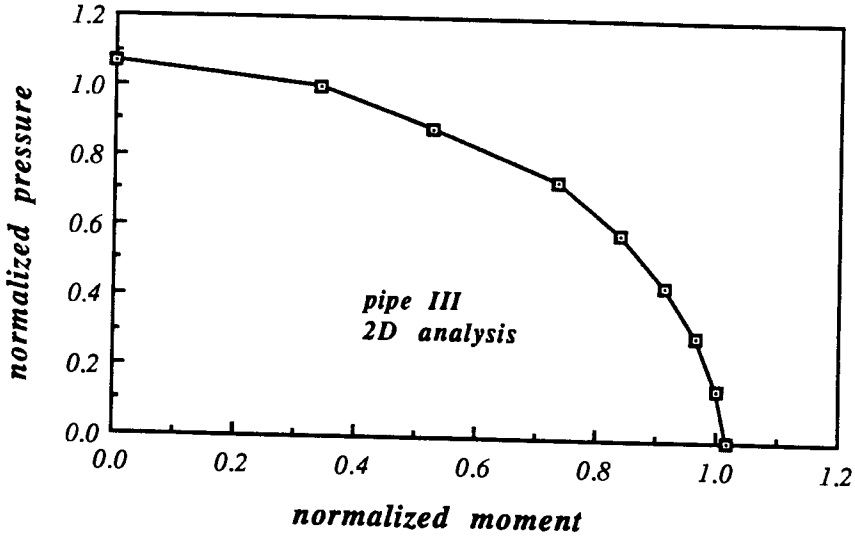

Figure 5.16: Pressure-moment envelopes of pipe III for $p \rightarrow k$ path.

5.6 Comparison with Existing Formulas

As mentioned in Chapter 2, there exist several formulas which can be used for pipeline design. It is interesting to compare these formulas with the envelopes derived above, in order to examine their accuracy. Three formulas are considered herein. The first two are the Shell (Eq. 2.6) and Battelle (Eq. 2.11) formulas, which are widely used in design. Of these, the Shell formula is entirely based on experimental data, whereas the Battelle formula is semi-empirical. The third formula is 2.13, derived by de Winter et al.[46] by considering a simplified model of tube collapse.

A first conceptual comparison between Shell and Battelle formulas is necessary at this point. The maximum pressure capacity given by the Shell formula is based on experimental data. On the other hand, the ultimate pres-

sure for the Battelle formula is found from the Timoshenko equation. More specifically, this formula is derived by assuming an initial inextensional ovalization in the form of the first buckling mode and linearizing the governing equations. The pressure that produces a maximum stress equal to the yield stress is considered to be the maximum pressure. Furthermore, the maximum bending capacity is generally different in the two formulas. They coincide only if $D/t = 32$. Finally, the shape of the two curves is different. The Shell formula assumes a linear interaction, whereas the Battelle formula accounts for the concave nature of the available experimental data.

The formulas are compared with the $p \rightarrow k$ envelope which is the most crucial and most likely to occur during the pipelaying procedure. Figure 5.17 shows the comparison for pipes I and II. It appears that, in general, all formulas are in fairly good agreement with the $p \rightarrow k$ envelope. Furthermore, both Shell and Battelle formulas predict with very good accuracy the pure pressure strength. However, for the pure bending case, they both significantly underestimate the ultimate capacity. The equation of de Winter et al. is quite satisfactory, except for the regions near the pure bending and pure pressure cases, where it overestimates the ultimate strength. In Figure 5.18 the comparison for pipe III is depicted. The pure-pressure point is very accurately predicted from the Battelle formula and the equation of de Winter et al., whereas the Shell formula is rather conservative. For the pure bending case, all formulas overestimate the ultimate capacity. Note that the Shell formula provides the best prediction for this case.

From the above comparison, it is apparent that the Shell formula correlates better the $p \rightarrow k$ envelope for pipes having a D/t ratio of about 20.

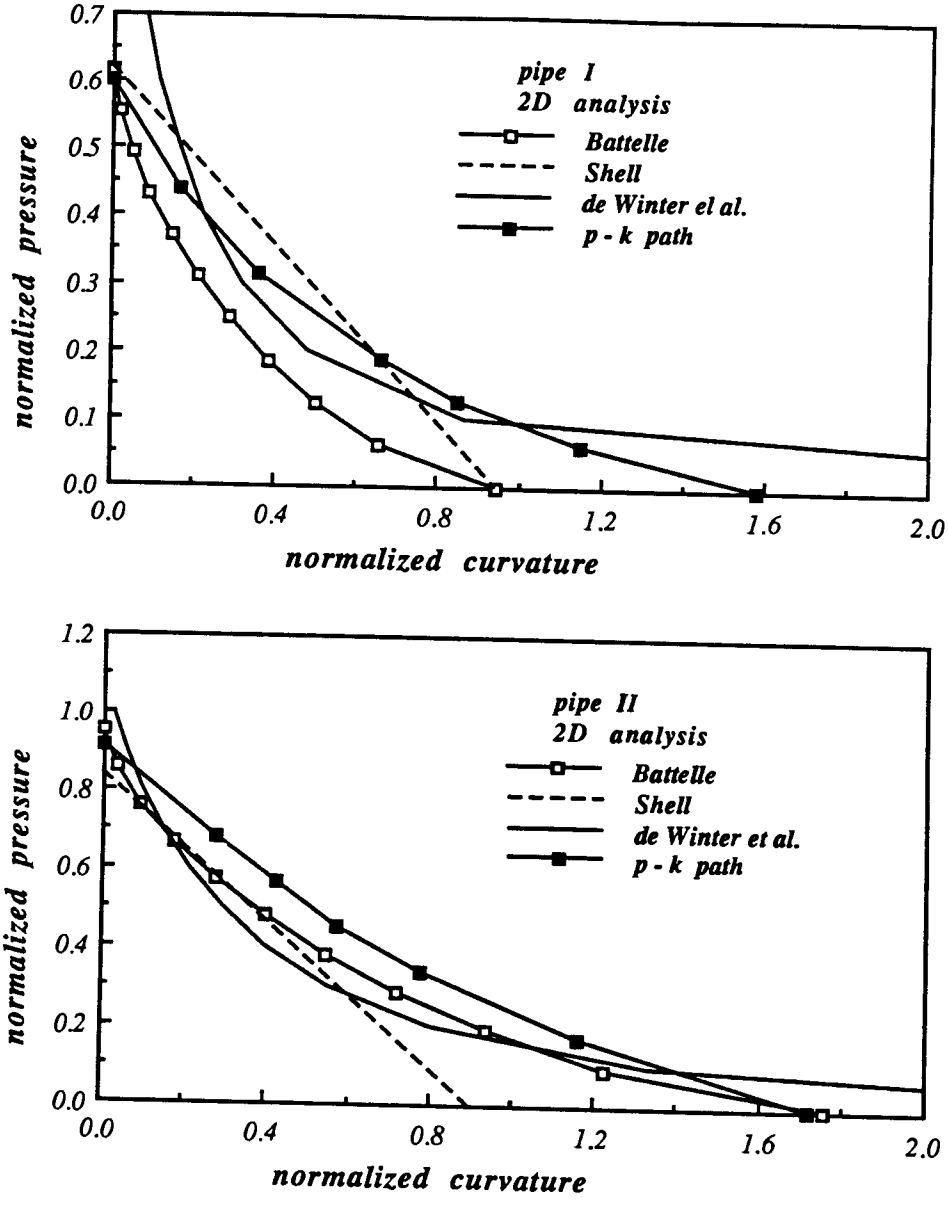

Figure 5.17: Comparison between $p \rightarrow k$ envelope and design formulas for pipes I and II.

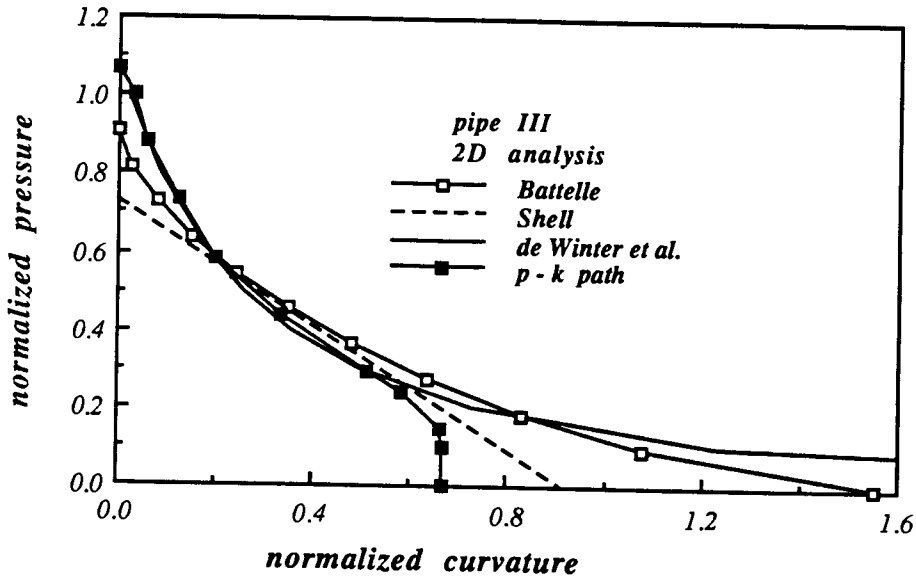

Figure 5.18: Comparison between $p \rightarrow k$ envelope and design formulas for pipe III.

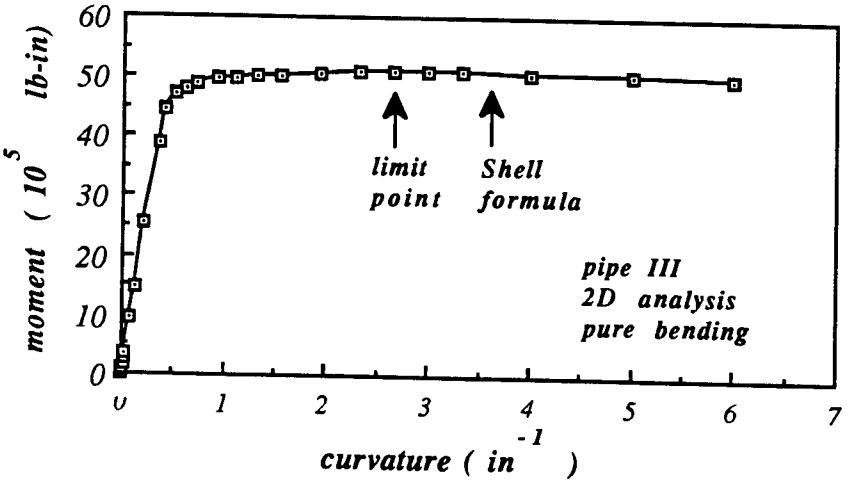

Figure 5.19: Pure bending curve for pipe III.

This is in accordance with the conclusion of Fowler [11] who compared the formulas with experimental data. However, this formula is not accurate for the pure bending case, especially for pipe III. This can be explained from the large plastic plateau of the moment-curvature diagram. Figure 5.19 shows the moment-curvature diagram for pipe III under pure bending. Indeed, it can be seen that the curvature predicted from the Shell formula corresponds to a moment value which is practically the same with the limit moment, their difference being less that 0.5%. In addition, the formula is rather conservative for the pure pressure case. However, it should be noted that the elastoplastic buckling of tubes under pure bending is very sensitive to initial imperfections [19]. In our analysis in order to obtain the pure-pressure point, we assumed an initial imperfection (ovalization) of the order of $6 \cdot 10^{-4}$ for pipes I and II, and no imperfection for pipe III. Note that in [25] the allowable initial imperfection is specified to be 0.01. Therefore, the Shell formula seems to provide a good estimate of the collapse envelope for design purposes.

Chapter 6

Effect of Tension on Pipeline Response

In the course of installation, the pipe, in addition to pressure and bending, is subjected to a tensile axial force, which is necessary in order to control the pipeline shape. Without this force, the pipe would fail due to extensive bending in the sagbend region. In the presence of tension, the interaction curves derived in Chapter 5 must be revised. First, the effect of tension on the response under pressure is examined. Then, the case where all loading parameters (bending, pressure and tension) are nonzero is considered.

6.1 Pressure and Tension

The same three pipes considered in the case of bending-pressure loading are examined in this analysis as well. In addition, a fourth pipe (referred to as pipe IV) is analyzed to compare the present analysis with the exprerimental data of Kyriakides et al. [21]. The pipe diameter and thickness are $31.75\,mm$ and $1.2446\,mm$ respectively and the pipe material is stainless steel. The uniaxial material behavior is given by the Ramberg-Osgood formula (see Eq. 5.1) , where E and σ_o are taken equal to $199\,GPa$ and $320 MPa$ respectively. Finally, the yield stress is $368\,MPa$.

In order to examine the path-sensitivity of this loading combination, two different loading loading paths are analyzed:

- $p \rightarrow T$ path, where pressure is raised to a certain value, and then it is kept constant, while tensile deformation is applied until a limit tension load is reached.
- $T \rightarrow p$ path, in which tension is first applied up to a certain level, and then it is kept constant, while pressure is increased until a limit pressure is obtained.

Results are presented in the form of pressure-tension interaction curves. The values of tension and pressure are normalized by $T_y = \sigma_y A$ and $p_y = 2\sigma_y t/D$ respectively, where A is the area of the undeformed cross-section. Figures 6.1 and 6.2 show the collapse envelopes for pipes I, II and III respectively. It is apparent that the results from this loading combination are almost independent of the loading sequence. This observation was also reported by Kyriakides et al. [21], and it is explained by the fact that, during most part of loading, the pipe remains elastic and collapse occurs soon after yielding. The path-independence is more pronounced in the case of pipe III, which has a very slight amount of strain hardening and collapse occurs almost immediately after initial yield. On the other hand, pipes I and II have significant strain hardening and exhibit plastic response before collapse. Therefore, a certain path dependence is expected. The difference between the two paths is more pronounced for pipe II which is thicker than pipe I.

It is important to note that, the pipe must have a slight initial imperfection (see Eq. 5.2) for a limit value of pressure to occur. More specifically, the value of w_o/R was taken equal to $7 \cdot 10^{-4}$ for pipes I,II and III, and equal to $1 \cdot 10^{-3}$ for pipe IV.

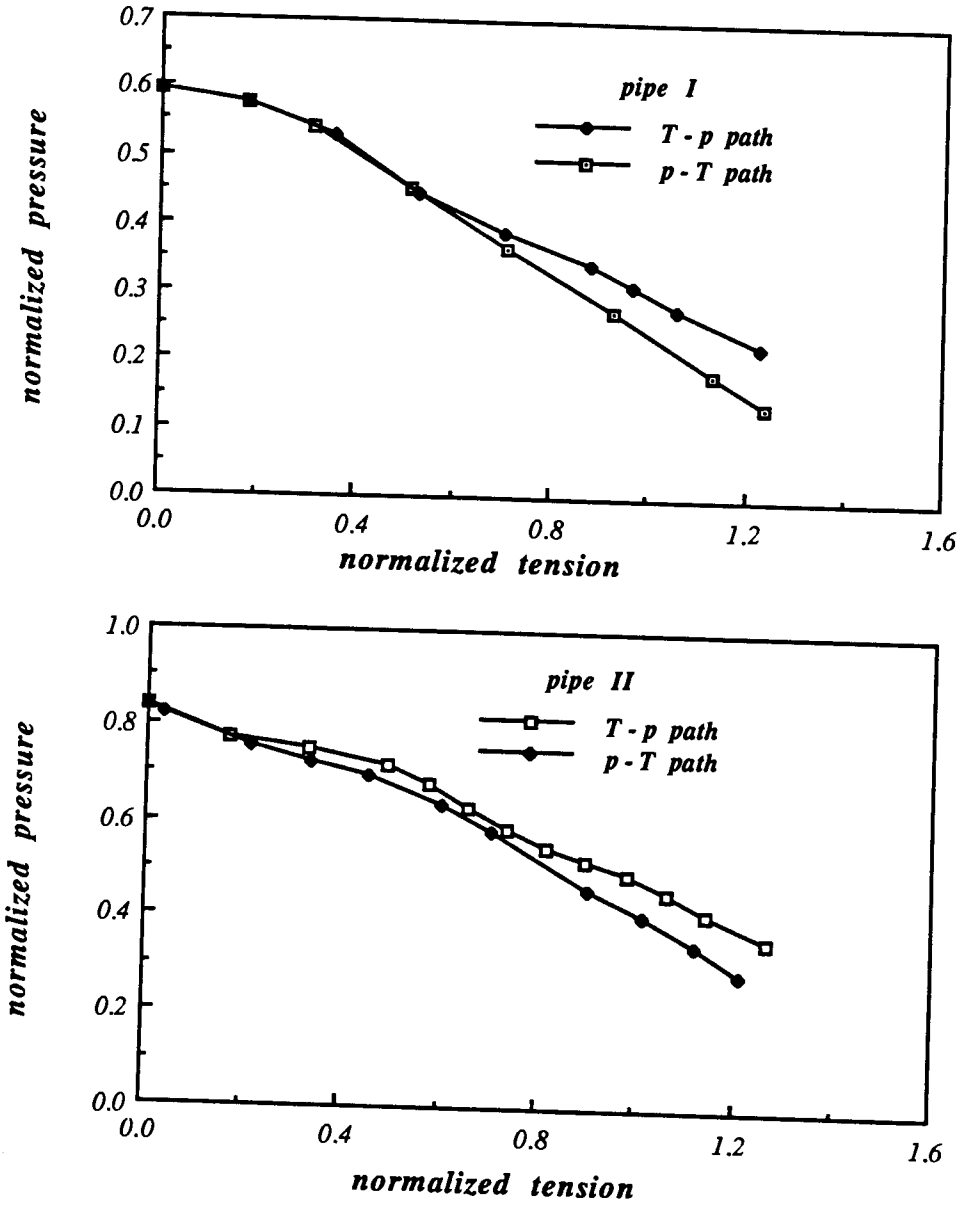

Figure 6.1: Pressure-tension envelopes for pipes I and II.

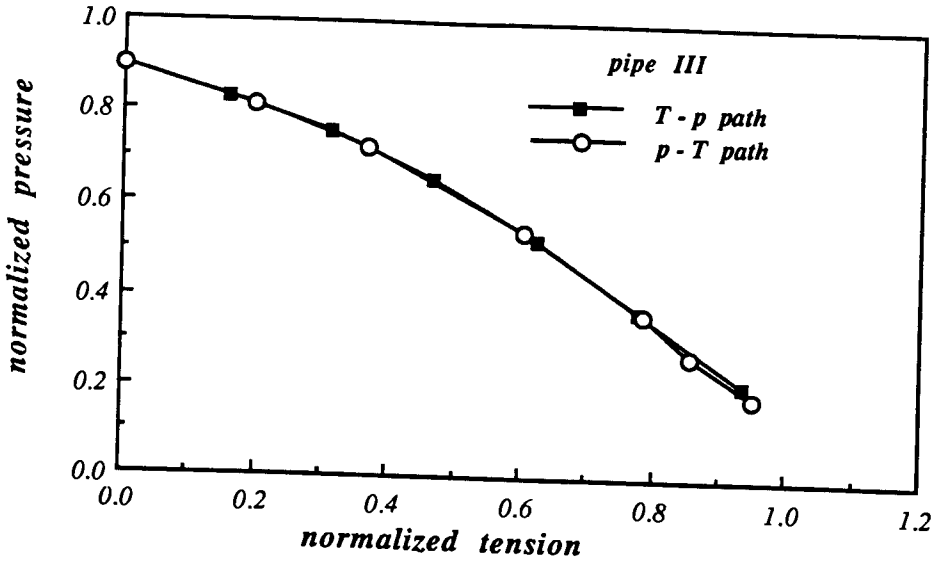

Figure 6.2: Pressure-tension envelopes for pipe III.

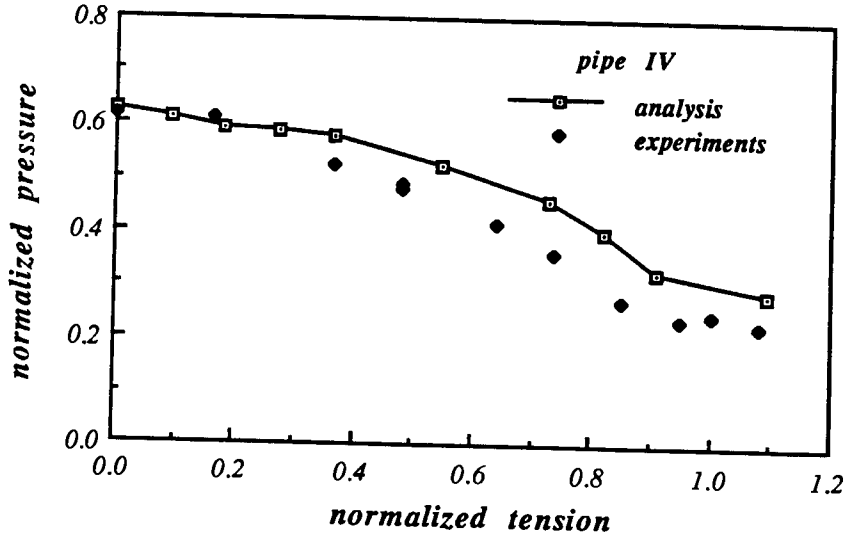

Figure 6.3: Pressure-tension envelope for pipe IV ($T \rightarrow p$ path).

Figure 6.3 shows the comparison between the present analysis and the experimental data for pipe IV. Results are in good agreement especially at high pressure levels.

In Figures 6.4 and 6.5, the $p \rightarrow T$ collapse envelope is compared with the envelopes from three existing formulas. The first is the Shell formula for pressure-tension interaction (combination of Eqs. 2.4 and 2.9). The second formula is proposed in the API bulletin (see Eq. 2.10) and the third was derived by de Winter et al. (Eq. 2.12) by considering a simplified "rocker" element to model pipe collapse. The comparison indicates that the Shell formula is quite accurate. On the other hand, the API formula and Eq. 2.12 are on the conservative and the unconservative side respectively. However, it should be noted that all three formulas neglect the post yielding material behavior, and assume that yield tension is the ultimate tension loading. This is rather conservative for materials having significant hardening (e.g. materials of pipes I and II), but is very reasonable for materials which are nearly elastic-perfectly-plastic as the material of pipe III.

6.2 Bending, Pressure and Tension

In this case, all three loading parameters are considered. In fact, there is a large number of loading sequences. However, only the $T \rightarrow p \rightarrow k$ path will be examined herein. This path is the most likely to occur during the pipelaying process.

From the numerical point of view, the auxiliary elements described in Chapter 4 must be adjusted in order to control the axial force in the direction

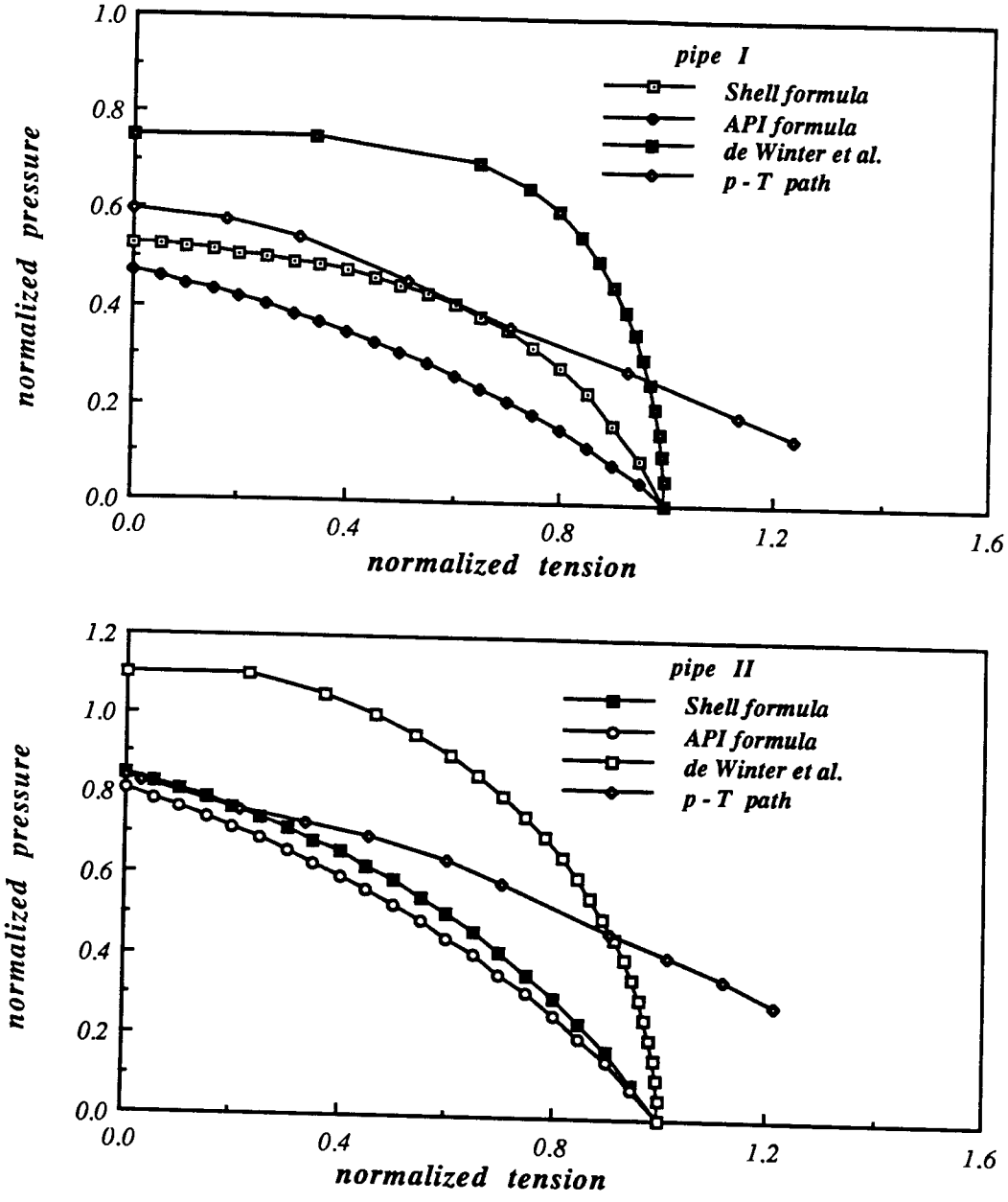

Figure 6.4: Comparison between $p \rightarrow T$ envelope and design formulas for pipes I and II.

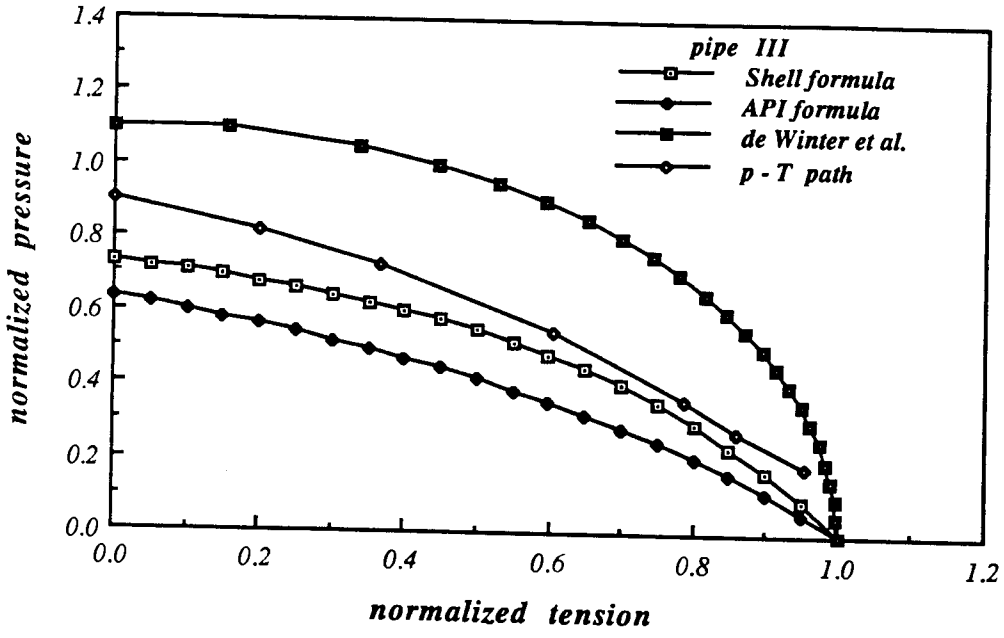

Figure 6.5: Comparison between $p \rightarrow T$ envelope and design formulas for pipe III.

normal to the cross section of the pipe (Figure 6.6). Thus, the degrees of freedom of the plate node must be transformed by rotation to the $\hat{x}_1$ and $\hat{x}_3$ directions. This can be easily achieved by multiplying matrices $\mathbf{C_4}$ and $\mathbf{C_2'}$ by the matrix $\mathbf{R}$ (3×3) given by:

$$\mathbf{R} = \begin{bmatrix} cos\phi & sin\phi & 0 \\ -sin\phi & cos\phi & 0 \\ 0 & 0 & 1 \end{bmatrix} \tag{6.1}$$

where ϕ is the total rotation of the plate. In fact ϕ is equal to $\theta/2$, θ being the relative rotation of the two plates. Plate nodes are restrained in the $\hat{x}_1$-direction, whereas in the $\hat{x}_3$-direction the force is prescribed.

It should be noted that, in order to satisfy equilibrium, it is necessary to apply load on the pipe in the transverse direction. For that, the bottom

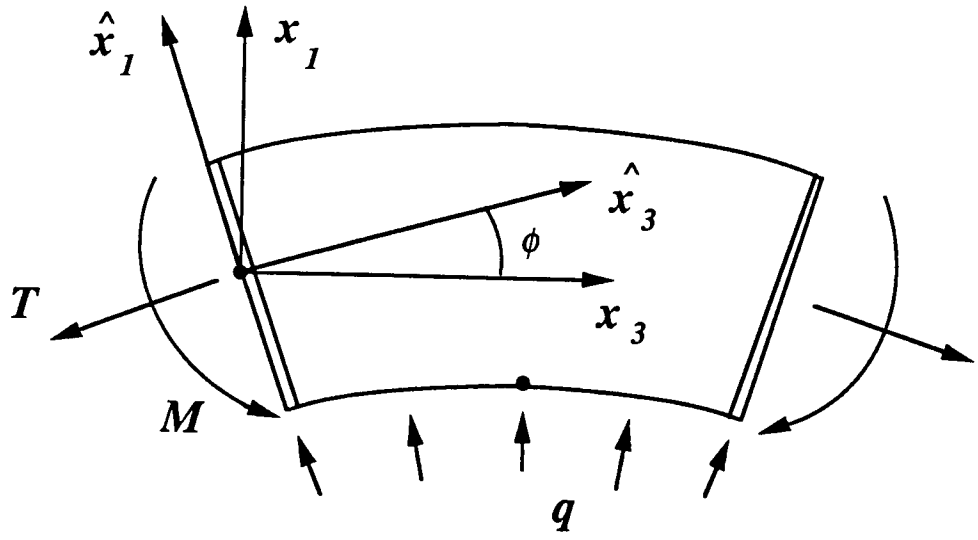

Figure 6.6: Schematic representation of bending-tension procedure.

node of the middle section is fixed. The kinematic conditions 4.42 of uniform cross-section ovalization will produce forces on the bottom nodes of the end sections. Due to the uniform curvature along the generators, the support conditions will simulate a uniformly distributed constant load on the inner pipe generator (Figure 6.6).

In all reported results, moment is computed with respect to the middle point of the cross-section, and normalized by $M_y = \sigma_y t D^2$, which is the yield moment of the cross-section.

The pressure-bending diagrams of pipes I and II are shown in Figures 6.7 and 6.8 for four levels of axial force. The most important observation is that the bending capacity is reduced when tension is increased. It should be emphasized that the interaction curves derived in Chapter 5 are different from

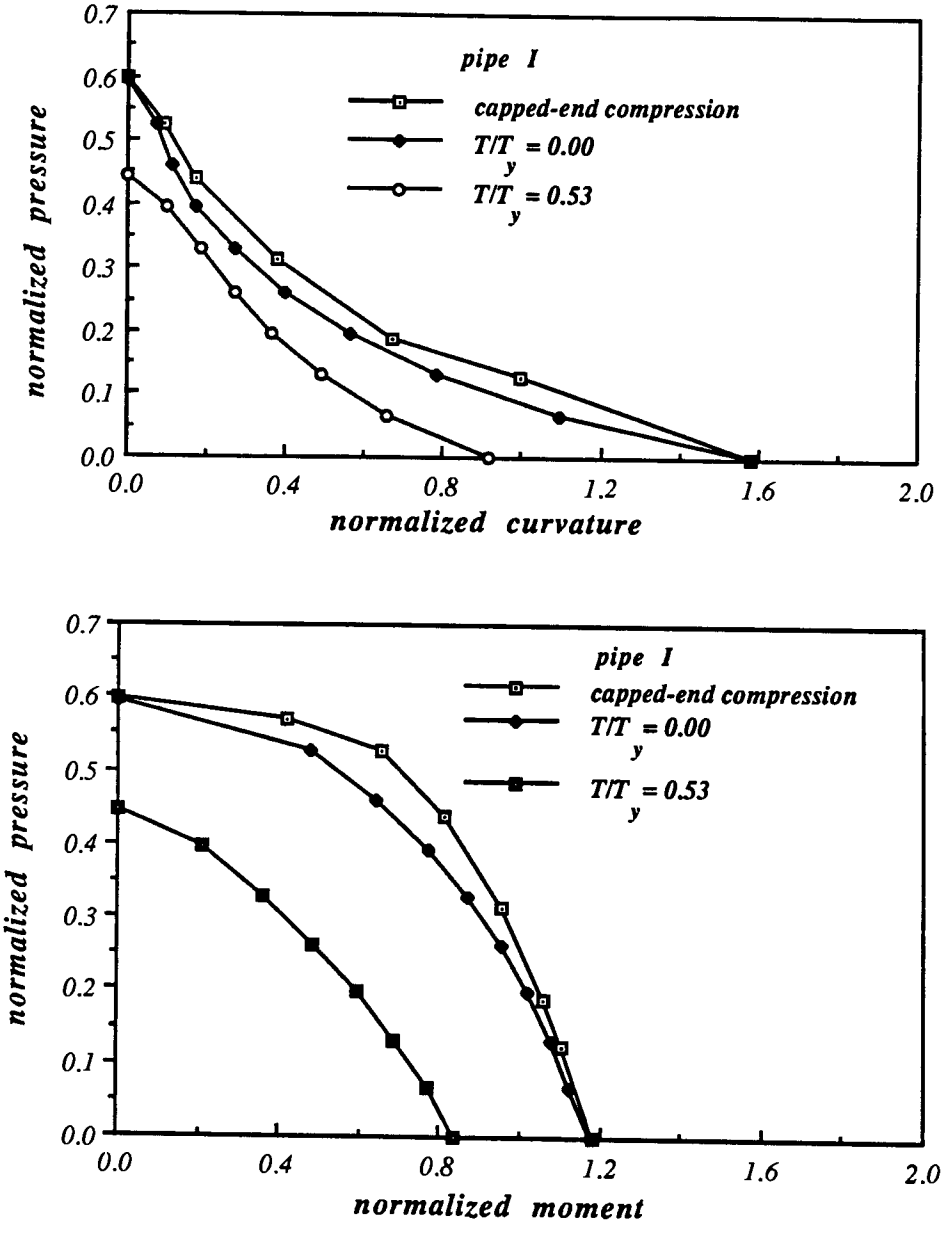

Figure 6.7: Pressure-bending envelopes for different values of axial force (pipe I).

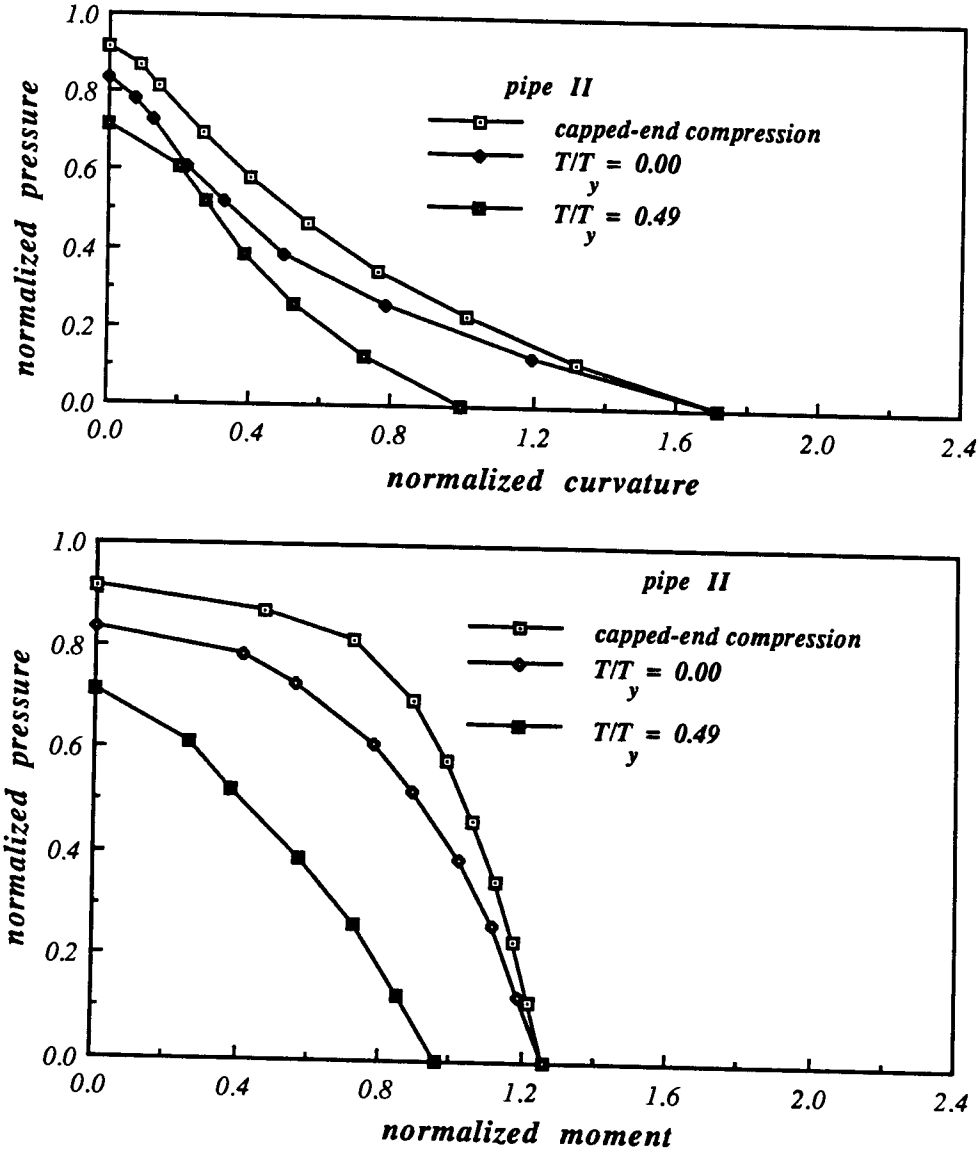

Figure 6.8: Pressure-bending envelopes for different values of axial force (pipe II).

the envelopes for zero tension. This is because, in the calculations of Chapter 5, there was no loading on the inner tube generator, and, therefore, in order to satisfy equilibrium, a compressive axial force, called "capped-end" force, was necessary. It is seen that this force has a beneficial effect on the response. More specifically, the yield pressure is somewhat increased and, therefore, this effect is expected to be more significant for pipe II which is thicker and its collapse pressure is close to the yield pressure. Note that, in order to be consistent with the results of the previous section, the intersection points of the envelopes with the pressure axis are obtained from Figure 6.1, and, therefore, they assume a small initial pipe imperfection. However, all other points of the envelopes where obtained assuming no initial imperfection. The tension-bending diagrams of the same pipes are shown in Figures 6.9 and 6.10, for three different values of pressure. For low values of pressure, the collapse envelopes continue above the yield tension (level a) due to the significant strain hardening of the material. In the same graphs, level b denotes the tension-pressure interaction collapse point for the third value of pressure (Figure 6.1). Note that in the present analysis there is a certain bending capacity at this level. This is because the pipe is assumed to be initially perfect, whereas level b was obtained from the analysis of the previous section, assuming a small initial imperfection.

The pressure-bending interaction diagrams of pipe III for different values of axial loading are presented in Figure 6.11 implying that the capacity is reduced in the presence of tension. The tension-moment interaction curves for the same pipe are given in Figure 6.12, indicating the same trends of behavior as for the other two pipes. However, if the tension-curvature interaction

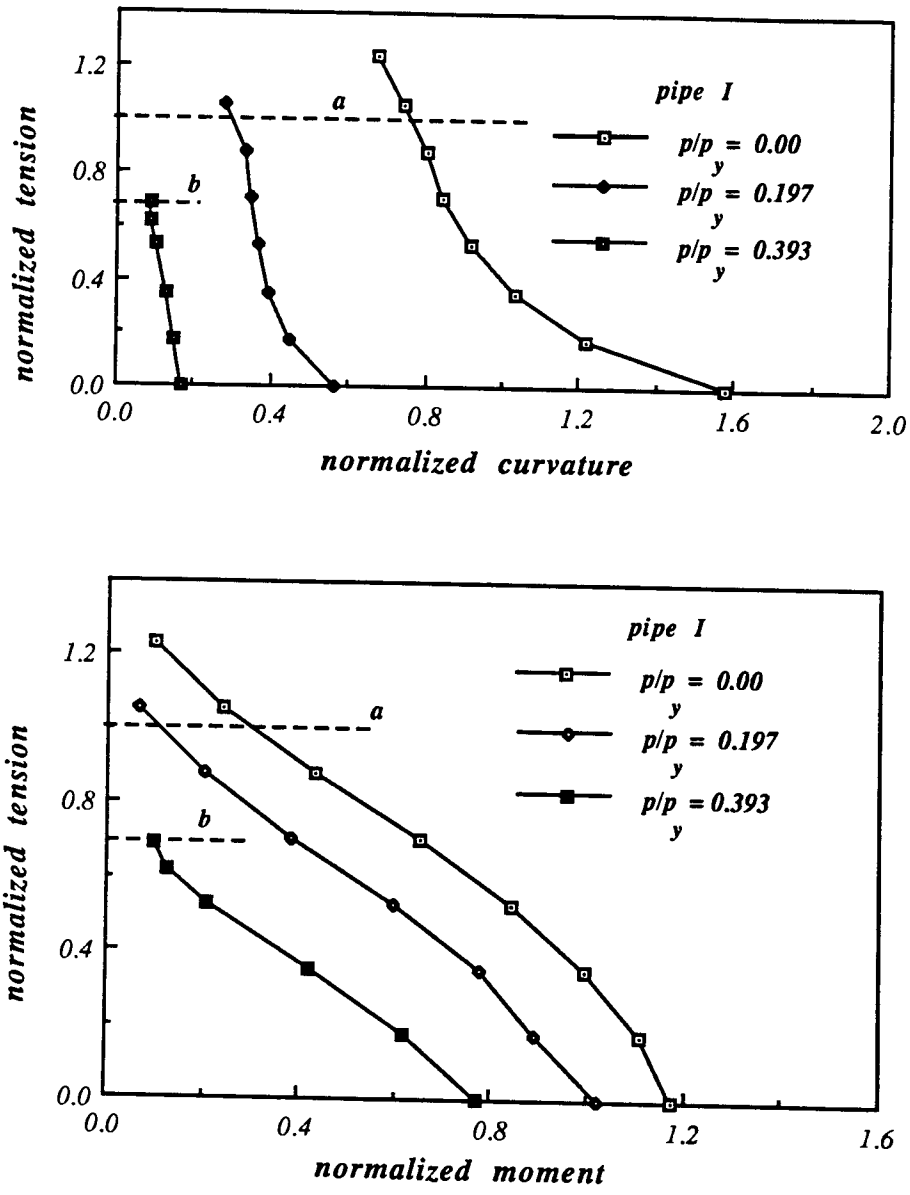

Figure 6.9: Tension-bending envelopes for different levels of pressure (pipe I).

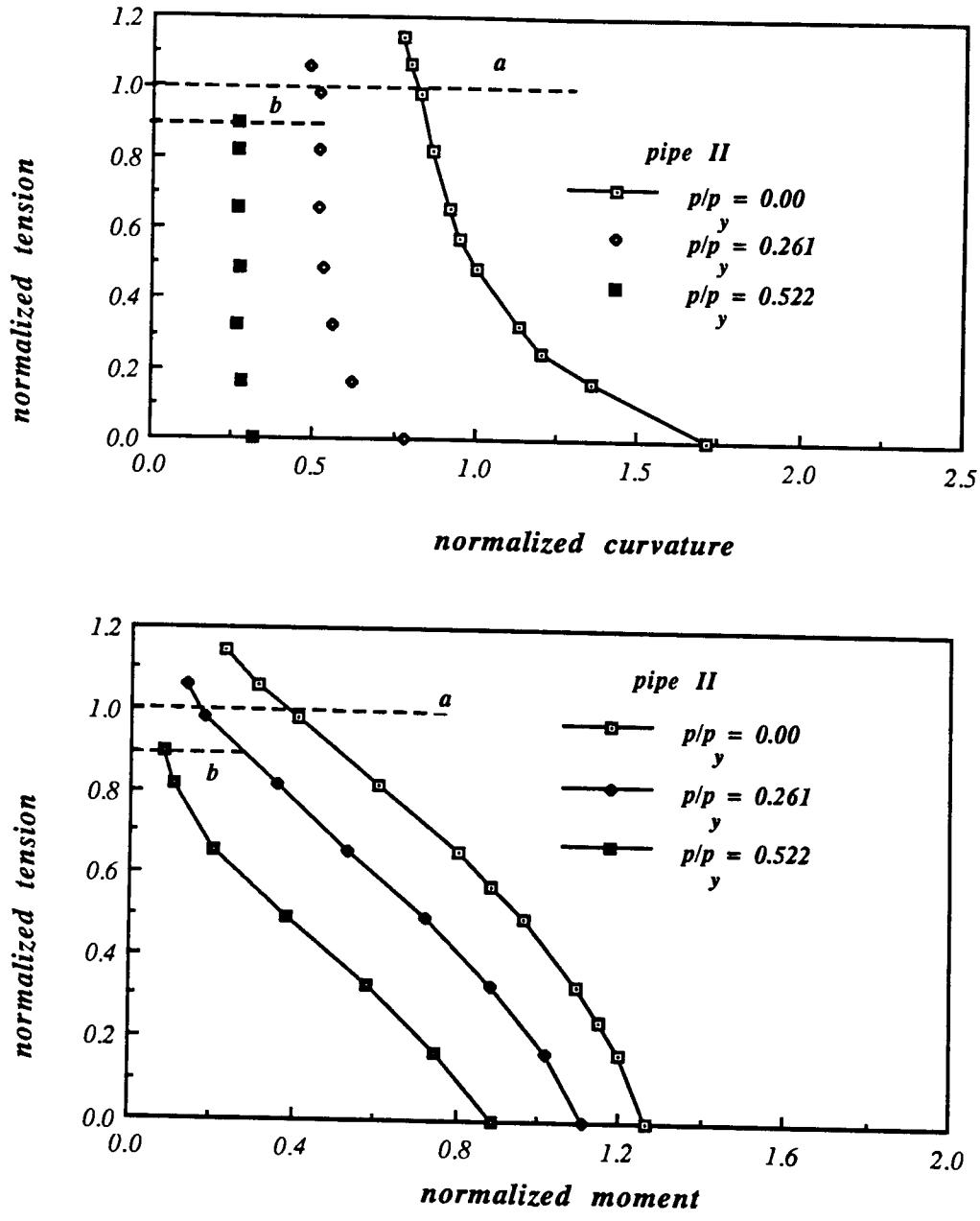

Figure 6.10: Tension-bending envelopes for different levels of pressure (pipe II).

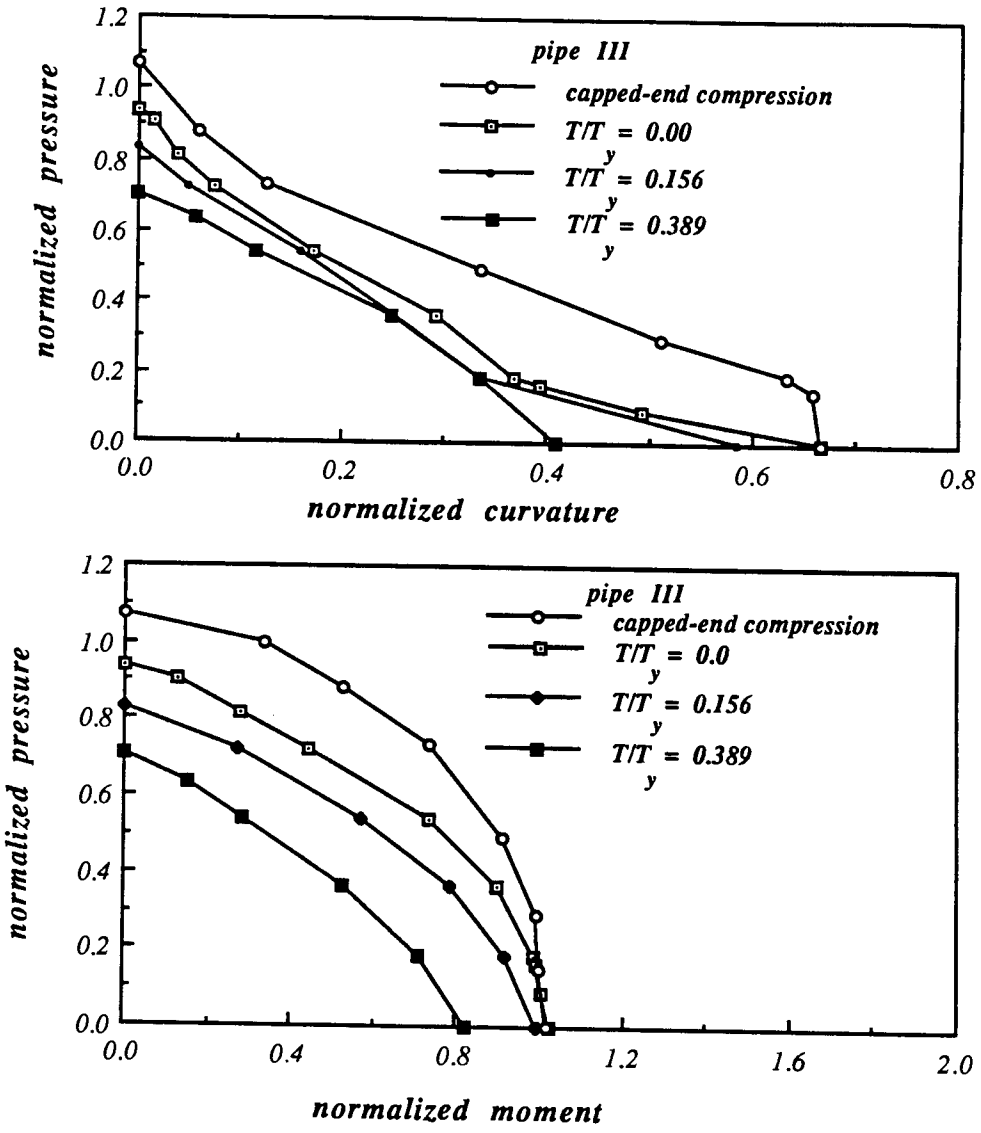

Figure 6.11: Pressure-bending envelopes for different values of axial force (pipe III).

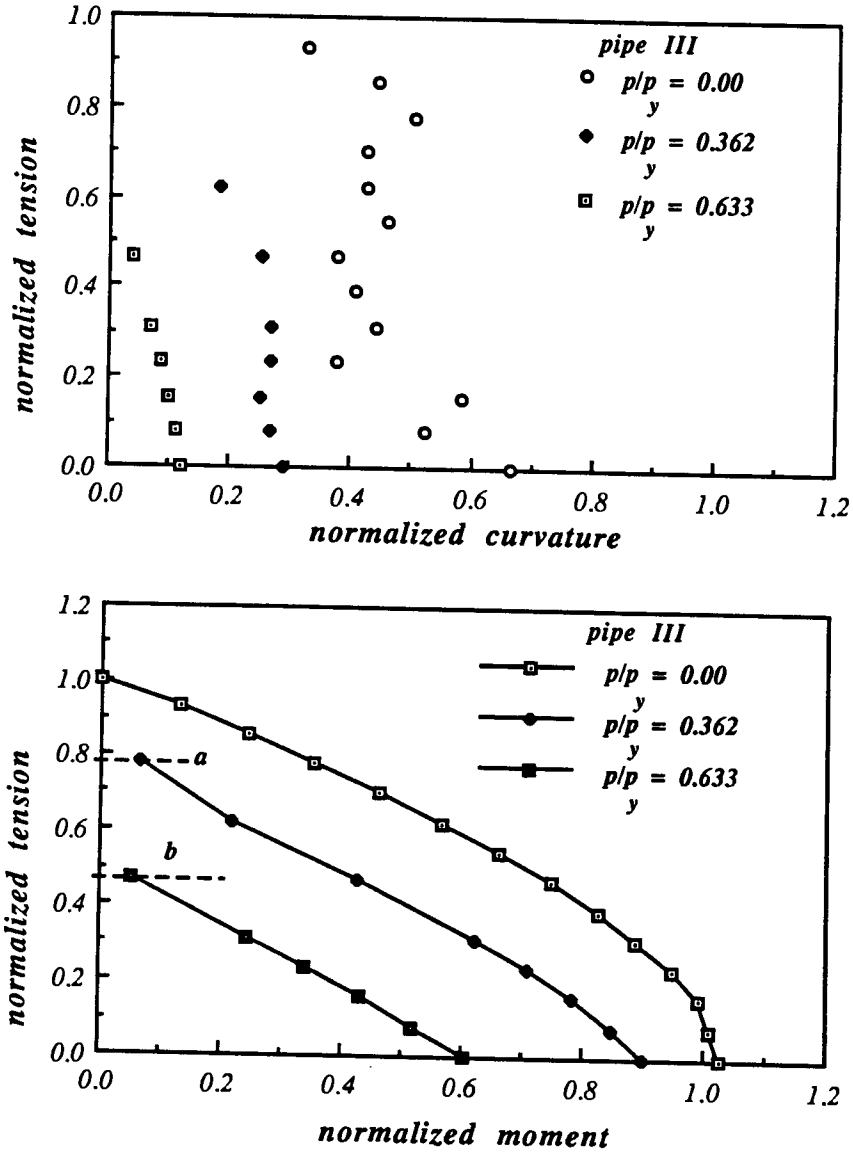

Figure 6.12: Tension-bending envelopes for different levels of pressure (pipe III).

is considered, results seem to be significantly different. Figure 6.12 also shows several tension-curvature interaction points for three different values of pressure. These points suggest an "irregular" behavior: in some cases, for increasing values of tension, although the limit moment decreases, the corresponding curvature increases. The phenomenon is accentuated at zero pressure, but it appears to subside at increasing levels of pressure. Considerable effort was made towards interpretation of these results. Unfortunately, an unambiguous explanation of the phenomenon is still elusive. However, some discussion on this matter is necessary.

To ensure consistency in the calculations, the analysis was repeated using smaller steps and a two-layer element. The results did not change. Furthermore, due to the presence of axial loading, the value of the moment depends on the point with respect to which the moment is defined. Throughout this study, the moment was referred to the middle of the segment joining the outermost and innermost points of the cross section. It should be noted that this point varies in the course of the analysis due to ovalization. The innermost point of the cross section was considered as an alternative reference point. However, the irregularity of the results did not change.

An important observation is that the material of pipe III has a uniaxial stress-strain curve with very slight hardening, as opposed to the materials of pipes I and II. Therefore, it is interesting to investigate the effect of strain-hardening on the phenomenon. Three bilinear materials are considered having the same Young's modulus E and yield stress σ_y as the X-52 material, but with a contant post-yield modulus equal to $E/464$, $E/208$ and $E/100$ respectively. Using these materials for pipe III, the tension-bending interaction is

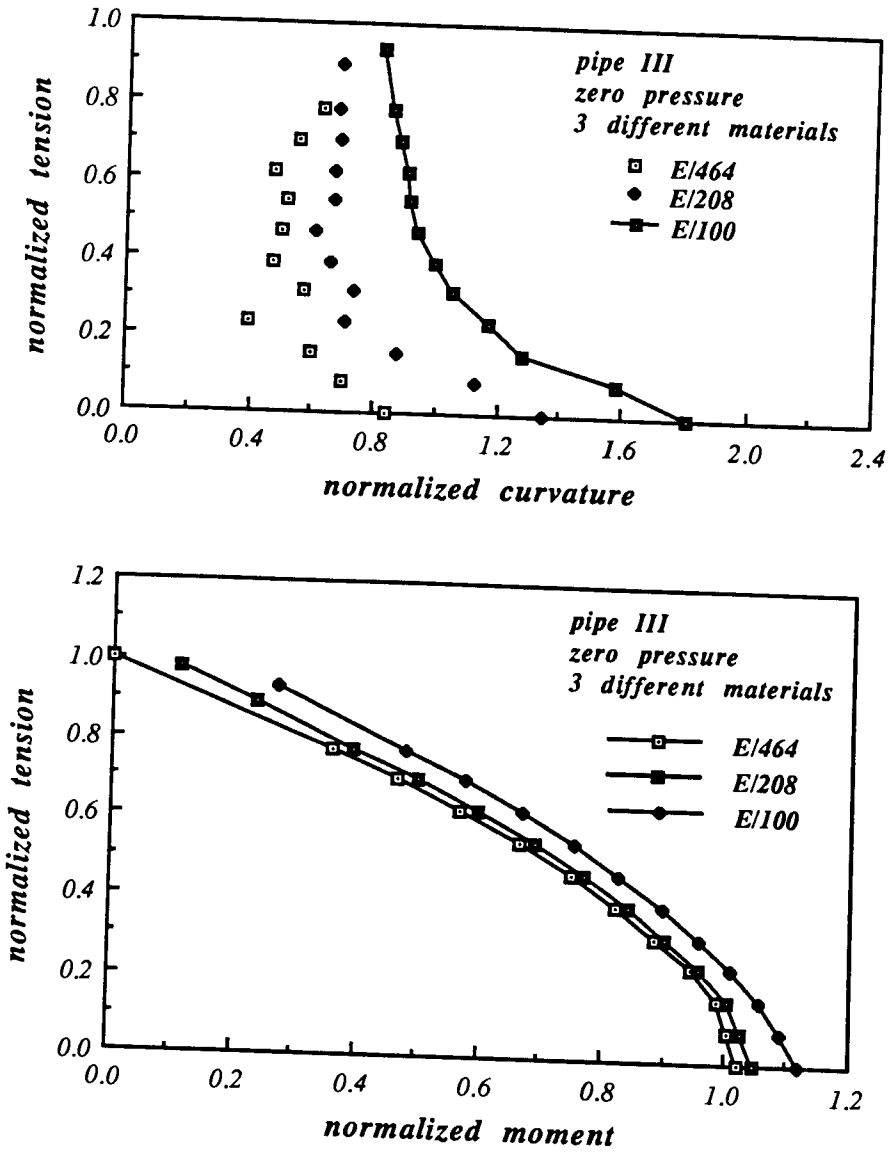

Figure 6.13: Pressure-bending envelopes for three different materials (pipe III).

examined. Figure 6.13 shows the tension-curvature, as well as the corresponding tension-moment curves. Clearly, the irregularity is gradually removed for increasing post-yield modulus.

The bending curves for pipe III (material X-52) are shown in Figure 6.14(a) for six different levels of pressure. All curves have very large "plastic plateaux", where the moment is almost constant. It is believed that this nearly perfectly-plastic behavior is responsible for the irregularity.

Figure 6.14(b) shows the bending curves for pressurized pipe III. It can be seen that the post-yield behavior becomes less flat when pressure is increased. This explains the "decrease" of the irregularity with increasing pressure.

Due to the large "plastic plateau" of the bending curves, the curvature that corresponds to the limit moment point does not seem to be a robust measure of the bending strength of the pipe. Indeed, soon after yielding, the pipe loses its bending stiffness. Therefore, the curvature where the limit moment occurs is not necessarily important.

This behavior appears to justify the "conservativeness" noted in Chapter 2 concerning pipeline design against bending loading. More specifically, the yield bending strain is used for the purpose of defining collapse. As a result, the corresponding curvature is much less than the curvature at which limit moment occurs. However, because of the very low bending stiffness soon after yielding, the yield curvature is a very reasonable measure of bending strength, whenever pipes with nearly perfectly-plastic material are considered.

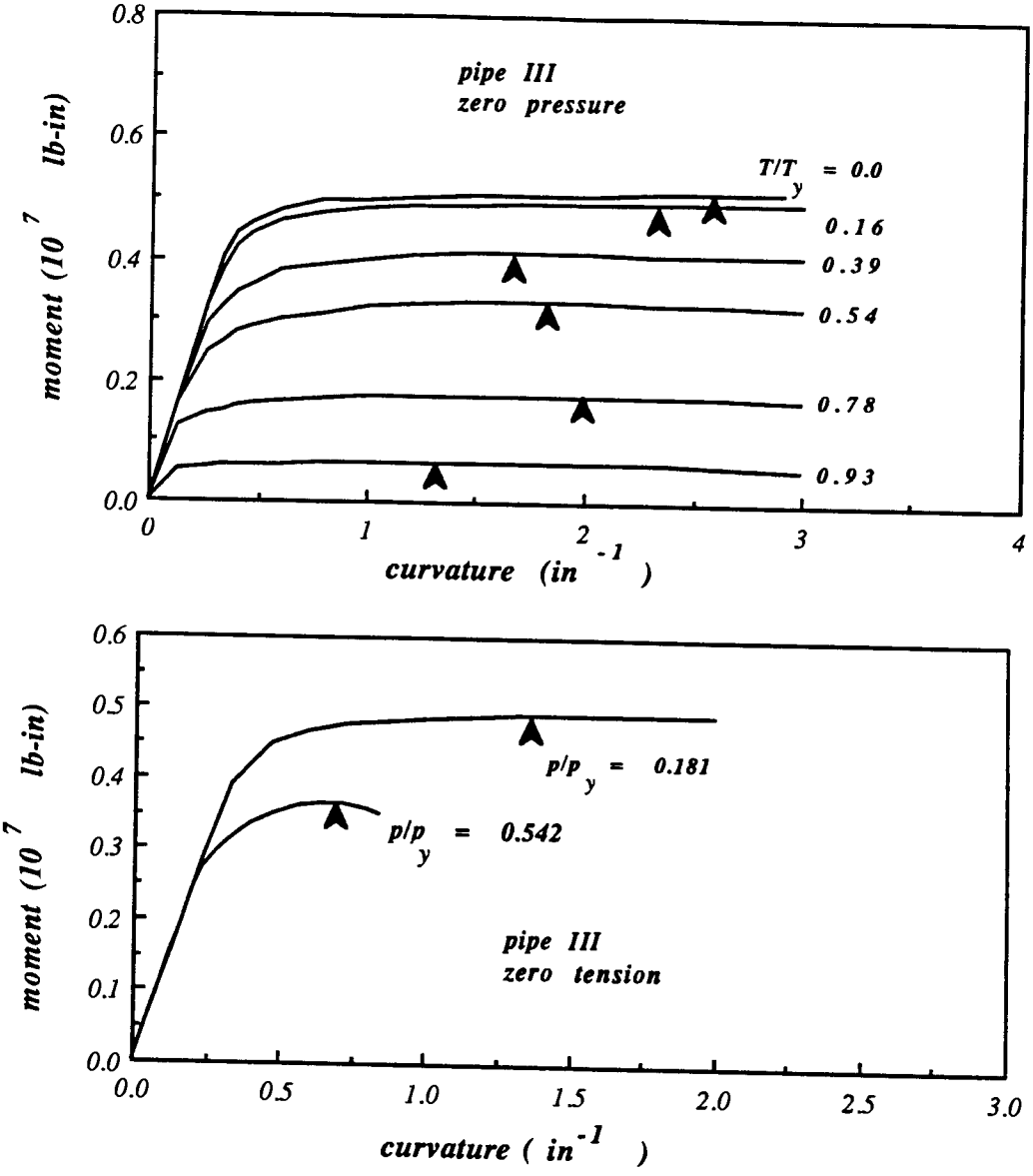

Figure 6.14: Moment-curvature curves for different values of tension and pressure (pipe III).

Chapter 7

Summary and Conclusions

This work was motivated by the design of deep-water pipelines. During the installation procedure, pipes are subjected to combination of high external pressure, bending and tension that may lead to buckling.

In order to investigate the problem, an analytical technique was developed, accounting for geometric and material nonlinearities. Nine-node isoparametric shell finite elements, capable of simulating pipes of arbitrary thickness, were employed. The introduction of the pressure node facilitates the tracing of equilibrium paths with limit pressure points.

First, the pressure-bending interaction was examined. Results were reported in the form of pressure-bending diagrams which were in good agreement with experimental data. It was observed that the response was sensitive to the loading history. To detect instability along any loading path, a simple stability criterion was employed, with meaningful results. Three loading sequences were considered ($k \rightarrow p$, $p \rightarrow k$ and radial paths) and the corresponding instability envelopes were obtained. Among these paths, the $p \rightarrow k$ path is the most critical.

Results from three-dimensional analysis which simulates a typical experimental procedure, showed that curvature calculated from end rotations may not be a good measure of bending in the pipe, whenever rigid plates are

welded at the end sections of the specimen. It is suggested that the average curvature over a five-diameter pipe segment about the middle section can be used to report experimental results.

A simplified two-dimensional analysis that uses the same basic technique and reduces significantly the computational cost was also implemented. Results were quite close to the experimental data.

Using the two-dimensional analysis, the effects of tension on pipe response were examined. Results for pressure-tension interaction were in good agreement with experiments and indicated that the response is slightly affected by the loading path.

Finally, the case where all loading parameters (pressure, bending and tension) are nonzero was considered. Results were reported in the form of pressure-bending diagrams for different levels of tension and tension-bending diagrams for different values of pressure. It was found that there is a certain irregularity concerning the tension-curvature interaction for low levels of pressure, when the material is nearly perfecty-plastic. This implies that, curvature may not be a robust measure of bending capacity, especially when the material has a low post-yield modulus.

The results of this work are expected to provide engineers with a better understanding of the phenomenon of buckling under combined loading towards safe pipeline design.

BIBLIOGRAPHY

[1] Aanhold, J. E. van, "Finite Element Algorithm for Static Analysis of Deep-water Pipelaying", 1st *OMAE, Deepsea Systems Symposium*, ed. ASME, Vol. II, pp. 107–112, New Orleans, 1982.

[2] Ades, C. S. "Bending strength of tubing in the plastic range." *J. Aeronautical Sciences*, V.24, pp. 605–610, 1957.

[3] Ahmad, S., Irons, B. M. and Zienkiewicz, O. C., "Analysis of Thick and Thin Shell Structures by Curved Finite Elements," *International Journal for Numerical Methods in Engineering*, Vol. 2, pp. 419–451, 1970.

[4] American Petroleum Institute "Bulletin on Formulas and Calculations for Casing, Tubing, Drill Pipe, and Line Pipe Properties", API Bul. 5C3, July 1989.

[5] Bathe, K. J., *Finite Element Procedures in Engineering Analysis*, Prentice-Hall Inc., New Jersey, 1982.

[6] Brazier, L. G. "On the flexure of thin cylindrical shells and other thin sections." *Proceedings, Royal Society*, A, V. 166, pp. 104–114, 1927.

[7] Corona, E. and Kyriakides, S. "On the collapse of inelastic tubes under combined bending and pressure." *Int. J. Solids & Structures* V. 24, pp. 505–535, 1988.

[8] Corona, E. and Kyriakides, S. "Collapse of pipelines under combined bending and external pressure." *Proceedings, International Conference on the*

Behaviour of Offshore Structures, V. 3, pp. 953–964, Trondheim, Norway, 1988.

[9] Fabian, O. "Collapse of cylindrical, elastic tubes under combined bending, pressure and axial loads." *Int. J. Solids & Structures* V. 13, pp. 1257–1270, 1977.

[10] Fabian, O. "Elastic-plastic collapse of long tubes under combined bending and pressure loads." *Ocean Enginnering*, V. 8, pp. 295–330, 1981.

[11] Fowler, J. R., "Large scale tests." *Proceedings, Seminar on Collapse of Offshore Pipelines*, Houston, Texas, February 1990.

[12] Gellin, S. "The plastic buckling of long cylindrical shells under pure bending." *Int. J. Solids & Structures* V. 10, pp. 397–407, 1980.

[13] Gurtin, M. E., *An Introduction to Continuum Mechanics*, ed. Academic Press, London 1981.

[14] Hibbit, H. D, Marcal, P. V. and Rice, J. R., "A Finite Element Formulation for Problems of Large Strain and Large Displacement," *Int. J. Solids & Structures*, Vol. 6, pp. 1069–1586, 1970.

[15] Hutchinson, J. W., "Finite Strain Analysis of Elastic-Plastic Solids and Structures," *Numerical Solutions of Nonlinear Structural Problems*, edited by R. F. Hartung, ASME, The Applied Mechanics Division, Vol. 6, pp. 17–29, 1973.

[16] Jensen, J. J. "Collapse of long, elastic-plastic pipes subjected to combined loads." *Proceedings, European Seminar on Offshore Oil and Gas*, Birmingham, 1984.

[17] Johns, T. G. and McConnell, D. P. "Response and stability of elastoplastic circular pipes under combined bending and external pressure." *Proceedings, 11th Pipeline Technology Conference*, Houston, Texas, 1983.

[18] Katsounas, A. T. and Tassoulas, J. L. "Finite element analysis of propagating buckles in deep-water pipelines." *Offshore Technology Research Center, Report No 1*, The University of Texas, Austin, Texas, 1989.

[19] Kyriakides, S. and Babcock, C. D., "Large Deflection Collapse of an Inelastic InextensionalRing under External Pressure," *International Journal of Solids and Structures*, Vol. 17, No. 10, pp. 957–973, 1981.

[20] Kyriakides, S. and Shaw, P. K., "Reponse and Stability of Elastoplastic Circular Pipes Under Combined Bending and External pressure," *International Journal of Solids and Structures*, Vol. 18, No. 11, pp. 957–973, 1982.

[21] Kyriakides, S., Corona, E., Madhavan, R. and Babcock, C. D. "Pipe Collapse Under Combined Pressure, Bending and Tension Loads", *Offshore Technology Conference*, OTC 6104, pp. 541–550, Houston, Texas, 1989.

[22] Kyriakides, S. and Babcock, C. D., "Experimental Determination of the Propagation Pressure of Circular Pipes," *Journal of Pressure Vessel Technology*, Vol. 103, pp. 328–336, 1981.

[23] Langner, C. G. and Ayers, R. R., "The Feasibility of Laying Pipelines in Deep Waters." *ASME, Proceedings, OMAE Symposium*, Vol. 1, pp. 478–489, 1985.

[24] Langner, C. G. "Relationships for Deepwater Suspended Pipe Spans" *ASME, 3th OMAE Symposium*, pp. 552–558, 1984.

[25] Langner, C. G. "Design of Deepwater Pipelines" *TNO-IWECO* 30^{th} *Ann. Symp. on Underwater Technology*, Kurhaus, Netherlands, May 1984.

[26] Langner, C. G. private communication, May 1990.

[27] Malvern, L. E., *Introduction to the Mechanics of a Continuous Medium*, Prentice-Hall, Englewood Cliffs, New Jersey, 1969.

[28] Mesloh, R. E., Johns, T. G. and Sorenson, J. E., "The Propagating Buckle," *Proceedings, BOSS 76*, Vol. 1, pp. 787–797, 1976.

[29] Murphey, C. E. and Langner, C. G. "Ultimate strength under bending collapse and fatigue." 4^{th} *International Offshore and Arctic Engineering Symposium*, V. 1, pp. 467–477, 1985.

[30] Needleman, A., "Finite Elements for Finite Strain Plasticity Problems," *Plasticity of Metals at Finite Strain: Theory, Experiment and Computation*, edited by E. H. Lee and R. L. Mallett, Rensselaer Polytechnic Institute, Troy, New York, pp. 387–436, 1982.

[31] Palmer, A. C., Hutchinson, G. and Ells, J. W., "Configuration of Submarine Pipelines During Laying Operations" *Transactions of ASME*, V. 96, pp. 1112–1118, November 1974.

[32] Palmer, A. C. and Martin, J. H., "Buckle Propagation in Submarine Pipelines," *Nature*, Vol. 1, pp. 46–48, 1975.

[33] Reddy, B. D. "An Experimental Study of the Plastic Buckling of Circular Cylinders in Pure Bending", *Int. J. Solids and Structures*, V. 15, pp. 669–683, 1979.

[34] Reissner, E. "On finite bending of pressurized tubes." *ASME J.Applied Mech.* V. 26, pp. 386–392, 1959.

[35] Reissner, E. "On finite pure bending of cylindrical tubes." *Osterr.Ing.Arch.*, V. 15, pp. 165–172, 1961.

[36] Reissner, E. and Weinitschke, H. J. "Finite pure bending of circular cylindrical tubes." *Quarterly of Applied Mathematics* , V. 10, pp. 305–319, 1963.

[37] Row, D., Chan, E. and Langner, C. G. "Prediction of pipe collapse under external pressure, axial load and bending.", *Offshore and Arctic pipelines (ASME)* edited by J.S.Chung and K.Karal, 1987.

[38] Sherman, D. R. "Test of circular steel tubes in bending." *ASCE J.Struct.Div.*, V. 102, ST11, pp. 2181–2195, 1976.

[39] Song, H.- W. and Tassoulas, J. L. "Dynamics of propagating buckles in deep-water pipelines." *Offshore Technology Research Center, Report No 6*, The University of Texas, Austin, Texas, 1990.

[40] Steel, W. J. M and Spence, J., "On Propagating Buckles and their arrest in sub-sea pipelines," *Proceedings of the Institution of Mechanical Engineers*, Vol. 197, pp. 139–147, 1983.

[41] Stephens, W. B., Starnes, J. H., Jr. and Almroth, B. O. "Collapse of long cylindrical shells under combined bending and pressure loads." *AIAA Journal*, V. 13(1), pp. 20-25, 1975.

[42] Switaiski, B., "Stresses and Deformations in Deepsea Pipelines during laying by J-method",1^{st} *OMAE, Deepsea Systems Symposium*, ed. ASME, Vol. II, pp. 96–106, New Orleans, 1982.

[43] Tassoulas, J. L., Katsounas, A. T. and Song, H-W. "Finite element analysis of propagating buckles in deepwater pipelines." *Proceedings,* 22^{nd} *Offshore Technology Conference*, Houston, Texas, pp. 631–638, 1990.

[44] Timoshenko, S., "Working Stresses for Columns and Thin-Walled Structures." *Trans. ASME, Applied Mechanics Division*, V. 1, pp. 173–183, 1933.

[45] Wilkins, J. R., "Offshore Pipeline Stress Analysis" *Offshore Technology Conference*, OCT 1227, Houston, Texas, 1970.

[46] Winter, P. E. de, Stark, J. W. B., Witteveen, J., "Collapse Behaviour of Submarine Pipelines", *Shell Structures: Stability and Strength*, ed. R. Narayanan, Elsvier Appl. Sc. Publ., Chapter 7, pp. 221–226, 1985.

[47] Zienkiewicz, O. C.. *The Finite Element Method*, Third Edition, McGraw-Hill, London, England, 1977.